Steady-State Density Functional Theory for Non-equilibrium Quantum Systems

Liu Shuanglong

(B.Sc., SiChuan University)

a thesis submitted

for the degree of Doctor of Philosophy

Department of Physics

National University of Singapore

2015

Declaration

I hereby declare that this thesis is my original work and it has been written by me in its entirety. I have duly acknowledged all the sources of information which have been used in the thesis.

This thesis has also not been submitted for any degree in any university previously.

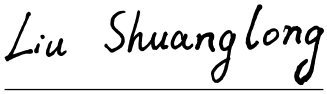

Liu Shuanglong
3 November 2015

Acknowledgments

First I would like to thank NUS for supporting my life, study, and research. Second, I came to Singapore in seek of theoretical physics four years ago but took up computational physics five months later. Regarding this turning point, I owe my sincere thanks to Dr. Tan Meng Chwan, Dr. Gong Jiangbin, and Dr. Wang Zhisong who guided and encouraged me. Third, thank Dr. Yeo Ye, Dr. Wang Jian-Sheng, et al. for your teaching excellence from which the benefit on us continues. Fourth, Jiajun, Luo Yuan, Gong Li, Jingnan, Weiqiang, Jiang Yong, Leiqiang, Longwen, Di Kai, Yao Yong, Jialin, Zhao Qin, Chenguang, Quy Duong, Lili, Sun Yang, Zhaohong, Lili and many other friends, thanks not only for sharing with me joyous time and evoking discussions but also for bringing thoughtful lessons and invaluable growth to me. Fifth, thank Guo Na, Yongjie, Yang Ming, Wenxuan and other group members for your helps in my research. At the beginning, it was Argo who taught me a lot, many thanks to Argo. Here I give special thanks to my supervisor, Dr. Zhang Chun, who has paid numerous efforts in educating, training, and helping me. To some degree, he has made a part of what I am today. Last but not least, thanks for living in my dreams, my families.

To my brother

Contents

Abstract

Recently, electron transport properties of molecular junctions under finite bias voltages have attracted a lot of attention because of the potential application of molecular electronic devices. When a molecular junction is under zero bias voltage at zero temperature, it is in equilibrium ground state and all its properties can be solved by ground-state density functional theory (GS-DFT) where ground-state electron density determines everything. Under finite bias voltage, the molecular junction is in non-equilibrium steady state. According to Hershfield's non-equilibrium statistics, a system in non-equilibrium steady state corresponds to an effective equilibrium system. This correspondence provides the basis for the steady-state density functional theory (SS-DFT) which will be developed in this thesis. In SS-DFT, we proved that the total electron density is not enough to determine the properties of the system in steady state. However, two electron densities, equilibrium electron density ρ_e and current-carrying electron density ρ_n, now play the role of basic variables. Specifically, the ground state energy of the effective equilibrium system is a functional of ρ_e and ρ_n, i.e. $\tilde{E}_0 = \tilde{E}_0[\rho_e, \rho_n]$. Furthermore, $\tilde{E}_0[\rho_e, \rho_n]$ is stationary upon variation of ρ_e and ρ_n, which leads to a dual mean field (DMF) approach for obtaining the desired steady state. In the DMF approach, current-carrying electrons experience a different mean field potential from that for the equilibrium electrons; and two sets of coupled Schrödinger-like mean field equations need to be solved simultaneously. Before one sets out to solve the mean field equations, it remains to find the explicit form of the exchange correlation part of $\tilde{E}_0[\rho_e, \rho_n]$, i.e. $E_{xc}[\rho_e, \rho_n] = E_x[\rho_e, \rho_n] + E_c[\rho_e, \rho_n]$. For this purpose, we generalized the Thomas-Fermi-Dirac model (gTFD) into non-equilibrium situation and derived the

exchange energy density $\mathcal{E}_x^n$ of a non-equilibrium uniform free electron gas as a function of ρ_e and ρ_n. $\mathcal{E}_x^n(\rho_e, \rho_n)$ is then used to approximate the general exchange energy functional $E_x[\rho_e, \rho_n]$. The non-equilibrium correction to the correlation energy is out of the scope of this thesis. For weakly correlated systems, we simply set E_c to GS-DFT one. In addition, we have implemented SS-DFT in SIESTA package and simulated several realistic molecular junctions, including a zigzag graphene nano-ribbon (ZGNR) junction, a junction consisting of a benzene molecule and carbon nano-tube (CNT) leads, and a junction with self-assembled mono-layer (SAM) of alkanethiolates sandwiched between silver leads. Our calculations for the ZGNR junction showed that SS-DFT recovers the results obtained from the conventional DFT+NEGF method (via TranSiesta function) in the limit of zero bias; while at large biases, SS-DFT produced significantly lower electric current since the exchange potential for current-carrying electrons in SS-DFT is higher than the GS-DFT one. For the CNT-benzene-CNT junction, SS-DFT bore lower energy than DFT+NEGF at all biases. In a limit case where the CNT leads were pulled away from the benzene molecule so that they are decoupled, SS-DFT was able to produce the local equilibrium electronic structure of the benzene molecule while DFT+NEGF failed to do so. Finally, the simulations of the SAM junctions explained the experimentally observed odd-even effect in the charge mobility. In summary, we have developed a steady state density functional theory which paves the way to first-principles studies of the electronic and transport properties of molecular junctions under finite bias.

List of Tables

List of Figures

If I have seen further, it is by standing on the shoulders of giants.

Isaac Newton

0 Introduction

Many-body problems can be tackled by density functional theory (DFT) and many-particle formalism (MPF). MPF is based on second quantization, Green's functions, and diagrammatic calculations.[1–3] It provides systematic formulas for calculating electron density and transport properties. DFT is a mean-field theory to solve many-body problems efficiently.[4,5] It bears the electronic structure of a many-body system. They can be combined to study the transport properties of open quantum systems in non-equilibrium steady state.[6]

Ground state density functional theory (GS-DFT) uses ground state electron density to determine the ground state properties.[7] Currently, GS-DFT is widely used

for the study of non-equilibrium steady state for which GS-DFT is actually not valid. In this thesis, we develop a steady-state density functional theory (SS-DFT) where two electron densities, equilibrium and current-carrying electron densities, are the basic variables. SS-DFT is solid specially for steady state. It will be combined with MPF for studying electron transport through molecular junctions which is the key problem in molecular electronics.[8]

0.1 Molecular Electronics

Proposed by Aviram and Ratner in 1974, molecular electronics utilizes molecules as functional units in a circuit.[9] It is the eventual successor to micro electronics as the minimization process of MOSFET continues. At the molecular scale, electrons behave as wave, instead of particles, which puts a limit on the size of MOSFET. It was estimated that the dimension of the smallest MOSFET is of 1.5 nm,[10] while sub-5 nm MOSFET has been made in lab.[11] Thus, the need for greater computation power and lesser energy consumption in contemporary information era urges the study of molecular electronic devices. Experimentally, various molecular devices such as diodes, switches, and transistors have been demonstrated experimentally[12,13] since the invention of the scanning tunneling microscope (STM) in 1981.[14]

STM enabled us to manipulate materials at the atomic level. A normal STM scan of some nano particle on a substrate can be viewed as the formation of a molecular junction.[15–17] To fabricate a molecular junction with desired molecules in between, the STM break junction technique can be employed.[18,19] However, molecular junctions made by STM usually involve a tip and a surface (substrate). Other configurations of molecular junctions can be achieved by the techniques of mechanically controllable break junction (MCB)[20] or electromigration break junction (EMB).[21–23]

Since the 1990s, transport properties of molecular junctions have been probed. In 1993, the conductance of an iron atom bridging an STM tip and a metal surface was

measured by Crommie.[15] Subsequently, in 1997, Reed formed benzene-1, 4-dithiol junctions with gold nanowire leads and measured its conductance.[24] In this experiment, the Au-S bond links benzene to the gold lead stabilizing the molecular junction. In addition to the Au-S bond, M-N[25] and M-C[26] bonds can also work in a similar way for other molecular junctions. Here M represents metal. Generally, a conductance measurement is hard to repeat due to variations in the atomic configuration of the junction.[27–30] Despite the structural uncertainty, Tao et al. successfully confirmed the conductance of a single molecule junction by repeatedly forming the junction and analyzing the conductance statistically in 2003.[18] This study made a great contribution to the measurement of electron transport through molecular junctions.

In summary, advanced techniques such as STM, MCB and EMB were developed to fabricate molecular junctions. However, it is still formidable to control the molecular scale structures precisely. Despite the structural uncertainty, the conductance of a single molecule junction can be identified by statistical analysis.

0.2 Many-Body Theories

Theoretically, the goal is to predict the transport properties of an open quantum system in non-equilibrium steady state. Two components are needed for achieving this goal. One is the quantum transport formula and the other is the electronic structure of the open system.

The transport formula can be obtained from MPF. Based on the concept of wave scattering, Landauer derived a formula for non-interacting two-terminal junctions in the 1950s.[31] Later in 1986, the Landauer formula was generalized to non-interacting multiple-terminal cases by Büttiker.[32] The Landauer-Büttiker formalism greatly improved our understanding of quantum electron transport. In 1971, the first rigorous quantum transport theory was derived by Caroli et al. based on non-equilibrium Green functions (NEGF)[33] for non-interacting systems.[34,35] In these studies, the steady

state evolves from a non-equilibrium initial condition with the coupling between a lead and the center region turned on gradually. Alternatively by establishing the steady state from an equilibrium initial condition, Cini constructed another equivalent quantum transport scheme also with NEGF in 1980.[36] Importantly, Meir and Wingreen generalized Caroli's work to interacting cases in 1992.[8] The Meir-Wingreen formula provides a general theoretical framework for studying quantum electron transport. It reduces to the Landauer formula in the non-interacting limit.

The electronic structure of the open quantum system is needed when we apply a transport formula. To obtain the electronic structure, one is concerned with three issues: open boundary condition, non-equilibrium effects and electron correlation. In 1995, Lang used a self-consistent procedure based on GS-DFT to attack the problem.[37,38] In Lang's method, GS-DFT includes electron correlation. The electron density was calculated by summing up the squares of the occupied scattering states which were found by solving a Lippmann-Schwinger equation with the open boundary encoded. However, as a limitation, the leads were described by the jellium model which ignores the atomistic structure. In 2001, based on Lang's method, Guo et al. invented the DFT+NEGF method which employs NEGF to compute the electron density.[39] NEGF takes care of the open boundary condition and the non-equilibrium distribution. Another improvement by Guo et al. is taking the atomistic structure of the leads into account. Several implementations of DFT+NEGF have been reported.[40–42] Importantly, the DFT+NEGF method enabled efficient simulations of realistic molecular junctions. It has been extended to tackle spin dependent transport[43] and include electron-phonon coupling.[44,45] It usually bears qualitatively correct current-voltage characteristics for molecular junctions.[46,47] However, the predicted currents can differ from the experimental results by several orders of magnitude.[48] Possible reasons include the complexity of the molecule-lead contact, the self-interaction error, inaccurate electron correlation, and lack of dynamic effects.[49–53] In this thesis we would

like to address the problem that non-equilibrium effect is absent in GS-DFT and apply SS-DFT instead to solve the electronic structure of the open quantum system.

In 1993, Hershfield showed that a system in non-equilibrium steady state corresponds to an effective equilibrium system.[54] The correspondence provides the basis for SS-DFT. In SS-DFT, the equilibrium and current-carrying electron densities, ρ_e and ρ_n, together determine the properties of the open system in the steady state, e.g. the energy $E_0 = E_0[\rho_e, \rho_n]$. In order to approximate the exchange energy functional $E_x[\rho_e, \rho_n]$, we generalized the Thomas-Fermi-Dirac (TFD) model to non-equilibrium cases and derived the exchange energy density $\mathcal{E}_x^n$ of a non-equilibrium uniform non-interacting electron gas as a function of ρ_e and ρ_n.[55] In this way, the non-equilibrium effects are taken into account at the energy functional level explicitly. Furthermore, the stationary condition of the effective ground state energy leads to a dual mean field (DMF) approach for obtaining the steady state.[56] In the DMF approach, equilibrium electrons experience a different mean field from that for current-carrying electrons. NEGF is also used to take care of the open boundary condition in the DMF approach. We have implemented SS-DFT in the SIESTA package and simulated several realistic molecular junctions with our implementation.[57] Note that the correlation energy functional for SS-DFT is still unknown. In our simulations, we simply set it to the GS-DFT one, which may not be a bad approximation for weakly correlated systems.

As an overview, Fig. 0.1 shows the theoretical framework for studying the transport properties of an open quantum system in steady state. In this framework, NEGF and SS-DFT are combined to solve the problem.

0.3 Purpose and Scope

The purpose of our study is to develop the steady-state density functional theory for open quantum systems in a non-equilibrium steady state and provide a first-

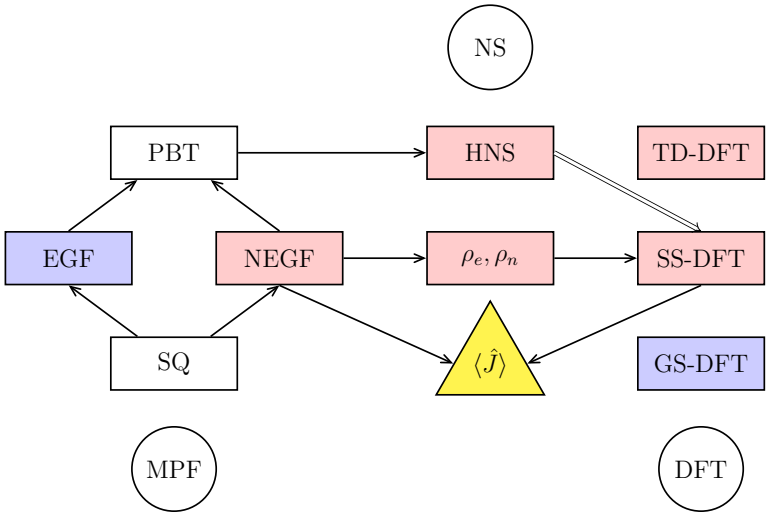

Figure 0.1: The theoretical framework for studying open quantum systems in steady state. The abbreviations: SQ stands for second quantization; EGF stands for equilibrium Green's function; PBT stands for perturbation theory; NS stands for non-equilibrium statistics; HNS stands for Hershfields' non-equilibrium statistics; $\langle \hat{J} \rangle$ is the steady electric current. The blue objects pertain to equilibrium ground state. The red objects pertain to non-equilibrium steady state.

principles method based on SS-DFT for simulating the electronic and transport properties of molecular junctions.

SS-DFT further improved our understanding of open quantum systems in steady state by identifying their basic variables. Our first-principles method based on SS-DFT will be an efficient theoretical tool for the study of electron transport in molecular devices.

A concise account of many-particle formalism and density functional theory will be given in chapter 1. In chapter 2, SS-DFT will be developed in detail. Finally, simulations of several molecular junctions will be presented in chapter 3. Chapters 2 and 3 contain the main results of this thesis. Experimental studies are absent because of the theoretical nature of this work.

The book of nature is written in the language of mathematics.

Galileo Galilei

1 Many-Body Theories

In this chapter, we review the many-particle formalism (MPF) and the ground-state density functional theory (GS-DFT). For MPF, both equilibrium and non-equilibrium Green's functions will be covered.

1.1 Second Quantization

In this section, we explore the language of second quantization whose power lies in operator algebra. Second quantization relies on creation and annihilation operators which will be introduced gradually in the following.

Let $\mathcal{H}$ be the Hilbert space spanned by the eigenstates of a single particle Hamilto-

nian $\hat{h}$

$$\hat{h}\,|\alpha\rangle = \epsilon_\alpha\,|\alpha\rangle\,, \tag{1.1}$$

where $|\alpha\rangle$ are orthonormal

$$\langle\alpha'|\;\alpha\rangle = \delta_{\alpha\alpha'}. \tag{1.2}$$

Any vector in $\mathcal{H}$ is a linear combination of $|\alpha\rangle$s. Since a many-body system is a collection of individual particles, its state can be constructed from single particle states. All states constructed in this way span a configuration space. For a system of N particles, the configuration space $\mathcal{C}_N$ is

$$\mathcal{C}_N \equiv \mathcal{H}\otimes\mathcal{H}\otimes\cdots\otimes\mathcal{H}. \tag{1.3}$$

Any vector in $\mathcal{C}_N$ is a linear combination of $|\alpha_1\rangle\otimes|\alpha_2\rangle\otimes\cdots\otimes|\alpha_N\rangle$s.

The Hilbert space $\mathcal{H}_N$ for a system of N particles, defined in the configuration space $\mathcal{C}_N$, consists of complex, square integrable functions. $|\alpha_1,\alpha_2,\cdots,\alpha_N) = |\alpha_1\rangle\otimes|\alpha_2\rangle\otimes\cdots\otimes|\alpha_N\rangle$ form the canonical basis for $\mathcal{H}_N$. Its completeness reads

$$\sum_{\alpha_1,\cdots,\alpha_N} |\alpha_1,\alpha_2,\cdots,\alpha_N)\,(\alpha_1,\alpha_2,\cdots,\alpha_N| = 1. \tag{1.4}$$

The canonical basis however doesn't reflect the anti-symmetry of a N-fermion state ψ_N, namely

$$\psi_N(\boldsymbol{x}_{p_1},\boldsymbol{x}_{p_1},\cdots,\boldsymbol{x}_{p_N}) = (-1)^p\psi_N(\boldsymbol{x}_1,\boldsymbol{x}_2,\cdots,\boldsymbol{x}_N) \tag{1.5}$$

with p representing some permutation. In order to find an anti-symmetric basis, define the symmetrization operator $\hat{\mathcal{P}}$, for any ψ_N

$$\hat{\mathcal{P}}\psi_N(\boldsymbol{x}_1,\boldsymbol{x}_2,\cdots,\boldsymbol{x}_N) \equiv \frac{1}{N!}\sum_p (-1)^p\psi_N(\boldsymbol{x}_{p_1},\boldsymbol{x}_{p_1},\cdots,\boldsymbol{x}_{p_N}). \tag{1.6}$$

Then an anti-symmetric basis can be constructed as

$$|\alpha_1, \alpha_2, \cdots, \alpha_N\rangle \equiv \sqrt{N!}\hat{\mathcal{P}} \, |\alpha_1, \alpha_2, \cdots, \alpha_N) \tag{1.7}$$

whose completeness is

$$\frac{1}{N!} \sum_{\alpha_1, \cdots, \alpha_N} |\alpha_1, \cdots, \alpha_N\rangle \langle \alpha_1, \alpha_2, \cdots, \alpha_N| = 1. \tag{1.8}$$

Fock space $\mathcal{F}$ is defined as

$$\mathcal{F} \equiv \bigoplus_{n=0}^{\infty} F_n, \tag{1.9}$$

where

$$\begin{aligned} F_0 &= |0\rangle, \\ F_n &= \mathcal{H}_n, n = 1, 2, 3, \cdots \end{aligned} \tag{1.10}$$

The closure relation for Fock space is

$$|0\rangle \langle 0| + \sum_{N=1}^{\infty} \frac{1}{N!} \sum_{\alpha_1, \cdots, \alpha_N} |\alpha_1, \alpha_2, \cdots, \alpha_N\rangle \langle \alpha_1, \alpha_2, \cdots, \alpha_N| = 1. \tag{1.11}$$

In Fock space, the creation operator $\hat{a}_\lambda^\dagger$ is defined as

$$\hat{a}_\lambda^\dagger \, |\lambda_1, \cdots, \lambda_N\rangle \equiv \begin{cases} |\lambda, \lambda_1, \cdots, \lambda_N\rangle & \nexists \lambda_i = \lambda, \\ 0 & \exists \lambda_i = \lambda. \end{cases} \tag{1.12}$$

The annihilation operator $\hat{a}_\lambda$ is defined as the Hermitian adjoint of $\hat{a}_\lambda^\dagger$

$$\hat{a}_\lambda \equiv (\hat{a}_\lambda^\dagger)^\dagger. \tag{1.13}$$

It has the property

$$\hat{a}_\lambda |\lambda_1, \cdots, \lambda_N\rangle = \begin{cases} (-1)^{i-1} |\lambda_1, \cdots, \hat{\lambda}_i, \cdots, \lambda_N\rangle & \exists \lambda_i = \lambda, \\ 0 & \nexists \lambda_i = \lambda. \end{cases} \tag{1.14}$$

where $\hat{\lambda}_i$ means eliminate this λ_i. Particularly $\hat{a}_\lambda |0\rangle = 0$. According to the definition of creation operator

$$\left\{\hat{a}_\mu^\dagger, \hat{a}_\nu^\dagger\right\} = \hat{a}_\mu^\dagger \hat{a}_\nu^\dagger + \hat{a}_\nu^\dagger \hat{a}_\mu^\dagger = 0. \tag{1.15}$$

The Hermitian adjoint is

$$\{\hat{a}_\mu, \hat{a}_\nu\} = 0. \tag{1.16}$$

Due to the anti-symmetry of the basis upon which creation and annihilation operators are defined

$$\left\{\hat{a}_\mu, \hat{a}_\nu^\dagger\right\} = \delta_{\mu\nu}. \tag{1.17}$$

Next, we will express observables in term of creation and annihilation operators. Define the number operator

$$\hat{n}_\lambda \equiv \hat{a}_\lambda^\dagger \hat{a}_\lambda. \tag{1.18}$$

It has the property

$$\hat{n}_\lambda |\lambda_1, \lambda_2, \cdots, \lambda_N\rangle = \begin{cases} |\lambda_1, \lambda_2, \cdots, \lambda_N\rangle & \exists \lambda_i = \lambda, \\ 0 & \nexists \lambda_i = \lambda. \end{cases} \tag{1.19}$$

Define the total number operator

$$\hat{N} \equiv \sum_\lambda \hat{n}_\lambda. \tag{1.20}$$

It has the property

$$\hat{N} |\psi_N\rangle = N |\psi_N\rangle , \tag{1.21}$$

where N is the total number of electrons in the system of state $|\psi_N\rangle$. Any single particle operator $\hat{U} = \sum_i \hat{u}_i$ can be expressed in terms of number operators

$$\hat{U} = \sum_\alpha u_\alpha \hat{n}_\alpha, \tag{1.22}$$

where α is the diagonal representation of $\hat{u}$ with

$$\begin{aligned} \hat{u} |\alpha\rangle &= u_\alpha |\alpha\rangle , \\ \langle\beta|\ \alpha\rangle &= \delta_{\alpha\beta}. \end{aligned} \tag{1.23}$$

Define the pair counting operator

$$\hat{P}_{\alpha\beta} \equiv \hat{n}_\alpha \hat{n}_\beta - \delta_{\alpha\beta} \hat{n}_\alpha. \tag{1.24}$$

It has the property

$$\hat{P}_{\alpha\beta} |\lambda_1, \lambda_2, \cdots, \lambda_N\rangle = \begin{cases} |\lambda_1, \lambda_2, \cdots, \lambda_N\rangle & \exists i, j; \lambda_i = \alpha, \lambda_j = \beta, \\ 0 & \text{otherwise.} \end{cases} \tag{1.25}$$

In another form

$$\hat{P}_{\alpha\beta} = \hat{a}^\dagger_\alpha \hat{a}^\dagger_\beta \hat{a}_\beta \hat{a}_\alpha. \tag{1.26}$$

Any two particle operator $\hat{V} = \sum_{i \neq j} \hat{v}_{ij}$ can be expressed in terms of pair counting operator

$$\hat{V} = \frac{1}{2} \sum_{\alpha\beta} v_{\alpha\beta} \hat{P}_{\alpha\beta} = \frac{1}{2} \sum_{\alpha\beta} v_{\alpha\beta} \hat{a}^\dagger_\alpha \hat{a}^\dagger_\beta \hat{a}_\beta \hat{a}_\alpha, \tag{1.27}$$

where $\alpha\beta$ is the diagonal representation of $\hat{v}$ with

$$\begin{aligned} \hat{v}\,|\alpha\beta) &= v_{\alpha\beta}\,|\alpha\beta)\,, \\ (\alpha'\beta'|\,\alpha\beta) &= \delta_{\alpha\alpha'}\delta_{\beta\beta'}. \end{aligned} \tag{1.28}$$

Between two different representations α and β

$$|\alpha\rangle = \sum_{\beta} \langle\beta|\,\alpha\rangle\,|\beta\rangle\,. \tag{1.29}$$

The creation operators $\hat{a}^\dagger_\alpha$ and $\hat{a}^\dagger_\beta$ can be transformed as follows

$$\hat{a}^\dagger_\alpha = \sum_{\beta} \langle\beta|\,\alpha\rangle\,\hat{a}^\dagger_\beta. \tag{1.30}$$

Correspondingly

$$\hat{a}_\alpha = \sum_{\beta} \langle\alpha|\,\beta\rangle\,\hat{a}_\beta. \tag{1.31}$$

For a single particle operator

$$\hat{U} = \sum_{\alpha} u_\alpha \hat{a}^\dagger_\alpha \hat{a}_\alpha = \sum_{\beta\beta'} u_{\beta\beta'} \hat{a}^\dagger_\beta \hat{a}_{\beta'}. \tag{1.32}$$

For a two particle operator

$$\hat{V} = \frac{1}{2}\sum_{\alpha\alpha'} v_{\alpha\alpha'} \hat{a}^\dagger_\alpha \hat{a}^\dagger_{\alpha'} \hat{a}_{\alpha'} \hat{a}_\alpha = \frac{1}{2}\sum_{\beta_1\beta_2\beta_3\beta_4} v_{\beta_1\beta_2\beta_3\beta_4} \hat{a}^\dagger_{\beta_1} \hat{a}^\dagger_{\beta_2} \hat{a}_{\beta_4} \hat{a}_{\beta_3}. \tag{1.33}$$

In spin spacetime representation, let $\boldsymbol{x} = (\boldsymbol{r}, \sigma)$. The anti-commutation relations are

$$\begin{aligned} \left\{\hat{\psi}(\boldsymbol{x}), \hat{\psi}^\dagger(\boldsymbol{x}')\right\} &= \delta(\boldsymbol{x} - \boldsymbol{x}'), \\ \left\{\hat{\psi}^\dagger(\boldsymbol{x}), \hat{\psi}^\dagger(\boldsymbol{x}')\right\} &= \left\{\hat{\psi}(\boldsymbol{x}), \hat{\psi}(\boldsymbol{x}')\right\} = 0. \end{aligned} \tag{1.34}$$

We have the transformation to α representation

$$\begin{aligned}\hat{\psi}^\dagger(\boldsymbol{x}) &= \sum_\alpha \langle \alpha |\, \boldsymbol{x}\rangle\, \hat{a}_\alpha^\dagger = \sum_\alpha \phi_\alpha^*(\boldsymbol{x})\hat{a}_\alpha^\dagger, \\ \hat{\psi}(\boldsymbol{x}) &= \sum_\alpha \langle \boldsymbol{x} |\, \alpha\rangle\, \hat{a}_\alpha = \sum_\alpha \phi_\alpha(\boldsymbol{x})\hat{a}_\alpha.\end{aligned} \tag{1.35}$$

1.2 Equilibrium Green's Function

In the language of second quantization, the equilibrium Green's function will be defined and explored in the section. As a prerequisite, we first introduce pictures of quantum mechanics.

1.2.1 Pictures

Let $\hat{A}(t)$ be a general time-dependent unitary operator

$$\hat{A}^\dagger(t)\hat{A}(t) = 1 = \hat{A}(t)\hat{A}^\dagger(t). \tag{1.36}$$

Define a wavefunction and a operator in A picture as

$$\begin{aligned}|\psi(t)\rangle_A &\equiv \hat{A}(t)\,|\psi\rangle \\ \hat{O}(t)_A &\equiv \hat{A}(t)\hat{O}\hat{A}^\dagger(t)\end{aligned} \tag{1.37}$$

The expectation value of $\hat{O}$ in picture A is

$$\langle\psi|\hat{O}|\phi\rangle = \langle\psi_A|\hat{O}_A|\phi_A\rangle. \tag{1.38}$$

$\hat{A}(t) \equiv 1$ defines the Schrödinger picture. In the Schrödinger pciture, the time-

evolution operator $\hat{U}(t,t_0)_S$ is defined by

$$|\Psi(t)\rangle_S \equiv \hat{U}(t,t_0)_S\,|\Psi(t_0)\rangle\,. \tag{1.39}$$

It satisfies

$$i\frac{\partial}{\partial t}\hat{U}(t,t_0)_S = \hat{H}_S\hat{U}(t,t_0)_S \tag{1.40}$$

with $\hat{U}(t_0,t_0)_S = 1$. Note that Hartree atomic units are adopted so that $\hbar$, equal to 1, is dropped in the above equation. If the Hamiltonian $\hat{H}_S$ is explicitly time-independent, the above equation has a solution

$$\hat{U}(t,t_0)_S = \exp\left[-i\hat{H}_S(t-t_0)\right]. \tag{1.41}$$

In general

$$\hat{U}^\dagger(t,t_0)_S = \hat{U}^{-1}(t,t_0)_S = \hat{U}(t_0,t)_S. \tag{1.42}$$

$\hat{A}(t) \equiv \hat{U}^\dagger(t,t_0)_S$ defines the Heisenberg picture. In the Heisenberg picture, we have the Heisenberg equation of motion

$$i\frac{\mathrm{d}}{\mathrm{d}t}\hat{O}(t)_H = [\hat{O}_H,\hat{H}_H] + i\left[\frac{\partial\hat{O}_S}{\partial t}\right]_H, \tag{1.43}$$

where

$$\left[\frac{\partial\hat{O}_S}{\partial t}\right]_H \equiv \hat{U}_S^\dagger\left(\frac{\partial\hat{O}_S}{\partial t}\right)\hat{U}_S. \tag{1.44}$$

Let $\hat{H}_0$ be the easy part (time-independent and non-interacting) of the whole Hamiltonian $\hat{H}_S = \hat{H}_0 + \hat{V}_S$, then $\hat{A}(t) \equiv \exp\left(i\hat{H}_0 t\right)$ defines the interaction picture. In the interaction picture, an operator evolves according to

$$i\frac{\mathrm{d}}{\mathrm{d}t}\hat{O}(t)_I = \left[\hat{O}_I,\hat{H}_0\right] + i\left[\frac{\partial\hat{O}_S}{\partial t}\right]_I, \tag{1.45}$$

where

$$\left[\frac{\partial \hat{O}_S}{\partial t}\right]_I \equiv \exp\left(i\hat{H}_0 t\right)\left(\frac{\partial \hat{O}_S}{\partial t}\right)\exp\left(-i\hat{H}_0 t\right). \tag{1.46}$$

A wavefunction evolves according to

$$i\frac{\partial}{\partial t}\left|\Psi(t)\right\rangle_I = \hat{V}(t)_I\left|\Psi(t)\right\rangle_I. \tag{1.47}$$

Define a time-evolution operator $\hat{U}(t,t')_I$ by

$$\left|\Psi(t)\right\rangle_I = \hat{U}(t,t')_I\left|\Psi(t')\right\rangle_I. \tag{1.48}$$

It satisfies

$$i\frac{\partial}{\partial t}\hat{U}(t,t')_I = \hat{V}(t)_I\hat{U}(t,t')_I. \tag{1.49}$$

A formal solution to the above equation is

$$\begin{aligned}\hat{U}(t,t')_I =& \hat{T}\sum_{n=0}^{\infty}\frac{(-i)^n}{n!}\int_{t'}^{t}\mathrm{d}t_1\cdots\int_{t'}^{t}\mathrm{d}t_n\hat{V}(t_1)_I\cdots\hat{V}(t_n)_I \\ =& \hat{T}\exp\left[-i\int_{t'}^{t}\mathrm{d}\tau\hat{V}(\tau)_I\right],\end{aligned} \tag{1.50}$$

where the time-ordering operator $\hat{T}$ is defined by

$$\hat{T}\left[\hat{A}(t_1)\hat{B}(t_2)\right] \equiv \begin{cases}\hat{A}(t_1)\hat{B}(t_2) & \text{if } t_1 > t_2, \\ \hat{B}(t_2)\hat{A}(t_1) & \text{if } t_2 > t_1.\end{cases} \tag{1.51}$$

The transformation of the time-evolution operator between the Schrödinger picture and the interaction picture follows

$$\hat{U}(t,t')_I = \exp\left(i\hat{H}_0 t\right)\hat{U}(t,t')_S\exp\left(-i\hat{H}_0 t'\right). \tag{1.52}$$

The transformation of operators between the interacting picture and the Heisenberg picture follows

$$\hat{O}(t)_H = \hat{U}(0,t)_I \hat{O}(t)_I \hat{U}(t,0)_I. \tag{1.53}$$

Both the creation and annihilation operators in the interaction picture differ from those in the Schrödinger picture by just a phase factor

$$\begin{aligned} \hat{c}_i(t)_I &= e^{-i\epsilon_i t}\hat{c}_i, \\ \hat{c}_i^\dagger(t)_I &= e^{i\epsilon_i t}\hat{c}_i^\dagger. \end{aligned} \tag{1.54}$$

1.2.2 Definition and Properties

Define the time-ordered product of two creation and annihilation operators by

$$\hat{T}\big[\hat{A}(t)\hat{B}(t')\big] \equiv \begin{cases} \hat{A}(t)\hat{B}(t') & \text{if } t > t', \\ -\hat{B}(t')\hat{A}(t) & \text{if } t' > t. \end{cases} \tag{1.55}$$

Let $|\Psi_0\rangle$ be the ground state for some Hamiltonian H. The Green's function in a general λ representation is defined by

$$iG(\lambda t, \lambda' t') \equiv \frac{1}{\langle \Psi_0 |\ \Psi_0\rangle} \langle \Psi_0 | \hat{T}[c_\lambda(t)_H c_{\lambda'}^\dagger(t')_H] | \Psi_0 \rangle. \tag{1.56}$$

In the spin spacetime representation

$$iG(\boldsymbol{x}t, \boldsymbol{x}'t') \equiv \frac{1}{\langle \Psi_0 |\ \Psi_0\rangle} \langle \Psi_0 | \hat{T}[\psi(\boldsymbol{x}t)_H \psi^\dagger(\boldsymbol{x}'t')_H] | \Psi_0 \rangle, \tag{1.57}$$

or with the spin indices explicitly

$$iG_{\alpha\beta}(\boldsymbol{r}t, \boldsymbol{r}'t') \equiv \frac{1}{\langle \Psi_0 |\ \Psi_0\rangle} \langle \Psi_0 | \hat{T}[\psi_\alpha(\boldsymbol{r}t)_H \psi_\beta^\dagger(\boldsymbol{r}'t')_H] | \Psi_0 \rangle. \tag{1.58}$$

In the spin momentum representation

$$iG_{\alpha\beta}(\boldsymbol{k}t,\boldsymbol{k}'t') \equiv \frac{1}{\langle\Psi_0|\ \Psi_0\rangle}\langle\Psi_0|\hat{T}[c_{\boldsymbol{k}\alpha}(t)_H c^\dagger_{\boldsymbol{k}'\beta}(t')_H]|\Psi_0\rangle. \tag{1.59}$$

If the Hamiltonian is explicitly time-independent, the Green's function depends only on the time-difference $(t-t')$

$$\hat{H} \neq \hat{H}(t) \implies G(\lambda t,\lambda' t') = G(\lambda,\lambda',t-t'). \tag{1.60}$$

If the Hamiltonian commutes with the total-momentum operator $\hat{\boldsymbol{P}}$

$$\hat{\boldsymbol{P}} = \sum_\alpha \int \mathrm{d}\boldsymbol{r}\hat{\psi}^\dagger_\alpha(\boldsymbol{r})(-i\boldsymbol{\nabla})\hat{\psi}_\alpha(\boldsymbol{r}), \tag{1.61}$$

the Green's function only depends on the difference between the space coordinates $(\boldsymbol{r}-\boldsymbol{r}')$

$$[\hat{H},\hat{\boldsymbol{P}}] = 0 \implies G_{\alpha\beta}(\boldsymbol{r}t,\boldsymbol{r}'t') = G_{\alpha\beta}(\boldsymbol{r}-\boldsymbol{r}',t,t'). \tag{1.62}$$

Then we have the Fourier transform

$$G_{\alpha\beta}(\boldsymbol{k},t,t') = \int \mathrm{d}(\boldsymbol{r}-\boldsymbol{r}')e^{-i\boldsymbol{k}\cdot(\boldsymbol{r}-\boldsymbol{r}')}G_{\alpha\beta}(\boldsymbol{r}t,\boldsymbol{r}'t'), \tag{1.63}$$

and the inverse transformation

$$G_{\alpha\beta}(\boldsymbol{r}t,\boldsymbol{r}'t') = \int \frac{\mathrm{d}\boldsymbol{k}}{(2\pi)^3}e^{i\boldsymbol{k}\cdot(\boldsymbol{r}-\boldsymbol{r}')}G_{\alpha\beta}(\boldsymbol{k},t,t'). \tag{1.64}$$

Furthermore

$$[\hat{H},\hat{\boldsymbol{P}}] = 0 \implies G_{\alpha\beta}(\boldsymbol{k}t,\boldsymbol{k}'t') = \delta_{\boldsymbol{k}\boldsymbol{k}'}G_{\alpha\beta}(\boldsymbol{k},t,t'), \tag{1.65}$$

where $G_{\alpha\beta}(\boldsymbol{k}t, \boldsymbol{k}'t')$ is the momentum Green's function defined in Eqn. 1.59 and $G_{\alpha\beta}(\boldsymbol{k}, t, t')$ is the Fourier transform of the space Green's function. If the Hamiltonian both commutes with the total momentum and is explicitly time-independent, the Green's function writes

$$G_{\alpha\beta}(\boldsymbol{r}t, \boldsymbol{r}'t') = G_{\alpha\beta}(\boldsymbol{r} - \boldsymbol{r}', t - t'). \tag{1.66}$$

In this case, the Fourier transform is

$$G_{\alpha\beta}(\boldsymbol{k}, \omega) = \int \mathrm{d}(\boldsymbol{r} - \boldsymbol{r}')\mathrm{d}(t - t')e^{-i\boldsymbol{k}\cdot(\boldsymbol{r}-\boldsymbol{r}')}e^{i\omega(t-t')}G_{\alpha\beta}(\boldsymbol{r}t, \boldsymbol{r}'t'). \tag{1.67}$$

The inverse transformation is

$$G_{\alpha\beta}(\boldsymbol{r}t, \boldsymbol{r}'t') = \frac{1}{(2\pi)^4}\int \mathrm{d}\boldsymbol{k}\mathrm{d}\omega e^{i\boldsymbol{k}\cdot(\boldsymbol{r}-\boldsymbol{r}')}e^{-i\omega(t-t')}G_{\alpha\beta}(\boldsymbol{k}, \omega). \tag{1.68}$$

Given the Green's function, the following quantities can be calculated. 1) The ground-state expectation value of any single-particle operator. 2) The ground-state energy of the system. 3) The excitation energies of the system.

1.3 Perturbation Theory

In this section, we explore the perturbation theory which relates the full Green's function (with interaction) to the free ones (without interaction).

1.3.1 Perturbation Expansion

Assume a Hamiltonian

$$\hat{H}_\varepsilon(t)_S \equiv \hat{H}_0 + e^{-\varepsilon|t|}\hat{v} \tag{1.69}$$

with $\varepsilon > 0$ and H_0 being the easy part. Let $|\Phi_0\rangle$ be the ground state for $\hat{H}_0$. Let $|\Psi_0\rangle$ be the ground state for $\hat{H}_{\varepsilon\to 0}(0)_S$. At $t = 0$, the Schrödinger, Heisenberg and interaction pictures coincide. Let

$$|\Psi_\varepsilon(0)\rangle \equiv |\Psi_\varepsilon(0)\rangle_I = \hat{U}_\varepsilon(0, -\infty)_I \, |\Phi_0\rangle \, . \tag{1.70}$$

Gell-Mann–Low theorem states that if the vector $|\xi\rangle = \lim_{\varepsilon\to 0} \frac{|\Psi_\varepsilon(0)\rangle}{\langle\Phi_0|\,\Psi_\varepsilon(0)\rangle}$ exists to all orders in perturbation theory, then $|\xi\rangle$ is an exact eigen function of $\hat{H}_{\varepsilon\to 0}(0)_S$.[58] Hopefully

$$|\Psi_0\rangle = \lim_{\varepsilon\to 0} |\Psi_\varepsilon(0)\rangle \, . \tag{1.71}$$

Using Eqn. 1.50, 1.53, and 1.71, we have

$$\begin{aligned} iG(\lambda t, \lambda' t') &= \frac{\langle\Psi_0|\hat{T}[\hat{c}_\lambda(t)_H \hat{c}^\dagger_{\lambda'}(t')_H]|\Psi_0\rangle}{\langle\Psi_0|\,\Psi_0\rangle} \\ = \lim_{\varepsilon\to 0} \Bigg[&\frac{1}{\langle\Phi_0|\hat{U}_\varepsilon(\infty, -\infty)_I|\Phi_0\rangle} \sum_{n=0}^{\infty} \frac{(-i)^n}{n!} \int_{-\infty}^{\infty} \mathrm{d}t_1 \cdots \int_{-\infty}^{\infty} \mathrm{d}t_n \\ &\times e^{-\varepsilon(|t_1|+\cdots+|t_n|)} \langle\Phi_0| \, \hat{T} \left[\hat{v}(t_1)_I \cdots \hat{v}(t_n)_I \hat{c}_\lambda(t)_I \hat{c}^\dagger_{\lambda'}(t')_I \right] |\Phi_0\rangle \Bigg]. \end{aligned} \tag{1.72}$$

1.3.2 Wick's Theorem

As an operator equality, Wick's theorem expresses a product of creation and annihilation operators as a sum of the products of contractions and normal ordered products.

Let $\hat{a}^\dagger_i$ and $\hat{b}^\dagger_i$ ($\hat{a}_i$ and $\hat{b}_i$) be the creation (annihilation) operators for particles and holes respectively. For a product of creation and annihilation operators, define the normal order operator $\hat{N}$ which brings the annihilation operators to the right, and multiplies the product with the sign of the permutations applied. For example

$$\hat{N}[\hat{b}_i(t_1)_I \hat{a}^\dagger_j(t_2)_I \hat{b}^\dagger_k(t_3)_I] = (-1)^2 \hat{a}^\dagger_j(t_2)_I \hat{b}^\dagger_k(t_3)_I \hat{b}_i(t_1)_I . \tag{1.73}$$

Let $\hat{A}\hat{B}\cdots\hat{Z}$ be some creation and annihilation operators. Define the paring of two operators by

$$\hat{A}\hat{B} \equiv \hat{A}\hat{B} - \hat{N}\big(\hat{A}\hat{B}\big) \tag{1.74}$$

For example,

$$\begin{aligned}\hat{a}_i(t)_I\hat{a}_j^\dagger(t')_I =& e^{i\epsilon_j(t'-t)}\delta_{ij},\\ \hat{b}_i(t)_I\hat{b}_j^\dagger(t')_I =& e^{i\epsilon_j(t-t')}\delta_{ij}.\end{aligned} \tag{1.75}$$

All other pairings vanish. Thus any pairing is a c-number. Since $\langle\Phi_0|\hat{N}\big(\hat{A}\hat{B}\big)|\Phi_0\rangle = 0$,

$$\langle\Phi_0|\hat{A}\hat{B}|\Phi_0\rangle = \langle\Phi_0|\hat{N}\big(\hat{A}\hat{B}\big) + \hat{A}\hat{B}|\Phi_0\rangle = \hat{A}\hat{B}. \tag{1.76}$$

Define the normal ordering for a product with pairings

$$\hat{N}\big(\hat{A}\hat{B}\hat{C}\hat{D}\hat{E}\cdots\hat{X}\hat{Y}\hat{Z}\big) \equiv (-1)^q\hat{A}\hat{D}\hat{C}\hat{Y}\hat{N}\big(\hat{B}\hat{E}\cdots\hat{X}\hat{Z}\big). \tag{1.77}$$

Here q is the number of commutations needed to bring the paired operators to the left of the product. The *Wick's theorem for normal products* states that

$$\begin{aligned}\hat{A}_1\hat{A}_2\cdots\hat{A}_n =& \hat{N}\big(\hat{A}_1\cdots\hat{A}_n\big)\\ &+\hat{N}\big(\hat{A}_1\hat{A}_2\hat{A}_3\cdots\hat{A}_n\big) + \hat{N}\big(\hat{A}_1\hat{A}_2\hat{A}_3\cdots\hat{A}_n\big)\\ &+\cdots\text{all other one pairing terms}\\ &+\hat{N}\big(\hat{A}_1\hat{A}_2\cdots\hat{A}_n\big)\\ &+\cdots\text{all other two pairing terms}+\\ &\ \vdots\\ &+\text{all completely paired terms.}\end{aligned} \tag{1.78}$$

For time ordered products, define the contraction by

$$\overbrace{\hat{A}(t)\hat{B}(t')} \equiv \hat{T}\big(\hat{A}(t)\hat{B}(t')\big) - \hat{N}\big(\hat{A}(t)\hat{B}(t')\big). \tag{1.79}$$

The contraction is related to the pairing by

$$\overbrace{\hat{A}(t)\hat{B}(t')} = \begin{cases} \underbrace{\hat{A}(t)\hat{B}}(t') & \text{if } t > t', \\ -\underbrace{\hat{B}(t')\hat{A}}(t) & \text{if } t' > t. \end{cases} \tag{1.80}$$

Therefore, contractions are c-numbers, so that

$$\big\langle \Phi_0 \big| \hat{T}\big(\hat{A}(t)\hat{B}(t')\big) \big| \Phi_0 \big\rangle = \overbrace{\hat{A}(t)\hat{B}(t')}. \tag{1.81}$$

According to the properties of pairings

$$\hat{N}\big(\overbrace{\hat{A}\hat{B}\overbrace{\hat{C}\hat{D}}\hat{E}\cdots\hat{X}\hat{Y}}\hat{Z}\big) \equiv (-1)^q \overbrace{\hat{A}\hat{D}}\overbrace{\hat{C}\hat{Y}}\hat{N}\big(\hat{B}\hat{E}\cdots\hat{X}\hat{Z}\big). \tag{1.82}$$

The *Wick's theorem for time-ordered products* states that[59]

$$\begin{aligned} \hat{T}\big(\hat{A}_1\hat{A}_2\cdots\hat{A}_n\big) =& \hat{N}\big(\hat{A}_1\cdots\hat{A}_n\big) \\ &+\hat{N}\big(\overbrace{\hat{A}_1\hat{A}_2}\hat{A}_3\cdots\hat{A}_n\big) + \hat{N}\big(\hat{A}_1\overbrace{\hat{A}_2\hat{A}_3}\cdots\hat{A}_n\big) \\ &+\cdots \text{all other one contraction terms} \\ &+\hat{N}\big(\overbrace{\hat{A}_1\hat{A}_2}\cdots\hat{A}_n\big) \\ &+\cdots \text{all other two contraction terms}+ \\ &\vdots \\ &+\text{all completely contracted terms.} \end{aligned} \tag{1.83}$$

If $\hat{H}_0$ is explicitly time-independent, $\overbrace{\hat{c}_i(t)_I\hat{c}_j^\dagger(t')_I}$ is the $\hat{H}_0$-propagator (free

Green's function)

$$\begin{aligned} iG^0(it, jt') =& \left\langle \Phi_0 \middle| \hat{T}\left[\hat{c}_i(t)_H \hat{c}_j^\dagger(t')_H\right] \middle| \Phi_0 \right\rangle \\ =& \left\langle \Phi_0 \middle| \hat{T}\left[\hat{c}_i(t)_I \hat{c}_j^\dagger(t')_I\right] \middle| \Phi_0 \right\rangle \\ =& \overbrace{\hat{c}_i(t)_I \hat{c}_j^\dagger(t')_I}. \end{aligned}$$

While other contractions are zero

$$\overbrace{\hat{c}_i(t)_I \hat{c}_j}(t')_I = \ 0 \ = \overbrace{\hat{c}_i^\dagger(t)_I \hat{c}_j^\dagger}(t')_I. \tag{1.84}$$

Similarly for field operators

$$\overbrace{\hat{\psi}(\boldsymbol{x}t)_I \hat{\psi}^\dagger}(\boldsymbol{x}'t')_I = iG^0(\boldsymbol{x}t, \boldsymbol{x}'t'), \tag{1.85}$$

and

$$\overbrace{\hat{\psi}(\boldsymbol{x}t)_I \hat{\psi}}(\boldsymbol{x}'t')_I = \ 0 \ = \overbrace{\hat{\psi}^\dagger(\boldsymbol{x}t)_I \hat{\psi}^\dagger}(\boldsymbol{x}'t')_I. \tag{1.86}$$

1.3.3 Diagrammatic Calculations

The Green's function in λ representation is given in Eqn. 1.72. We set $\lambda = i$ to be discrete in the following. The Green's function in the spin spacetime representation writes

$$\begin{aligned} & iG_{\alpha\beta}(\boldsymbol{r}t, \boldsymbol{r}'t') = \\ & \lim_{\varepsilon \to 0} \left[\frac{1}{\langle \Phi_0 | \hat{U}_\varepsilon(\infty, -\infty)_I | \Phi_0 \rangle} \sum_{n=0}^{\infty} \frac{(-i)^n}{n!} \int_{-\infty}^{\infty} \mathrm{d}t_1 \cdots \int_{-\infty}^{\infty} \mathrm{d}t_n \right. \\ & \left. \times e^{-\varepsilon(|t_1| + \cdots + |t_n|)} \left\langle \Phi_0 \right| \hat{T}\left[\hat{v}(t_1)_I \cdots \hat{v}(t_n)_I \hat{\psi}(\boldsymbol{r}t)_I \hat{\psi}^\dagger(\boldsymbol{r}'t')_I \right] \left| \Phi_0 \right\rangle \right]. \end{aligned} \tag{1.87}$$

Let

$$\hat{v}(t)_I = \frac{1}{2}\sum_{ijkl}\langle ij|v|kl\rangle \hat{c}_i^\dagger(t)_I \hat{c}_j^\dagger(t)_I \hat{c}_l(t)_I \hat{c}_k(t)_I \tag{1.88}$$

for a discrete representation and

$$\hat{v}(t)_I = \frac{1}{2}\int \mathrm{d}\boldsymbol{x}\int \mathrm{d}\boldsymbol{x}' v(\boldsymbol{x},\boldsymbol{x}')\hat{\psi}^\dagger(\boldsymbol{x}t)_I \hat{\psi}^\dagger(\boldsymbol{x}'t)_I \hat{\psi}(\boldsymbol{x}'t)_I \hat{\psi}(\boldsymbol{x}t)_I \tag{1.89}$$

for the spin spacetime representation. Apply Wick's theorem to Eqn. 1.72 and Eqn. 1.87, the nth order term becomes

$$\begin{aligned}\frac{(-i)^n}{n!2^n}\times\left\{\begin{array}{l}\sum_{ijkl}\cdots \\ \int \mathrm{d}\boldsymbol{x}_1\int \mathrm{d}\boldsymbol{x}_1'\cdots\end{array}\right\}\int \mathrm{d}^n t e^{-\varepsilon(|t_1|\cdots)} \\ \times\sum(\pm)\underbrace{\langle v\rangle\cdots\langle v\rangle}_{n\text{ factors}}\underbrace{(iG^0)\cdots(iG^0)}_{(2n+1)\text{ factors}}.\end{aligned} \tag{1.90}$$

Eqn. 1.90 can be evaluated in a diagrammatic way invented by Feynman.[60] The recipe for translating the above equation to a diagram is as follows.

1. Imagine a time-axis with time increasing from below to above.

2. The H_0-propagator $G^0(\lambda t,\lambda' t')$ is represented by a continuous line from $(\lambda' t')$ to (λt). An arrow is drawn on the line pointing from the second to the first argument. The endpoints are ordered in time; the length, curvature or tilt of the lines do not matter. The diagram for $G^0(\lambda t,\lambda' t')$ is shown in Fig. 1.1.

3. The matrix elements of the interaction are represented by a wiggly line with the endpoints labeled according to Fig. 1.2. The points where the interaction lines are connected to propagators are called internal vertices.

4. Green's functions with equal time-arguments shall be interpreted as $G^0(\lambda t,\lambda' t^+)$.

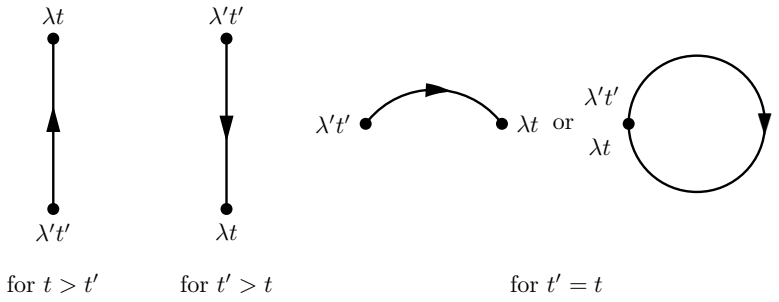

Figure 1.1: Diagrams for the H_0-propagator $G^0(\lambda t, \lambda' t')$.

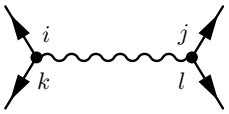

Figure 1.2: Diagram for the interaction matrix element $\langle ij|\hat{v}|kl\rangle$.

5. All indexes for an internal vertex shall be summed or integrated over. The factor $e^{-\varepsilon|t|}$ shall be added to the integrals over time.

6. The sign of any term is $(-1)^l$ where l is the number of closed loops formed by G^0-lines.

7. The prefactor of each term of nth order is

$$\frac{i^n}{n!2^n}. \tag{1.91}$$

The above rules are also valid for the vacuum amplitude. For example, the diagram in Fig. 1.3 represents the term

$$(-1)^1 \frac{i^2}{2!2^2} \sum_{pqrs} \sum_{jkmn} \int \mathrm{d}t_1 \int \mathrm{d}t_2 e^{-\varepsilon(|t_1|+|t_2|)} \langle pq|\hat{v}|rs\rangle \langle jk|\hat{v}|mn\rangle$$
$$\times G^0(mt_1, pt_2) G^0(st_2, jt_1) G^0(nt_1, qt_2) G^0(rt_2, kt_1). \tag{1.92}$$

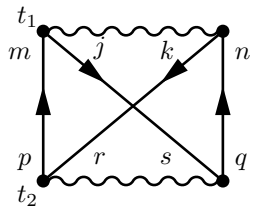

Figure 1.3: A second order vacuum amplitude diagram.

For the vacuum amplitude, the Linked-Cluster theorem by Goldstone states that [61]

$$\left\langle \Phi_0 \middle| \hat{U}_I \middle| \Phi_0 \right\rangle = \exp\left[\left\langle \Phi_0 \middle| \hat{U}_I \middle| \Phi_0 \right\rangle_L \right]. \tag{1.93}$$

Here $\left\langle \Phi_0 \middle| \hat{U}_I \middle| \Phi_0 \right\rangle_L$ means that only connected diagrams are included in the sum. For the Green's function, all terms of the numerator are obtained from the product of all connected diagrams which connect the two external endpoints with all diagrams of the vacuum amplitude. Thus the denominator cancels.

For any graph in the expansion of the Green's function, the remaining part after excluding the connections to the external end points is a self-energy insertion. The sum of all self-energy insertions is the self-energy $\tilde{M}$ which is illustrated in Fig. 1.4. A

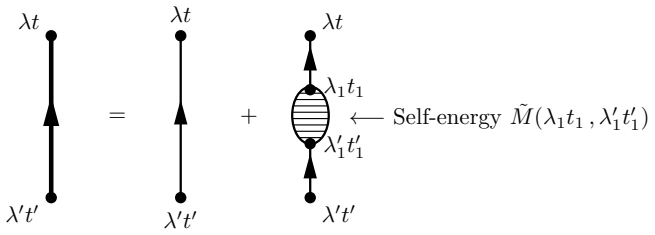

Figure 1.4: Diagrammatic representation of the self-energy $\tilde{M}$. The thick line represents the full Green's function.

self-energy insertion is called *reducible* if it can be partitioned into a lower-order self-energy insertion by cutting a single G^0-line. The sum of all irreducible self-energy insertions is called *proper self-energy* M. The self-energy can be obtained from the proper self-energy, as shown in Fig. 1.5. The Green's function is related to the proper

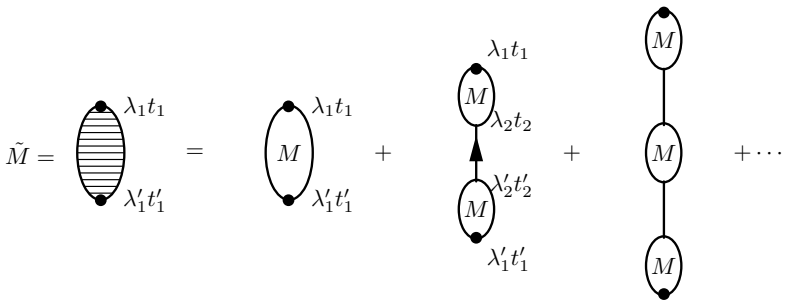

Figure 1.5: The self-energy $\tilde{M}$ expressed in terms of the proper self-energy M.

self-energy by *Dyson's equation* as shown in Eqn. 1.94 and illustrated in Fig. 1.6.

$$G(\lambda t, \lambda' t') = G^0(\lambda t, \lambda' t') + \sum_{\lambda_1} \sum_{\lambda_1'} \int \mathrm{d}t_1 \int \mathrm{d}t_1' G^0(\lambda t, \lambda_1 t_1) M(\lambda_1 t_1, \lambda_1' t_1') G(\lambda_1' t_1', \lambda' t'). \tag{1.94}$$

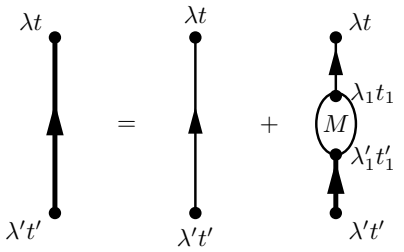

Figure 1.6: Diagramatic representation of Dyson's equation. The thick line represents the full Green's function. M is the proper self-energy.

1.4 Non-equilibrium Green's Function

A system out of equilibrium may not go back to its ground state at $t \to \infty$. In this case Gell-Mann–Low theorem doesn't apply for $0 \leq t < \infty$. However a systematic theoretical framework for obtaining non-equilibrium properties can still be established with the aid of a contour ordered integral. The non-equilibrium many-particle formalism is structurally parallel to the equilibrium one. In this section, we will focus on the non-equilibrium Green's function.

1.4.1 Definition and Properties

Consider the Hamiltonian

$$\hat{H} = \hat{H}_0 + \hat{H}_i + \hat{H}'(t), \tag{1.95}$$

where $\hat{H}_0$ is the easy part (time-independent and non-interacting), $\hat{H}_i$ contains many-body interaction, and $\hat{H}'(t)$ is time dependent. $\hat{H}'(t)$ drives the system to non-equilibrium. To approach non-equilibrium properties, assume the system is in equilibrium at the beginning and the non-equilibrium part is turned on at $t = t_0$. Before t_0, the system is described by the equilibrium density matrix

$$\hat{\rho}(\hat{h}) = \frac{\exp(-\beta\hat{h})}{\mathrm{Tr}\left[\exp(-\beta\hat{h})\right]}, \tag{1.96}$$

where $\hat{h} = \hat{H}_0 + \hat{H}_i$. After the non-equilibrium part is turned on, assume the thermal dynamics is still governed by $\hat{\rho}(\hat{h})$. Then the task is to calculate

$$\langle \hat{O}(t) \rangle = \mathrm{Tr}\left[\hat{\rho}(\hat{h})\hat{O}_H(t)\right]. \tag{1.97}$$

The expectation of an operator $\hat{O}(t)$ can be expressed in terms of contour-ordered Green's functions $G(1, 1')$ defined by

$$iG(1, 1') \equiv \langle \hat{T}_C[\hat{\psi}_H(1)\hat{\psi}^\dagger_H(1')] \rangle, \tag{1.98}$$

where $(1) \equiv (\boldsymbol{x}_1 t_1)$ and the contour ordering operator $\hat{T}_C$ brings the later (on the contour C) field operator to the left. C is a time contour and illustrated in Fig. 1.7. The contour-ordered Green's function in Eqn. 1.98 contains four different cases:

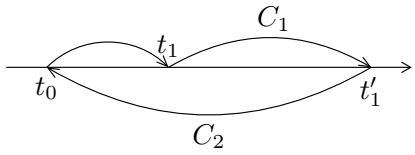

Figure 1.7: Contour C.

$$G(1,1') = \begin{cases} G_C(1,1') & t_1, t_{1'} \in C_1 \\ G^{>}(1,1') & t_1 \in C_2, t_{1'} \in C_1 \\ G^{<}(1,1') & t_1 \in C_1, t_{1'} \in C_2 \\ G_{\tilde{C}}(1,1') & t_1, t_{1'} \in C_2 \end{cases} \tag{1.99}$$

In detail, the *Causal* or *time-ordered* Green's function G_C

$$\begin{aligned} G_C(1,1') &= -i\langle \hat{T}_C[\hat{\psi}_H(1)\hat{\psi}_H^\dagger(1')]\rangle \\ &= -i\theta(t_1 - t_{1'})\langle \hat{\psi}_H(1)\hat{\psi}_H^\dagger(1')\rangle + i\theta(t_{1'} - t_1)\langle \hat{\psi}_H^\dagger(1')\hat{\psi}_H(1)\rangle, \end{aligned} \tag{1.100}$$

the *greater* Green's function $G^>$

$$G^{>}(1,1') = -i\langle \hat{\psi}_H(1)\hat{\psi}_H^\dagger(1')\rangle, \tag{1.101}$$

the *lesser* Green's function $G^<$

$$G^{<}(1,1') = +i\langle \hat{\psi}_H^\dagger(1')\hat{\psi}_H(1)\rangle, \tag{1.102}$$

and the *antitime-ordered* Green's function $G_{\tilde{C}}$

$$\begin{aligned} G_{\tilde{C}}(1,1') &= -i\langle \tilde{\hat{T}}_C[\hat{\psi}_H(1)\hat{\psi}_H^\dagger(1')]\rangle \\ &= -i\theta(t_{1'} - t_1)\langle \hat{\psi}_H(1)\hat{\psi}_H^\dagger(1')\rangle + i\theta(t_1 - t_{1'})\langle \hat{\psi}_H^\dagger(1')\hat{\psi}_H(1)\rangle. \end{aligned} \tag{1.103}$$

The above four Green's functions are linearly dependent, i.e.

$$G_C + G_{\tilde{C}} = G^{<} + G^{>}. \tag{1.104}$$

Furthermore, the advanced Green's function is defined as

$$\begin{aligned} G^a(1,1') \equiv & i\theta(t_{1'}-t_1)\langle\{\hat{\psi}_H(1),\hat{\psi}_H^\dagger(1')\}\rangle \\ = & \theta(t_{1'}-t_1)[G^<(1,1')-G^>(1,1')], \end{aligned} \tag{1.105}$$

and the retarded Green's function is defined as

$$\begin{aligned} G^r(1,1') \equiv & -i\theta(t_1-t_{1'})\langle\{\hat{\psi}_H(1),\hat{\psi}_H^\dagger(1')\}\rangle \\ = & \theta(t_1-t_{1'})[G^>(1,1')-G^<(1,1')]. \end{aligned} \tag{1.106}$$

Thus we have $G^r - G^a = G^> - G^<$.

The contour-ordered Green's function can be transformed into a form for which Wick's theorem can be applied. Let

$$\hat{H}'_h(t) = \exp[i\hat{h}(t-t_0)]\hat{H}'(t)\exp[-i\hat{h}(t-t_0)], \tag{1.107}$$

and

$$\hat{v}_h(t,t_0) = \hat{T}\left\{\exp\left[-i\int_{t_0}^{t} \mathrm{d}t'\hat{H}'_h(t')\right]\right\}. \tag{1.108}$$

Then

$$\hat{\psi}_H(t) = \hat{v}_h^\dagger(t,t_0)\hat{\psi}_h(t)\hat{v}_h(t,t_0). \tag{1.109}$$

Using Eqn. 1.109, we have

$$iG(1,1') = \langle\hat{T}_C[\hat{S}_C^H\hat{\psi}_h(1)\hat{\psi}_h^\dagger(1')]\rangle, \tag{1.110}$$

where

$$\hat{S}_C^H = \exp\left[-i\int_C \mathrm{d}\tau\hat{H}'_h(\tau)\right]. \tag{1.111}$$

Replacing the h-dependence by H_0-dependence, we have[62]

$$iG(1,1') = \frac{\mathrm{Tr}\left\{\hat{\rho}_0 \hat{T}_{C_v}[\hat{S}^i_{C_v}\hat{S}'_C \psi_{H_0}(1)\psi^\dagger_{H_0}(1')]\right\}}{\mathrm{Tr}[\rho_0 \hat{T}_{C_v}(\hat{S}^i_{C_v}\hat{S}'_C)]}, \tag{1.112}$$

where the density matrix

$$\hat{\rho}_0 = \frac{\exp(-\beta \hat{H}_0)}{\mathrm{Tr}[\exp(-\beta \hat{H}_0)]}, \tag{1.113}$$

and

$$\begin{aligned} \hat{S}'_C &= \exp\left[-i\int_C \mathrm{d}\tau \hat{H}'_{H_0}(\tau)\right], \\ \hat{S}^i_{C_v} &= \exp\left[-i\int_{C_v} \mathrm{d}\tau \hat{H}^i_{H_0}(\tau)\right]. \end{aligned} \tag{1.114}$$

The contour C_v is illustrated in Fig. 1.8. After Eqn. 1.112 is expanded into perturbation series, Wick's theorem and diagrammatic analyses can be applied.

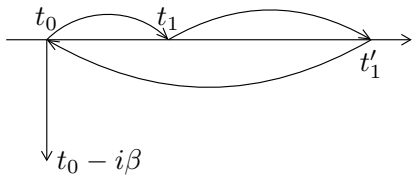

Figure 1.8: Contour C_v.

Parallel to the equilibrium theory, we have Dyson's equation for non-equilibrium cases

$$\begin{aligned} G(1,1') = G_0(1,1') &+ \int \mathrm{d}\boldsymbol{x}_2 \int_{C_v} \mathrm{d}\tau_2 G_0(1,2)U(2)G(2,1') \\ &+ \int \mathrm{d}\boldsymbol{x}_2 \int \mathrm{d}\boldsymbol{x}_3 \int_{C_v} \mathrm{d}\tau_2 \int_{C_v} \mathrm{d}\tau_3 G_0(1,2)\Sigma(2,3)G(3,1'), \end{aligned} \tag{1.115}$$

where U is the non-equilibrium term of Eqn. 1.95 in mean field approximation. In order to make the calculations feasible, Langreth theorem can be applied to relate a contour integral to a real axis integral.[63] For example

$$C^<(t_1, t_{1'}) = \int_C \mathrm{d}\tau A(t_1,\tau)B(\tau, t_{1'})$$

Contour	Real axis
$C = \int_C AB$	$C^< = \int_t [A^r B^< + A^< B^a]$
	$C^r = \int_t A^r B^r$
$D = \int_C ABC$	$D^< = \int_t [A^r B^r C^< + A^r B^< C^a + A^< B^a C^a]$
	$D^r = \int_t A^r B^r C^r$
$C(\tau, \tau') = A(\tau, \tau')B(\tau, \tau')$	$C^<(t, t') = A^<(t, t')B^<(t, t')$
	$C^r(t, t') = A^<(t, t')B^r(t, t') + A^r(t, t')B^<(t, t')$ $A^r(t, t')B^r(t, t')$
$D(\tau, \tau') = A(\tau, \tau')B(\tau', \tau)$	$D^<(t, t') = A^<(t, t')B^>(t', t)$
	$D^r(t, t') = A^<(t, t')B^a(t', t) + A^r(t, t')B^<(t', t)$

Table 1.1: Examples of analytic continuation.

$$= \int_{-\infty}^{\infty} \mathrm{d}t [A^r(t_1, t)B^<(t, t_{1'}) + A^<(t_1, t)B^a(t, t_{1'})]. \tag{1.116}$$

More examples are given in Tab. 1.1. Applying Langreth theorem to Dyson's equation with the non-equilibrium term absorbed in the free Green's function, we have

$$G^< = G_0^< + G_0^r \Sigma^r G^< + G_0^r \Sigma^< G^a + G_0^< \Sigma^a G^a. \tag{1.117}$$

Infinite iterations lead to

$$G^< = (1 + G^r \Sigma^r) G_0^< (1 + \Sigma^a G^a) + G^r \Sigma^< G^a. \tag{1.118}$$

After Fourier transforming time into frequency, Eqn. 1.118 becomes

$$G^< = G^r \Sigma^< G^a. \tag{1.119}$$

By writing so, we have used $(1 + G^r \Sigma^r) G_0^< = 0$ in the limit $\eta \to 0^+$ with

$$G_0^r(\omega) = [\omega - \epsilon_{\boldsymbol{k}} + i\eta]^{-1},$$

$$G^r(\omega) = [G_0^r(\omega)^{-1} - \Sigma^r(\omega)]^{-1}, \tag{1.120}$$
$$G_0^<(\omega) = 2\pi i f(\epsilon_{\boldsymbol{k}})\delta(\epsilon_{\boldsymbol{k}} - \omega).$$

1.4.2 Landauer Formula

The Landauer formula expresses current as an integral of transmission over energy. It deals with non-interacting electrons and treats their transport as wave scattering. Beyond mean field, a general formula for electric current through an interacting region was derived by Wingreen et al. in 1992. Wingreen's formula falls back to the Landauer formula in the non-interacting limit. In this section, we will present Wingreen and Landauer's results.

Consider a tunnel junction consisting of left lead, interacting center region, and right lead as illustrated in Fig. 1.9. When left and right chemical potentials, μ_L and μ_R,

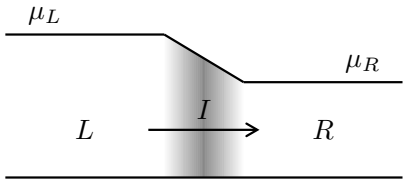

Figure 1.9: A tunnel junction with interacting scattering region.

are different, electric current I flows through the junction. The model Hamiltonian for the system in Fig. 1.9 is

$$\hat{H} = \sum_{\boldsymbol{k},\alpha} \epsilon_{\boldsymbol{k}\alpha} \hat{c}^\dagger_{\boldsymbol{k}\alpha} \hat{c}_{\boldsymbol{k}\alpha} + \hat{H}_{int}(\hat{d}^\dagger_n, \hat{d}_n) + \sum_{\boldsymbol{k},\alpha,n} \left(v_{\boldsymbol{k}\alpha,n} \hat{c}^\dagger_{\boldsymbol{k}\alpha} \hat{d}_n + \text{h.c.} \right), \tag{1.121}$$

where $\alpha \in L(R)$ runs over the quantum numbers belonging to the left (right) lead; $\hat{H}_{int}$ describes the many-body interaction in the scattering region; the last term is the coupling between the left (right) lead and the center region. Assume the tunneling term is turned on gradually and the desired steady state will be established at certain time, then we have a time dependent process for which non-equilibrium

many-particle formalism can be applied. Let left-going electric current direction be positive. Then the electric current operator is

$$\begin{aligned}\hat{I} =& -e\frac{\mathrm{d}\hat{N}_L}{\mathrm{d}t}\\ =& -\frac{e}{i\hbar}\big[\hat{N}_L,\hat{H}\big]\\ =& -\frac{e}{i\hbar}\sum_{\substack{\boldsymbol{k},\alpha\in L\\ n}}\big[v_{\boldsymbol{k}\alpha,n}\hat{c}^\dagger_{\boldsymbol{k}\alpha}\hat{d}_n - v^*_{\boldsymbol{k}\alpha,n}\hat{d}^\dagger_n\hat{c}_{\boldsymbol{k}\alpha}\big],\end{aligned} \tag{1.122}$$

where $e>0$ is the unit charge and $\hat{N}_L=\sum_{\boldsymbol{k},\alpha\in L}\hat{c}^\dagger_{\boldsymbol{k}\alpha}\hat{c}_{\boldsymbol{k}\alpha}$ is the number operator of the left lead. Apply the thermal average of Eqn. 1.97, we have

$$\begin{aligned}I =&\langle\hat{I}\rangle\\ =&\frac{ie}{\hbar}\sum_{\substack{\boldsymbol{k},\alpha\in L\\ n}}\big[v_{\boldsymbol{k}\alpha,n}\big\langle\hat{c}^\dagger_{\boldsymbol{k}\alpha}\hat{d}_n\big\rangle - \text{c.c.}\big]\\ =&\frac{2e}{\hbar}\,\mathrm{Re}\Big[\sum_{\substack{\boldsymbol{k},\alpha\in L\\ n}}v_{\boldsymbol{k}\alpha,n}G^<_{n,\boldsymbol{k}\alpha}(t,t)\Big],\end{aligned} \tag{1.123}$$

where the lesser Green's function $G^<_{n,\boldsymbol{k}\alpha}$ is defined by

$$G^<_{n,\boldsymbol{k}\alpha}(t,t')\equiv i\big\langle\hat{c}^\dagger_{\boldsymbol{k}\alpha}(t')\hat{d}_n(t)\big\rangle. \tag{1.124}$$

In order to simplify Eqn. 1.124, consider contour-ordered Green's functions for which we have

$$G_{n,\boldsymbol{k}\alpha}(\tau,\tau')=\sum_m\int\mathrm{d}\tau_1 G_{n,m}(\tau,\tau_1)v^*_{\boldsymbol{k}\alpha,m}g_{\boldsymbol{k}\alpha}(\tau_1,\tau'), \tag{1.125}$$

where $G_{n,m}$ and $g_{\boldsymbol{k},\alpha\in L(R)}$ are the Green's functions for the central region and the

lead $L(R)$ respectively. Its analytic continuation leads to

$$\begin{aligned} G^<_{n,\boldsymbol{k}\alpha}(t-t') = \sum_m \int \mathrm{d}t_1 V^*_{\boldsymbol{k}\alpha,m}[G^r_{n,m}(t-t_1)g^<_{\boldsymbol{k}\alpha}(t_1-t')]+ \\ G^<_{n,m}(t-t_1)g^a_{\boldsymbol{k}\alpha}(t_1-t'). \end{aligned} \tag{1.126}$$

After Fourier transform from time to energy, the lesser Green's function reads

$$G^<_{n,\boldsymbol{k}\alpha}(\epsilon) = \sum_m V^*_{\boldsymbol{k}\alpha,m}[G^r_{n,m}(\epsilon)g^<_{\boldsymbol{k}\alpha}(\epsilon) + G^<_{n,m}(\epsilon)g^a_{\boldsymbol{k}\alpha}(\epsilon)]. \tag{1.127}$$

Thus the electric current in Eqn. 1.123 becomes

$$I_L = \frac{2e}{\hbar}\int \frac{\mathrm{d}\epsilon}{2\pi}\,\mathrm{Re}\Big\{\sum_{\substack{\boldsymbol{k},\alpha\in L\\ n,m}} V_{\boldsymbol{k}\alpha,n}V^*_{\boldsymbol{k}\alpha,m}\big[G^r_{n,m}g^<_{\boldsymbol{k}\alpha} + G^<_{n,m}g^a_{\boldsymbol{k}\alpha}\big]\Big\}. \tag{1.128}$$

Define a level-width function

$$\big[\Gamma^L(\epsilon_{\boldsymbol{k}})\big]_{m,n} = 2\pi\sum_{\alpha\in L}\rho_\alpha(\epsilon_{\boldsymbol{k}})v_{\alpha,n}(\epsilon_{\boldsymbol{k}})v^*_{\alpha,m}(\epsilon_{\boldsymbol{k}}), \tag{1.129}$$

where $\rho_\alpha(\epsilon_{\boldsymbol{k}})$ is the density of states in channel α. Eqn. 1.128 then becomes

$$I_L = \frac{ie}{\hbar}\int \frac{\mathrm{d}\epsilon}{2\pi}\,\mathrm{Tr}\left(\boldsymbol{\Gamma}^L(\epsilon)\Big\{\boldsymbol{G}^<(\epsilon) + f_L(\epsilon)\big[\boldsymbol{G}^r(\epsilon)-\boldsymbol{G}^a(\epsilon)\big]\Big\}\right), \tag{1.130}$$

where $f_L(\epsilon)$ is the distribution function in the left lead. Starting from $I = e\langle\dot{\hat{N}}_R\rangle$, one ends up with

$$I_R = -\frac{ie}{\hbar}\int \frac{\mathrm{d}\epsilon}{2\pi}\,\mathrm{Tr}\left(\boldsymbol{\Gamma}^R(\epsilon)\Big\{\boldsymbol{G}^<(\epsilon) + f_R(\epsilon)\big[\boldsymbol{G}^r(\epsilon)-\boldsymbol{G}^a(\epsilon)\big]\Big\}\right). \tag{1.131}$$

Combine Eqn. 1.130 and 1.131, we have the general expression for the electric current

$$\begin{aligned} I =& (I_L + I_R)/2 \\ =& \frac{ie}{2\hbar} \int \frac{\mathrm{d}\epsilon}{2\pi} \mathrm{Tr} \Big\{ \big[\mathbf{\Gamma}^L(\epsilon) - \mathbf{\Gamma}^R(\epsilon)\big] \boldsymbol{G}^<(\epsilon) + \\ & \big[f_L(\epsilon)\mathbf{\Gamma}^L(\epsilon) - f_R(\epsilon)\mathbf{\Gamma}^R(\epsilon)\big] \big[\boldsymbol{G}^r(\epsilon) - \boldsymbol{G}^a(\epsilon)\big] \Big\}. \end{aligned} \tag{1.132}$$

For the non-interacting case, one has Dyson's equations for the Green's functions in the center region which enables us to rewrite Eqn. 1.132 as[34]

$$I = \frac{e}{\hbar} \int \frac{\mathrm{d}\epsilon}{2\pi} [f_L(\epsilon) - f_R(\epsilon)] \, \mathrm{Tr}\{\boldsymbol{G}^a \mathbf{\Gamma}^R \boldsymbol{G}^r \mathbf{\Gamma}^L\}. \tag{1.133}$$

In terms of the transmission coefficient from left to right

$$t_{\alpha\alpha'} \equiv 2\pi \sum_{n,m} \rho_\alpha^{1/2} \rho_{\alpha'}^{1/2} v^*_{\alpha,n} G^r_{n,m} v_{\alpha',m} \tag{1.134}$$

with $\alpha \in R$ and $\alpha' \in L$, the electric current in Eqn. 1.133 becomes

$$I = \frac{e}{\hbar} \int \frac{\mathrm{d}\epsilon}{2\pi} [f_L(\epsilon) - f_R(\epsilon)] \, \mathrm{Tr}\{\boldsymbol{t}\boldsymbol{t}^\dagger(\epsilon)\}, \tag{1.135}$$

which is the usual Landauer formula.

1.5 Ground State Density Functional Theory

In this subsection, we review the ground-state density functional theory (GS-DFT) which is an alternative to MPF for solving ground-state properties. GS-DFT is based on two Hohenberg-Kohn (HK) theorems.[7] The first HK theorem states that any observable is a functional of the ground-state electron density ρ, e.g. the ground-state energy $E_0 = E_0[\rho]$. The second HK theorem states that $E_0[\rho]$ is stationary about the ground-state electron density. To solve $\delta E_0 = 0$, Kohn and Sham (KS) developed

a mean field scheme by introducing a non-interacting reference system.[64] The exact $E_0[\rho]$ is still unknown but can be well approximated.

1.5.1 HK Theorems

The proof of HK theorem one is based on the minimum-energy principle. Let $\rho(\boldsymbol{r})$ be the ground-state electron density for some non-degenerate N-electron system governed by the Hamiltonian

$$\hat{H} = \hat{T} + \int \mathrm{d}\boldsymbol{r}\rho(\boldsymbol{r})v_{\text{ext}}(\boldsymbol{r}) + \hat{V}_{ee}. \tag{1.136}$$

Assume $\rho(\boldsymbol{r})$ is also the ground-state electron density for another N-electron Hamiltonian

$$\hat{H}' = \hat{T} + \int \mathrm{d}\boldsymbol{r}\rho(\boldsymbol{r})v'_{\text{ext}}(\boldsymbol{r}) + \hat{V}_{ee}, \tag{1.137}$$

where $v'_{\text{ext}}(\boldsymbol{r})$ is locally different from $v_{\text{ext}}(\boldsymbol{r})$. Let $|\Psi\rangle$ and $|\Psi'\rangle$ be the ground states for $\hat{H}$ and $\hat{H}'$ respectively. Since $|\Psi\rangle \not\equiv |\Psi'\rangle$,

$$\begin{aligned} E_0 < \langle\Psi'|\hat{H}|\Psi'\rangle &= \langle\Psi'|\hat{H}'|\Psi'\rangle + \langle\Psi'|\hat{H} - \hat{H}'|\Psi'\rangle \\ &= E'_0 + \int \mathrm{d}\boldsymbol{r}\rho(\boldsymbol{r})\big[v_{\text{ext}}(\boldsymbol{r}) - v'_{\text{ext}}(\boldsymbol{r})\big]. \end{aligned} \tag{1.138}$$

Similarly,

$$\begin{aligned} E'_0 < \langle\Psi|\hat{H}'|\Psi\rangle &= \langle\Psi|\hat{H}|\Psi\rangle - \langle\Psi|\hat{H} - \hat{H}'|\Psi\rangle \\ &= E_0 - \int \mathrm{d}\boldsymbol{r}\rho(\boldsymbol{r})\big[v_{\text{ext}}(\boldsymbol{r}) - v'_{\text{ext}}(\boldsymbol{r})\big]. \end{aligned} \tag{1.139}$$

Combine Eqn. 1.138 and 1.139, we get

$$E_0 + E'_0 < E'_0 + E_0, \tag{1.140}$$

which cannot be true. Thus $v_{\text{ext}}(\boldsymbol{r})$ and $v'_{\text{ext}}(\boldsymbol{r})$ cannot be locally different. When they are different by only a global constant, $\hat{H}$ and $\hat{H}'$ have common ground state thus the same ground-state electron density. Therefore, the ground-state electron density $\rho(\boldsymbol{r})$ determines the external potential $v_{\text{ext}}(\boldsymbol{r})$ up to a global additive constant. Consequently, the ground state can be determined by $\rho(\boldsymbol{r})$ and the expectation value of any observable $\hat{O}$ is a functional of $\rho(\boldsymbol{r})$, such as the kinetic energy $T[\rho(\boldsymbol{r})]$ and the potential energy $V_{ee}[\rho(\boldsymbol{r})]$. In $V_{ee}[\rho(\boldsymbol{r})]$, the classical component is the Hartree energy $E_H[\rho(\boldsymbol{r})] = \int \mathrm{d}\boldsymbol{r}\mathrm{d}\boldsymbol{r}'\rho(\boldsymbol{r})\rho(\boldsymbol{r}')/|\boldsymbol{r}-\boldsymbol{r}'|$.

Let $E_0[\rho(\boldsymbol{r})]$ be the ground-state energy functional for some N-electron system with a certain external potential. The second HK theorem reads: For a trial density $\rho'(\boldsymbol{r})$, such that $\rho'(\boldsymbol{r}) \geq 0$ and $\int \mathrm{d}\boldsymbol{r}\rho'(\boldsymbol{r}) = N$,

$$E_0 \leq E_0[\rho'(\boldsymbol{r})] \tag{1.141}$$

where E_0 is the ground-state energy.

1.5.2 KS Scheme

In order to obtain the ground state properties from $\delta E_0[\rho] = 0$, Kohn and Sham introduced a non-interacting reference system governed by the Hamiltonian

$$\hat{H}_s = -\frac{1}{2}\sum_i^N \boldsymbol{\nabla}_i^2 + \sum_i^N v_s(\boldsymbol{r}_i). \tag{1.142}$$

The reference system has the following ground state

$$\Psi_s = \frac{1}{\sqrt{N!}}\det[\psi_1\psi_2\cdots\psi_N]$$

$$\equiv \frac{1}{\sqrt{N!}} \begin{vmatrix} \psi_1(\boldsymbol{r}_1, s_1) & \psi_1(\boldsymbol{r}_2, s_2) & \cdots & \psi_1(\boldsymbol{r}_N, s_N) \\ \psi_2(\boldsymbol{r}_1, s_1) & \psi_2(\boldsymbol{r}_2, s_2) & \cdots & \psi_2(\boldsymbol{r}_N, s_N) \\ \vdots & \vdots & \ddots & \vdots \\ \psi_N(\boldsymbol{r}_1, s_1) & \psi_N(\boldsymbol{r}_2, s_2) & \cdots & \psi_N(\boldsymbol{r}_N, s_N) \end{vmatrix} \tag{1.143}$$

where the ψ_i are the N lowest eigenstates of the one-electron Hamiltonian

$$\hat{h}_s = -\frac{1}{2}\boldsymbol{\nabla}^2 + v_s(\boldsymbol{r}). \tag{1.144}$$

Ψ_s is assumed to bear the same electron density as the real one in the interacting system, namely

$$\rho_{\text{real}} = \sum_i^N \sum_s |\psi_i(\boldsymbol{r}, s)|^2. \tag{1.145}$$

In the reference system, the kinetic energy is

$$T_s = \langle \Psi_s | -\frac{1}{2}\sum_i^N \boldsymbol{\nabla}_i^2 | \Psi_s \rangle = \sum_i^N \langle \psi_i | -\frac{1}{2}\boldsymbol{\nabla}_i^2 | \psi_i \rangle. \tag{1.146}$$

Define the exchange correlation energy functional

$$E_{xc}[\rho] \equiv T[\rho] - T_s[\rho] + V_{ee}[\rho] - V_H[\rho]. \tag{1.147}$$

Then $E_0[\rho]$ can be rewritten as

$$E_0[\rho] = T_s[\rho] + \int \mathrm{d}\boldsymbol{r} \rho v_{\text{ext}} + V_H[\rho] + E_{xc}[\rho]. \tag{1.148}$$

The minimum of $E_0[\rho]$ can be searched by varying the single particle states ψ_i with constraints

$$\int \mathrm{d}\boldsymbol{x} \psi_i^*(\boldsymbol{x}) \psi_j(\boldsymbol{x}) = \delta_{ij}, \tag{1.149}$$

which guarantees $\int \mathrm{d}\boldsymbol{r}\rho = N$. Following the method of Lagrange multipliers, define the functional Ω of the N orbitals

$$\Omega[\{\psi_i\}] = E_0[\rho] - \sum_i^N \sum_j^N \varepsilon_{ij} \int \mathrm{d}\boldsymbol{x}\psi_i^*(\boldsymbol{x})\psi_j(\boldsymbol{x}). \tag{1.150}$$

Then $\delta\Omega = 0$ leads to the KS equations

$$\hat{h}_{\text{eff}}\psi_i = [-\frac{1}{2}\boldsymbol{\nabla}^2 + v_{\text{eff}}]\psi_i = \sum_j^N \varepsilon_{ij}\psi_j, \tag{1.151}$$

where

$$v_{\text{eff}}(\boldsymbol{r}) = v_{\text{ext}}(\boldsymbol{r}) + \int \mathrm{d}\boldsymbol{r}' \frac{\rho(\boldsymbol{r}')}{|\boldsymbol{r} - \boldsymbol{r}'|} + v_{xc}(\boldsymbol{r}), \tag{1.152}$$

with $v_{xc}(\boldsymbol{r}) = \delta E_{xc}[\rho]/\delta\rho(\boldsymbol{r})$. Since $\hat{h}_{\text{eff}}$ is Hermitian, (ε_{ij}) is a Hermitian matrix and can be diagonalized by a unitary transformation. After the unitary transformation, the KS equations take their canonical form

$$[-\frac{1}{2}\boldsymbol{\nabla}^2 + v_{\text{eff}}]\psi_i = \epsilon_i\psi_i. \tag{1.153}$$

Once the Eqn. 1.153 is solved, the ground-state energy can be evaluated via Eqn. 1.148 or from the formula

$$E_0 = \sum_i^N \epsilon_i - \frac{1}{2}\int \mathrm{d}\boldsymbol{r}\mathrm{d}\boldsymbol{r}' \frac{\rho(\boldsymbol{r})\rho(\boldsymbol{r}')}{|\boldsymbol{r} - \boldsymbol{r}'|} + E_{xc}[\rho] - \int \mathrm{d}\boldsymbol{r}\rho(\boldsymbol{r})v_{xc}(\boldsymbol{r}). \tag{1.154}$$

1.5.3 Approximating E_{xc}

Since the exact $E_0[\rho]$ is still unknown, $E_{xc}[\rho]$ needs to be approximated in practice. Under local density approximation (LDA),

$$E_{xc}^{\text{LDA}}[\rho] = \int \mathrm{d}\boldsymbol{r}\rho(\boldsymbol{r})\varepsilon_{xc}(\rho), \tag{1.155}$$

where $\varepsilon_{xc}(\rho)$ is the exchange and correlation energy per particle of a uniform electron gas of density ρ. $\varepsilon_{xc}(\rho)$ can be divided into exchange and correlation parts

$$\varepsilon_{xc}(\rho) = \varepsilon_x(\rho) + \varepsilon_c(\rho). \tag{1.156}$$

The exchange part is already known from the TFD model and takes the form [65]

$$\varepsilon_x(\rho) = -C_x\rho^{1/3} \tag{1.157}$$

with $C_x = (3/4)(3/\pi)^{1/3}$. Accurate values of $\varepsilon_c(\rho)$ have been obtained by the quantum Monte Carlo calculations of Ceperley and Alder. [66] These values have been interpolated to provide an analytic form for $\varepsilon_c(\rho)$. [67]

In the presence of a magnetic field $\boldsymbol{B}(\boldsymbol{r})$, spin up electron density ρ^α and spin down electron density ρ^β play the role of basic variables. [68,69] In this case, the exchange correlation energy can be approximated by local spin density approximation (LSDA). Define the spin polarization parameter ζ by

$$\zeta = \frac{\rho^\alpha - \rho^\beta}{\rho} = \frac{\rho^\alpha - \rho^\beta}{\rho^\alpha + \rho^\beta}. \tag{1.158}$$

The exchange energy under LSDA then takes the form

$$E_x^{\text{LSDA}}[\rho^\alpha, \rho^\beta] = \int \mathrm{d}\boldsymbol{r}\rho\varepsilon_x(\rho, \zeta), \tag{1.159}$$

where $\varepsilon_x(\rho, \zeta) = \varepsilon_x^0(\rho) + [\varepsilon_x^1(\rho) - \varepsilon_x^0(\rho)]f(\zeta)$ with $\varepsilon_x^0(\rho) = \varepsilon_x(\rho, 0) = C_x\rho^{1/3}$, $\varepsilon_x^1(\rho) = \varepsilon_x(\rho, 1) = 2^{1/3}C_x\rho^{1/3}$, and $f(\zeta) = \frac{1}{2}(2^{1/3} - 1)^{-1}[(1 + \zeta)^{4/3} + (1 - \zeta)^{4/3} - 2]$. The correlation part formally writes

$$E_c^{\text{LSDA}}[\rho^\alpha, \rho^\beta] = \int \mathrm{d}\boldsymbol{r}\rho\varepsilon_c(\rho, \zeta). \tag{1.160}$$

It can be evaluated numerically within random phase approximation.[70,71]

Beyond LSDA, non-local correction can be included by generalized gradient approximation (GGA) which takes the general form

$$E_{xc}[\rho] = \int \mathrm{d}\boldsymbol{r}\epsilon_x(\rho)\xi g_{xc}(\rho,\xi), \tag{1.161}$$

where

$$\xi = \frac{(\boldsymbol{\nabla}\rho)^2}{4(3\pi^2\rho)^{2/3}\rho^2}. \tag{1.162}$$

The $E_{xc}[\rho]$ proposed by Perdew, Burke, and Ernzerhof is widely applied.[72]

GS-DFT has become a powerful tool for electronic structure analysis for both molecules and solids. In principle, it also applies for a molecular junction under zero bias voltage. However GS-DFT doesn't apply for the molecular junction under finite bias. In this case, we will show in next chapter that a steady state density functional theory (SS-DFT) can be developed and applied. As a remark, time dependent density functional theory (TD-DFT) applies for time dependent processes and uses the time dependent electron density as basic variable.[73] In order to approach the steady state with TD-DFT, one needs to solve the time evolution of system state from the beginning to long time limit which is not necessary when only the steady state is concerned.[74] On the other hand, without solving the transient state, one can obtain the steady state self-consistently under adiabatic local density approximation (ALDA), which however loses non-equilibrium effects.[75]

It takes two of us to discover truth: one to utter it and one to understand it.

Kahlil Gibran

2

Steady-State Density Functional Theory

In this chapter, we will first present the basis of the steady-state density functional theory (SS-DFT) for open quantum systems. Second, we will introduce a dual mean field (DMF) approach to solve the electronic structure of an open quantum system in steady state. Third, we will derive the exchange energy functional explicitly for a non-equilibrium uniform non-interacting electron gas. Finally, we will discuss the implementation of SS-DFT in the SIESTA package.

2.1 Basis of the Theory

In this section, we will present two steady-state density functional theorems for open quantum systems in steady state. They are analogous to the Hohenberg-Kohn theorems for a quantum system in ground state.[7] The steady-state density functional theorems are proved based on Hershfield's non-equilibrium statistics with the aid of an effective ground state. The correspondence between the effective ground state and the desired steady state will also be investigated.

2.1.1 Density Functional Theorems

In this subsection, we prove the steady-state density functional theorems.[76] Consider an open quantum system consisting of left reservoir, center region, and right reservoir as shown in Fig. 2.1. The left (right) reservoir is connected to the cathode (anode) of a battery. In this case, the left chemical potential μ_L is greater than the right chemical potential μ_R. The difference between the two chemical potentials determines the bias voltage by $eV_b = \mu_L - \mu_R$ where e is the unit charge. The model Hamiltonian for

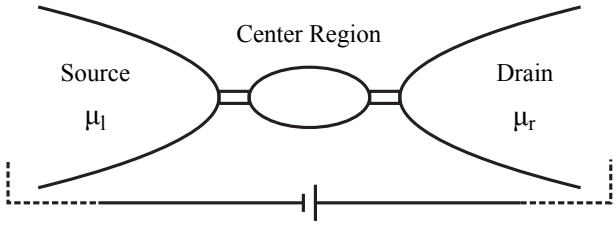

Figure 2.1: Model of an open quantum system under finite bias. The system consists of left reservoir, center region, and right reservoir. The two reservoirs are connected to a battery. The chemical potential for the left (right) reservoir is μ_L (μ_R).

the system illustrated in Fig. 2.1 is $\hat{H} = \hat{H}_{\text{lead}} + \hat{H}_{\text{C}} + \hat{H}_{\text{T}}$ with

$$\begin{aligned} \hat{H}_{\text{lead}} &= \sum_{\boldsymbol{k}\alpha} \epsilon_{\boldsymbol{k}\alpha} \hat{a}^{\dagger}_{\boldsymbol{k}\alpha} \hat{a}_{\boldsymbol{k}\alpha}, \\ \hat{H}_{\text{C}} &= \hat{H}_{\text{int}}(\{\hat{c}^{\dagger}_i\}, \{\hat{c}_i\}), \end{aligned} \tag{2.1}$$

$$\hat{H}_{\mathrm{T}} = \sum_{\boldsymbol{k}\alpha,i} (V_{\boldsymbol{k}\alpha,i} \hat{a}^{\dagger}_{\boldsymbol{k}\alpha} \hat{c}_i + \mathrm{H.c.}).$$

In Eqn. 2.1, $\alpha \in L(R)$ runs over the quantum indexes belonging to the left (right) reservoir; $\hat{a}^{\dagger}_{\boldsymbol{k}\alpha}$ with $\alpha \in L(R)$ creates a Bloch state in the left (right) reservoir; All $\hat{c}^{\dagger}_i$ generate a complete basis for the center region; H_T is the coupling term between the reservoirs and the center region; H.c. is the Hermitian conjugate of the first term in $\hat{H}_{\mathrm{T}}$. Note that many-body interaction is only included in the center region.

For the open system in steady state shown in Fig. 2.1, Hershfield showed that the expectation value of any observable $\hat{A}$ can be evaluated by a non-equilibrium density matrix, namely[54]

$$\langle \hat{A} \rangle = \frac{Tr\left[e^{-\beta(\hat{H}-\hat{Y})}\hat{A}\right]}{Tr\left[e^{-\beta(\hat{H}-\hat{Y})}\right]}, \tag{2.2}$$

where

$$\hat{Y} = \mu_L \sum_{\boldsymbol{k},\alpha\in L} \hat{\psi}^{\dagger}_{\boldsymbol{k}\alpha}\hat{\psi}_{\boldsymbol{k}\alpha} + \mu_R \sum_{\boldsymbol{k},\alpha\in R} \hat{\psi}^{\dagger}_{\boldsymbol{k}\alpha}\hat{\psi}_{\boldsymbol{k}\alpha} \tag{2.3}$$

accounts for the non-equilibrium distribution.* In Eqn. 2.3, $\hat{\psi}^{\dagger}_{\boldsymbol{k}\alpha}$ with $\alpha \in L(R)$ creates a scattering state incident from lead L (R); and $k_z > 0$ (< 0) when $\alpha \in L(R)$. Importantly, Hershfield's results provide the basis for the steady-state density functional theorems which will be proved in the following.

First, Hershfield's results imply that the steady state corresponds to an effective ground state. To see the correspondence, let's define the particle number operators

$$\begin{aligned} \hat{N}_L &= \sum_{\boldsymbol{k},\alpha\in L} \hat{\psi}^{\dagger}_{\boldsymbol{k}\alpha}\hat{\psi}_{\boldsymbol{k}\alpha}, \\ \hat{N}_R &= \sum_{\boldsymbol{k},\alpha\in R} \hat{\psi}^{\dagger}_{\boldsymbol{k}\alpha}\hat{\psi}_{\boldsymbol{k}\alpha}, \end{aligned} \tag{2.4}$$

*Assume there are no bound states in the center region.

and

$$\begin{aligned}\hat{N} =& \hat{N}_L + \hat{N}_R, \\ \hat{N}_n =& \hat{N}_L - \hat{N}_R.\end{aligned} \tag{2.5}$$

$\hat{N}_L$, $\hat{N}_R$, and $\hat{N}_n$ count the number of electrons incident from left, electrons incident from right, and non-equilibrium electrons respectively while $\hat{N}$ is the total number operator. With the particle number operators $\hat{N}$ and $\hat{N}_n$, the non-equilibrium density matrix in Eqn. 2.2 can be rewritten as

$$\hat{\rho} = e^{-\beta(\hat{H}-\hat{Y})} = e^{-\beta\left(\tilde{\hat{H}}-\tilde{\mu}\hat{N}\right)}, \tag{2.6}$$

where

$$\tilde{\hat{H}} = \hat{H} - \frac{eV_b}{2}\hat{N}_n, \tag{2.7}$$

$$\tilde{\mu} = \frac{\mu_L + \mu_R}{2}. \tag{2.8}$$

Eqn. 2.2 and 2.6 together show that a system in non-equilibrium steady state corresponds to a system in effective equilibrium.

Second, let's define total electron and current-carrying electron density operators, $\hat{\rho}_t(\boldsymbol{r})$ and $\hat{\rho}_n(\boldsymbol{r})$. Note that the real space representation of $\hat{N}_L$ in Eqn. 2.4 writes

$$\begin{aligned}\hat{N}_L &= \sum_{\boldsymbol{k},\alpha\in L} \hat{\psi}^\dagger_{\boldsymbol{k}\alpha}\hat{\psi}_{\boldsymbol{k}\alpha} \\ &= \sum_{\boldsymbol{k},\alpha\in L} \int \mathrm{d}\boldsymbol{r}\mathrm{d}\boldsymbol{r}' \left\langle \boldsymbol{r}\right| \left.\boldsymbol{k}\alpha\right\rangle \left\langle \boldsymbol{k}\alpha\right| \left.\boldsymbol{r}'\right\rangle \hat{\psi}^\dagger_L(\boldsymbol{r})\hat{\psi}_L(\boldsymbol{r}') \\ &= \int \mathrm{d}\boldsymbol{r}\mathrm{d}\boldsymbol{r}'\delta(\boldsymbol{r}-\boldsymbol{r}')\hat{\psi}^\dagger_L(\boldsymbol{r})\hat{\psi}_L(\boldsymbol{r}') \\ &= \int \mathrm{d}\boldsymbol{r}\hat{\psi}^\dagger_L(\boldsymbol{r})\hat{\psi}_L(\boldsymbol{r}) \\ &\equiv \int \mathrm{d}\boldsymbol{r}\hat{\rho}_L(\boldsymbol{r}).\end{aligned} \tag{2.9}$$

Similarly

$$\hat{N}_R = \int \mathrm{d}\boldsymbol{r}\hat{\psi}_R^\dagger(\boldsymbol{r})\hat{\psi}_R(\boldsymbol{r}) \equiv \int \mathrm{d}\boldsymbol{r}\hat{\rho}_R(\boldsymbol{r}). \tag{2.10}$$

Therefore, the real space representation of Eqn. 2.5 writes

$$\begin{aligned} \hat{N} &= \int \mathrm{d}\boldsymbol{r}\hat{\rho}_t(\boldsymbol{r}), \\ \hat{N}_n &= \int \mathrm{d}\boldsymbol{r}\hat{\rho}_n(\boldsymbol{r}), \end{aligned} \tag{2.11}$$

with

$$\begin{aligned} \hat{\rho}_t(\boldsymbol{r}) \equiv& \hat{\rho}_L(\boldsymbol{r}) + \hat{\rho}_R(\boldsymbol{r}), \\ \hat{\rho}_n(\boldsymbol{r}) \equiv& \hat{\rho}_L(\boldsymbol{r}) - \hat{\rho}_R(\boldsymbol{r}). \end{aligned} \tag{2.12}$$

Third, we prove the steady-state density functional theorem one based on the minimum property of the effective ground state energy. Assume the effective Hamiltonians

$$\begin{aligned} \tilde{\hat{H}} =& \hat{T} + \int \mathrm{d}\boldsymbol{r}\rho_t\hat{v}_{ext} + \hat{V}_{ee} - \frac{eV_b}{2}\int \mathrm{d}\boldsymbol{r}\hat{\rho}_n, \\ \tilde{\hat{H}}' =& \hat{T} + \int \mathrm{d}\boldsymbol{r}\rho_t\hat{v}'_{ext} + \hat{V}_{ee} - \frac{eV'_b}{2}\int \mathrm{d}\boldsymbol{r}\hat{\rho}_n, \end{aligned} \tag{2.13}$$

bear the same ρ_t and N_n with $\hat{v}'_{ext}(\boldsymbol{x})$ being locally different from $\hat{v}_{ext}(\boldsymbol{x})$ or V'_b being different from V_b. The effective ground state energy $\tilde{E}_0$ can be evaluated as follows

$$\begin{aligned} \tilde{E}_0 =& \frac{Tr\left[\hat{\rho}\tilde{\hat{H}}\right]}{Tr\left[\hat{\rho}\right]} \overset{T\to 0}{=} \langle\tilde{\psi}_0|\tilde{\hat{H}}|\tilde{\psi}_0\rangle \\ =& \langle\tilde{\psi}_0|\tilde{\hat{H}} - \tilde{\hat{H}}' + \tilde{\hat{H}}'|\tilde{\psi}_0\rangle \\ >& \tilde{E}'_0 + \langle\tilde{\psi}_0|\tilde{\hat{H}} - \tilde{\hat{H}}'|\tilde{\psi}_0\rangle \\ >& \tilde{E}'_0 + \int \mathrm{d}\boldsymbol{r}\rho_t(V_{ext} - V'_{ext}) - \frac{e(V_b - V'_b)}{2}\int \mathrm{d}\boldsymbol{r}\rho_n. \end{aligned} \tag{2.14}$$

Similarly,

$$\tilde{E}'_0 > \tilde{E}_0 - \int \mathrm{d}\boldsymbol{r}\rho_t(V_{ext} - V'_{ext}) + \frac{e(V_b - V'_b)}{2}\int \mathrm{d}\boldsymbol{r}\rho_n. \tag{2.15}$$

Combining Eq. 2.14 and 2.15, we get

$$\tilde{E}_0 + \tilde{E}_0' > \tilde{E}_0' + \tilde{E}_0, \tag{2.16}$$

which cannot be true. On the one hand, ρ_t and ρ_n remain the same when $\hat{v}_{ext}$ is arbitrarily shifted globally. Furthermore, ρ_e and ρ_n are equivalent to ρ_t and ρ_n due to $\rho_t \equiv \rho_e + \rho_n$. Thus ρ_e and ρ_n determine $\hat{v}_{ext}$ and V_b within an additive global constant to $\hat{v}_{ext}$. This completes the proof for the *steady-state density functional theorem one* which indicates that the effective ground state energy is a functional of ρ_e and ρ_n, namely

$$\tilde{E}_0 = \tilde{E}_0[\rho_e, \rho_n]. \tag{2.17}$$

Fourth, the minimum property of the effective ground state energy can be rephrased as the *steady-state density functional theorem two*: For trial densities $\rho_e'(\boldsymbol{r})$, $\rho_n'(\boldsymbol{r})$, such that $\rho_e'(\boldsymbol{r}) \geq 0$, $\rho_n'(\boldsymbol{r}) \geq 0$, and $\int \mathrm{d}\boldsymbol{r}[\rho_e'(\boldsymbol{r}) + \rho_n'(\boldsymbol{r})] = N$,

$$\tilde{E}_0 \leq \tilde{E}_0[\rho_e', \rho_n'] \tag{2.18}$$

where $\tilde{E}_0[\rho_e', \rho_n']$ is the energy functional in Eqn. 2.17. The theorem two forms a starting point for searching the desired steady state.

As a final remark, according to Eqn. 2.12, electron densities ρ_L and ρ_R are also equivalent to ρ_t and ρ_n. Therefore, the two steady-state density functional theorems can be stated in terms of ρ_L and ρ_R. This is useful for developing mean field approaches.

2.1.2 From Steady State to Effective Ground State

In this subsection, we will investigate the correspondence between the steady state and the effective ground state by evaluating the total number of particles $\langle \hat{N} \rangle$ and the effective energy $\langle \tilde{\hat{H}} \rangle$.

For simplicity, we ignore the many-body interaction and write the Hamiltonian as

$$\hat{H} = \sum_i \epsilon_i \hat{\psi}_i^\dagger \hat{\psi}_i, \tag{2.19}$$

and the effective Hamiltonian as

$$\tilde{\hat{H}} = \hat{H} - \frac{eV_b}{2}\hat{N}_n = \sum_i \tilde{\epsilon}_i \hat{\psi}_i^\dagger \hat{\psi}_i. \tag{2.20}$$

In Eqn. 2.19 and 2.20, the index i stands for $\boldsymbol{k}\alpha$; $\tilde{\epsilon}_i$ is defined to be

$$\tilde{\epsilon}_i = \epsilon_i - (-1)^{\xi_i}\, eV_b/2 \tag{2.21}$$

with $\xi_i = 0$ for $\alpha \in L$ and $\xi_i = 1$ for $\alpha \in R$. Eqn. 2.19 and 2.20 imply that a state of energy ϵ_i in the true system corresponds to a state of energy $\tilde{\epsilon}_i$ in the effective system.

Now let's turn to the evaluations of $\langle \hat{N} \rangle$ and $\langle \tilde{\hat{H}} \rangle$. First, the non-equilibrium density operator $\hat{\rho}$ in Hershfield's formalism writes

$$\hat{\rho} = \exp\big[-\beta(\hat{H} - \hat{Y})\big] = \exp\big[-\beta \sum_i (\tilde{\epsilon}_i - \tilde{\mu})\hat{n}_i\big], \tag{2.22}$$

where the effective chemical potential $\tilde{\mu}$ is given in Eqn. 2.8 and $\hat{n}_i$ is the particle number operator, i.e. $\hat{n}_i = \hat{\psi}_i^\dagger \hat{\psi}_i$. Thus the partition function is

$$\begin{aligned}
&\mathrm{Tr}[\hat{\rho}] \\
&= \mathrm{Tr}\left\{ \exp\big[-\beta \sum_i (\tilde{\epsilon}_i - \tilde{\mu})\, \hat{n}_i\big] \right\} \\
&\overset{2}{=} \mathrm{Tr}\left\{ \prod_i \exp\big[-\beta\, (\tilde{\epsilon}_i - \tilde{\mu})\, \hat{n}_i\big] \right\} \\
&= \sum_{\{\cdots n_i \cdots\}} \langle \cdots n_i \cdots | \prod_i \exp\left[-\beta\, (\tilde{\epsilon}_i - \tilde{\mu})\, \hat{n}_i\right] | \cdots n_i \cdots \rangle
\end{aligned} \tag{2.23}$$

$$
\begin{aligned}
&= \sum_{n_1=0}^{1} \sum_{n_2=0}^{1} \cdots \prod_i \exp\left[-\beta\left(\tilde{\epsilon}_i - \tilde{\mu}\right) n_i\right] \\
&= \prod_i \left(1 + \lambda_i\right),
\end{aligned}
$$

where $\lambda_i \equiv \exp\left[-\beta\left(\tilde{\epsilon}_i - \tilde{\mu}\right)\right]$. In step 2, the commutation relation $[\hat{n}_i, \hat{n}_j] = 0$ was applied. Second, the total number of particles is

$$
\begin{aligned}
&\langle \hat{N} \rangle = \mathrm{Tr}\left[\hat{\rho}\hat{N}\right] / \mathrm{Tr}\left[\hat{\rho}\right] \\
=&\frac{1}{\mathrm{Tr}\left[\hat{\rho}\right]} \sum_{\{\cdots n_i \cdots\}} \langle \cdots n_i \cdots | \hat{\rho} \sum_i \hat{n}_i | \cdots n_i \cdots \rangle \\
=&\frac{1}{\mathrm{Tr}\left[\hat{\rho}\right]} \sum_{n_1=0}^{1} \sum_{n_2=0}^{1} \cdots \prod_{i=1}^{\infty} \lambda_i^{n_i} \sum_{j=1}^{\infty} n_j \\
=&\frac{1}{\mathrm{Tr}\left[\hat{\rho}\right]} \sum_{n_2=0}^{1} \cdots \left[\lambda_1 \prod_{i=2}^{\infty} \lambda_i^{n_i} + (1+\lambda_1) \prod_{i=2}^{\infty} \lambda_i^{n_i} \sum_{j=2}^{\infty} n_j\right] \\
=&\frac{1}{\mathrm{Tr}\left[\hat{\rho}\right]} \left[\lambda_1 \prod_{i=2}^{\infty} (1+\lambda_i) + (1+\lambda_1) \sum_{n_2=0}^{1} \cdots \prod_{i=2}^{\infty} \lambda_i^{n_i} \sum_{j=2}^{\infty} n_j\right] \qquad (2.24) \\
=&\frac{1}{\mathrm{Tr}\left[\hat{\rho}\right]} \sum_{i=1}^{\infty} \prod_{j=1}^{\infty} \left(\bar{\delta}_{ij} + \lambda_j\right) \\
=&\sum_{i=1}^{\infty} \frac{\lambda_i}{1+\lambda_i} \\
=&\sum_{i=1}^{\infty} \frac{1}{1 + \exp\left[-\beta\left(\tilde{\epsilon}_i - \tilde{\mu}\right)\right]},
\end{aligned}
$$

where $\bar{\delta}_{ij} = 0$ if $i = j$ and $\bar{\delta}_{ij} = 1$ if $i \neq j$. Third, the effective energy is

$$
\begin{aligned}
&\langle \tilde{\hat{H}} \rangle = \mathrm{Tr}\left[\hat{\rho}\tilde{\hat{H}}\right] / \mathrm{Tr}\left[\hat{\rho}\right] \\
=&\frac{1}{\mathrm{Tr}\left[\hat{\rho}\right]} \mathrm{Tr}\left\{\hat{\rho} \sum_i \tilde{\epsilon}_i \hat{n}_i\right\} \\
=&\frac{1}{\mathrm{Tr}\left[\hat{\rho}\right]} \sum_{n_1=0}^{1} \sum_{n_2=0}^{1} \cdots \prod_{i=1}^{\infty} \lambda_i^{n_i} \sum_{j=1}^{\infty} \tilde{\epsilon}_j n_j
\end{aligned}
$$

$$
\begin{aligned}
=&\frac{1}{\mathrm{Tr}\left[\hat{\rho}\right]}\left[\lambda_1\tilde{\epsilon}_1\prod_{i=2}^{\infty}(1+\lambda_i)+(1+\lambda_1)\sum_{n_2=0}^{1}\cdots\prod_{i=2}^{\infty}\lambda_i^{n_i}\sum_{j=2}^{\infty}\tilde{\epsilon}_j n_j\right] \qquad (2.25)\\
=&\frac{1}{\mathrm{Tr}\left[\hat{\rho}\right]}\sum_{i=1}^{\infty}\tilde{\epsilon}_i\prod_{j=1}^{\infty}\left(\bar{\delta}_{ij}+\lambda_j\right)\\
=&\sum_{i=1}^{\infty}\frac{\lambda_i\tilde{\epsilon}_i}{1+\lambda_i}\\
=&\sum_{i=1}^{\infty}\frac{\tilde{\epsilon}_i}{1+\exp\left[-\beta\left(\tilde{\epsilon}_i-\tilde{\mu}\right)\right]}.
\end{aligned}
$$

Eqn. 2.24 and 2.25 imply that the effective system is in equilibrium.

In summary, single-particle states incident from left (right) are pulled down (lifted up) by $eV_b/2$ when a many-body steady state is mapped onto an effective ground state. As a result, the effective system has a common Fermi energy $\tilde{\mu} = (\mu_L + \mu_R)/2$, as illustrated in Fig. 2.2.

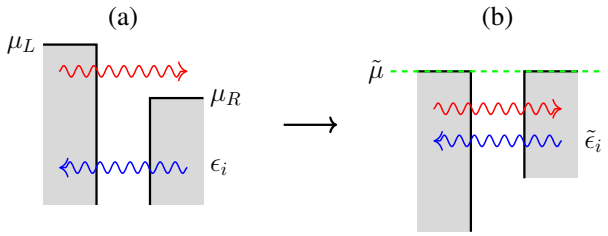

Figure 2.2: Correspondence between a non-equilibrium steady state (a) and an effective equilibrium ground state (b). The red (blue) wiggly arrow indicates an electron incident from left (right). The states incident from left (right) are pulled down (lifted up) by $eV_b/2$. The effective Fermi energy $\tilde{\mu} = (\mu_L + \mu_R)/2$.

2.2 Dual Mean Field Approach

In this section, we will present the *dual mean field* (DMF) approach for solving the electronic structure of an open quantum system in steady state.[56] The DMF approach is based on the stationary condition of the effective ground state energy. As mentioned in section 2.1.1, the effective ground state energy can be written as either $\tilde{E}_0[\rho_e, \rho_n]$ or $\tilde{E}_0[\rho_L, \rho_R]$. When the former expression is used, $\delta\tilde{E}_0[\rho_e, \rho_n] = 0$ leads to the *EN* representation of the DMF approach. When the latter expression is used,

$\delta\tilde{E}_0[\rho_L, \rho_R] = 0$ leads to the *LR* representation. In either representation, the open system is described by two mean fields instead of one. In the EN representation, one mean field is for equilibrium electrons and the other is for current-carrying electrons. In the LR representation, one mean field is for electrons incident from left and the other is for electrons incident from right.

2.2.1 LR Representation

In this subsection, we will present the LR representation of the DMF approach. First, we introduce a non-interacting ground-state reference system. In the reference system, the real electron densities ρ_L and ρ_R are calculated from single particle orbitals by

$$\begin{aligned} \rho_L(\boldsymbol{r}) &= \sum_{\boldsymbol{k},\alpha\in L} f_{FD}(\tilde{\epsilon}_{\boldsymbol{k}\alpha} - \tilde{\mu})|\phi_{\boldsymbol{k}\alpha}(\boldsymbol{r})|^2, \\ \rho_R(\boldsymbol{r}) &= \sum_{\boldsymbol{k},\alpha\in R} f_{FD}(\tilde{\epsilon}_{\boldsymbol{k}\alpha} - \tilde{\mu})|\phi_{\boldsymbol{k}\alpha}(\boldsymbol{r})|^2. \end{aligned} \tag{2.26}$$

In Eqn. 2.26, $\phi_{\boldsymbol{k}\alpha}$ describes an electron incident from left (right) for $\alpha \in L$ ($\alpha \in R$); f_{FD} is the Fermi-Dirac distribution; and $\tilde{\mu} = (\mu_L + \mu_R)/2$.

Second, we pose the variational problem with constraints in terms of the single particle orbitals in the reference system. When a variation is applied to either a left- or right-going state $\phi(\boldsymbol{r})$

$$\phi(\boldsymbol{r}) \to \phi(\boldsymbol{r}) + h\xi(\boldsymbol{r}),\ h \in \mathbb{R}, \tag{2.27}$$

it is subjected to certain constraints. On the one hand, the number of electrons within the center region is conserved due to the screening effect towards the metal leads. This is reflected in the normalization of single particle orbitals, namely

$$\int_{\Omega_C} \mathrm{d}\boldsymbol{r}\phi^*(\boldsymbol{r})\phi(\boldsymbol{r}) = 1. \tag{2.28}$$

On the other hand, assuming the wavefunction in both reservoirs is known, we have the constraints

$$\begin{aligned} \xi(\boldsymbol{r})|_{\partial\Omega_C} &= 0, \\ \boldsymbol{\nabla}\xi(\boldsymbol{r})|_{\partial\Omega_C} &= \mathbf{0}, \end{aligned} \tag{2.29}$$

due to the continuity of the wavefunction. Upon the above constrained variation, the effective ground state energy $\tilde{E}_0$ is stationary, i.e.

$$\tilde{E}_0\left[\phi + h\xi\right] \geq \tilde{E}_0\left[\phi\right]. \tag{2.30}$$

This constrained variational problem can be solved with the aid of the technique of Lagrange multiplier. Define

$$F\left[\phi\right] \equiv \tilde{E}_0\left[\phi\right] - \sum_{\boldsymbol{k},\alpha} \tilde{\epsilon}_{\boldsymbol{k}\alpha} \int \mathrm{d}\boldsymbol{r} \phi^*_{\boldsymbol{k}\alpha} \phi_{\boldsymbol{k}\alpha}. \tag{2.31}$$

Then the stationary condition becomes

$$\frac{\partial F\left[\phi + h\xi\right]}{\partial h}(0) = 0. \tag{2.32}$$

Third, we will derive the mean field equations based on Eqn. 2.32. Under LDA, the effective ground state energy reads

$$\begin{aligned} \tilde{E}_0\left[\phi_{\boldsymbol{k}\alpha}\right] = -\frac{1}{2}\sum_{\boldsymbol{k},\alpha} \int \mathrm{d}\boldsymbol{r} \phi^*_{\boldsymbol{k}\alpha} \boldsymbol{\nabla}^2 \phi_{\boldsymbol{k}\alpha} + \int \mathrm{d}\boldsymbol{r} \rho_t v_{ext} + \\ \frac{1}{2}\int \mathrm{d}\boldsymbol{r}\mathrm{d}\boldsymbol{r}' \frac{\rho_t\left(\boldsymbol{r}\right)\rho_t\left(\boldsymbol{r}'\right)}{|\boldsymbol{r}-\boldsymbol{r}'|} + \int \mathrm{d}\boldsymbol{r} e_{xc}(\rho_L, \rho_R) - \frac{eV_b}{2}\int \mathrm{d}\boldsymbol{r}(\rho_L - \rho_R). \end{aligned} \tag{2.33}$$

Let ρ be the electron density, either ρ_L or ρ_R, that has been varied upon the variation in Eqn. 2.27. The first order deviation of ρ regarding h is $\delta\rho = h(\phi^*\xi + \xi^*\phi)$. The

first order deviation in the kinetic energy is

$$
\begin{aligned}
&\delta T \\
=&\delta\langle\psi|\hat{T}|\psi\rangle \\
=&-\frac{1}{2}h\int_{\Omega_C}\mathrm{d}\boldsymbol{r}\left(\xi^*\boldsymbol{\nabla}^2\phi+\phi^*\boldsymbol{\nabla}^2\xi\right) \\
=&-\frac{1}{2}h\int_{\Omega_C}\mathrm{d}\boldsymbol{r}\left[\xi^*\boldsymbol{\nabla}^2\phi+\xi\boldsymbol{\nabla}^2\phi^*+\boldsymbol{\nabla}\cdot(\phi^*\boldsymbol{\nabla}\xi-\xi\boldsymbol{\nabla}\phi^*)\right] \\
=&-\frac{1}{2}h\int_{\Omega_C}\mathrm{d}\boldsymbol{r}\left(\xi^*\boldsymbol{\nabla}^2\phi+\xi\boldsymbol{\nabla}^2\phi^*\right) \\
=&-\frac{1}{2}h\int_{\Omega_C}\mathrm{d}\boldsymbol{r}\left(\xi^*\boldsymbol{\nabla}^2\phi+\xi\boldsymbol{\nabla}^2\phi^*\right),
\end{aligned}
\tag{2.34}
$$

where we have used the boundary conditions in Eqn. 2.29 so that $\int_{\Omega_C}\mathrm{d}\boldsymbol{r}\boldsymbol{\nabla}\cdot(\phi^*\boldsymbol{\nabla}\xi-\xi\boldsymbol{\nabla}\phi^*)=\int_{\partial\Omega_C}\mathrm{d}\boldsymbol{s}\cdot(\phi^*\boldsymbol{\nabla}\xi-\xi\boldsymbol{\nabla}\phi^*)=0$. The first order deviation in the external potential energy is

$$
\delta E_{ext}=\delta\int_{\infty}\mathrm{d}\boldsymbol{r}\rho_t v_{ext}=h\int_{\Omega_C}\mathrm{d}\boldsymbol{r}\left(\phi^*\xi+\xi^*\phi\right)v_{ext}. \tag{2.35}
$$

The first order deviation in the Hartree energy is

$$
\begin{aligned}
&\delta E_H \\
=&\delta\frac{1}{2}\int_{\infty}\mathrm{d}\boldsymbol{r}\rho_t v_H \\
=&\delta\frac{1}{2}\int_{\infty}\mathrm{d}\boldsymbol{r}\int_{\infty}\mathrm{d}\boldsymbol{r}'\frac{\rho_t(\boldsymbol{r})\rho_t(\boldsymbol{r}')}{|\boldsymbol{r}-\boldsymbol{r}'|} \\
=&\frac{1}{2}\int_{\infty}\mathrm{d}\boldsymbol{r}\int_{\infty}\mathrm{d}\boldsymbol{r}'\frac{\delta\rho_t(\boldsymbol{r})\rho_t(\boldsymbol{r}')+\rho_t(\boldsymbol{r})\delta\rho_t(\boldsymbol{r}')}{|\boldsymbol{r}-\boldsymbol{r}'|} \\
=&\int_{\infty}\mathrm{d}\boldsymbol{r}\int_{\infty}\mathrm{d}\boldsymbol{r}'\frac{\delta\rho_t(\boldsymbol{r})\rho_t(\boldsymbol{r}')}{|\boldsymbol{r}-\boldsymbol{r}'|} \\
=&\int_{\infty}\mathrm{d}\boldsymbol{r}\delta\rho_t(\boldsymbol{r})v_H(\boldsymbol{r}) \\
=&h\int_{\Omega_C}\mathrm{d}\boldsymbol{r}(\phi^*\xi+\xi^*\phi)v_H.
\end{aligned}
\tag{2.36}
$$

The first order deviation in the exchange correlation energy is

$$\delta E_{xc} = \delta \int_{\infty} \mathrm{d}\boldsymbol{r} e_{xc}(\rho_L, \rho_R) = h \int_{\Omega_C} \mathrm{d}\boldsymbol{r} \frac{\partial e_{xc}}{\partial \rho} \left(\phi^* \xi + \xi^* \phi\right). \tag{2.37}$$

The first order deviation in the non-equilibrium correction term is

$$-\frac{eV_b}{2}\delta \int_{\infty} \mathrm{d}\boldsymbol{r}(\rho_L - \rho_R) = \mp \frac{eV_b}{2} h \int_{\Omega_C} \mathrm{d}\boldsymbol{r}(\phi^* \xi + \xi^* \phi), \tag{2.38}$$

where the minus (plus) sign is for the variation of $\phi_{\boldsymbol{k},\alpha\in L}$ ($\phi_{\boldsymbol{k},\alpha\in R}$). The first order deviation in the multiplier term is

$$\delta \left(-\sum_{\boldsymbol{k},\alpha} \tilde{\epsilon}_{\boldsymbol{k}\alpha} \int_{\infty} \mathrm{d}\boldsymbol{r} \phi^*_{\boldsymbol{k}\alpha} \phi_{\boldsymbol{k}\alpha} \right) = -h\tilde{\epsilon} \int_{\Omega_C} \mathrm{d}\boldsymbol{r}(\phi^* \xi + \xi^* \phi). \tag{2.39}$$

In summary, the stationary condition Eqn. 2.32 becomes

$$\int_{\Omega_C} \mathrm{d}\boldsymbol{r} \xi^* \left(-\frac{1}{2}\boldsymbol{\nabla}^2 + v_{ext} + v_H + \frac{\partial e_{xc}}{\partial \rho} \mp \frac{eV_b}{2} - \tilde{\epsilon} \right) \phi + c.c. = 0. \tag{2.40}$$

Since the variation ξ can take different forms, we have mean field equations

$$\begin{aligned} (-\frac{1}{2}\boldsymbol{\nabla}^2 + v_{ext} + v_H + \frac{\partial e_{xc}}{\partial \rho_L} - \frac{eV_b}{2})\phi_{\boldsymbol{k}\alpha} =& \tilde{\epsilon}_{\boldsymbol{k}\alpha}\phi_{\boldsymbol{k}\alpha}, \\ (-\frac{1}{2}\boldsymbol{\nabla}^2 + v_{ext} + v_H + \frac{\partial e_{xc}}{\partial \rho_R} + \frac{eV_b}{2})\phi_{\boldsymbol{k}\beta} =& \tilde{\epsilon}_{\boldsymbol{k}\beta}\phi_{\boldsymbol{k}\beta}, \end{aligned} \tag{2.41}$$

where $\alpha \in L$ and $\beta \in R$. When the exchange correlation energy is approximated under GGA with $E_{xc} = \int \mathrm{d}\boldsymbol{r} e_{xc}(\rho_L, \rho_R, \boldsymbol{\nabla}\rho_t)$, the mean field Hamiltonians in Eqn. 2.41 take a different form as shown below

$$\begin{aligned} \tilde{\hat{h}}_L =& -\frac{1}{2}\boldsymbol{\nabla}^2 + v_{ext} + v_H + \frac{\partial e_{xc}}{\partial \rho_L} - \partial_i \frac{\partial e_{xc}}{\partial \partial_i \rho_t} - \frac{eV_b}{2}, \\ \tilde{\hat{h}}_R =& -\frac{1}{2}\boldsymbol{\nabla}^2 + v_{ext} + v_H + \frac{\partial e_{xc}}{\partial \rho_R} - \partial_i \frac{\partial e_{xc}}{\partial \partial_i \rho_t} + \frac{eV_b}{2}. \end{aligned} \tag{2.42}$$

Eqn. 2.41 and 2.42 indicate that left- and right-going electrons experience different mean field potentials when the open system is in non-equilibrium steady state. Furthermore, the $-eV_b/2$ and $eV_b/2$ terms are the downward and upward shifts to $\hat{h}_L$ and $\hat{h}_R$ respectively. Here, $\hat{h}_L$ and $\hat{h}_R$ are the mean field Hamiltonians for the steady-state reference system. Therefore, the correspondence between the real system and the effective system in the LR representation matches very well with the correspondence discussed in section 2.1.2.

2.2.2 EN Representation

In the LR representation of the DMF approach, the electron densities ρ_L and ρ_R are hard to compute. As a result, it is formidable to solve Eqn. 2.41. In seeking for practically solvable mean field equations, we will present the EN representation in this subsection.

For the real open system in steady state, it is clear that the electrons below μ_r contribute to the equilibrium electron density ρ_e while those between μ_r and μ_l contribute to the current-carrying electron density ρ_n. Therefore we introduce a steady-state reference system where the real electron densities ρ_e and ρ_n are calculated from single particle orbitals by

$$\begin{aligned} \rho_e(\boldsymbol{r}) &= \sum_{\boldsymbol{k},\alpha\in e} f_{FD}(\epsilon_{\boldsymbol{k}\alpha}-\mu_R)|\phi_{\boldsymbol{k}\alpha}(\boldsymbol{r})|^2, \\ \rho_n(\boldsymbol{r}) &= \sum_{\boldsymbol{k},\alpha\in n} [f_{FD}(\epsilon_{\boldsymbol{k}\alpha}-\mu_L)-f_{FD}(\epsilon_{\boldsymbol{k}\alpha}-\mu_R)]|\phi_{\boldsymbol{k}\alpha}(\boldsymbol{r})|^2. \end{aligned} \tag{2.43}$$

In Eqn. 2.43, f_{FD} is the Fermi-Dirac distribution; $f_{FD}(\epsilon_{\boldsymbol{k}\alpha}-\mu_R)$ and $f_{FD}(\epsilon_{\boldsymbol{k}\alpha}-\mu_L)-f_{FD}(\epsilon_{\boldsymbol{k}\alpha}-\mu_R)\}$ together define the non-equilibrium distribution.

In the EN representation, the effective ground state energy functional under LDA

reads

$$\begin{aligned}\tilde{E}_0\left[\phi_{\boldsymbol{k}\alpha}\right] = -\frac{1}{2}\sum_{\boldsymbol{k},\alpha}\int \mathrm{d}\boldsymbol{r}\phi^*_{\boldsymbol{k}\alpha}\boldsymbol{\nabla}^2\phi_{\boldsymbol{k}\alpha} + \int \mathrm{d}\boldsymbol{r}\rho_t v_{ext} + \\ \frac{1}{2}\int \mathrm{d}\boldsymbol{r}\mathrm{d}\boldsymbol{r}'\frac{\rho_t\left(\boldsymbol{r}\right)\rho_t\left(\boldsymbol{r}'\right)}{|\boldsymbol{r}-\boldsymbol{r}'|} + \int \mathrm{d}\boldsymbol{r}e_{xc}(\rho_e,\rho_n) - \frac{eV_b}{2}\int \mathrm{d}\boldsymbol{r}\rho_n.\end{aligned} \tag{2.44}$$

The stationary condition of the effective ground state energy leads to the following mean field equations

$$\begin{aligned}(-\frac{1}{2}\boldsymbol{\nabla}^2 + v_{ext} + v_H + \frac{\partial e_{xc}}{\partial \rho_e})\phi_{\boldsymbol{k}\alpha} =& \tilde{\epsilon}_{\boldsymbol{k}\alpha}\phi_{\boldsymbol{k}\alpha}, \\ (-\frac{1}{2}\boldsymbol{\nabla}^2 + v_{ext} + v_H + \frac{\partial e_{xc}}{\partial \rho_n} - \frac{eV_b}{2})\phi_{\boldsymbol{k}\beta} =& \tilde{\epsilon}_{\boldsymbol{k}\beta}\phi_{\boldsymbol{k}\beta},\end{aligned} \tag{2.45}$$

where $\alpha \in e$ and $\beta \in n$. When the exchange correlation energy is approximated in GGA with $E_{xc} = \int \mathrm{d}\boldsymbol{r}e_{xc}(\rho_e, \rho_n, \boldsymbol{\nabla}\rho_t)$, the mean field Hamiltonians become

$$\begin{aligned}\tilde{\hat{h}}_e =& -\frac{1}{2}\boldsymbol{\nabla}^2 + v_{ext} + v_H + \frac{\partial e_{xc}}{\partial \rho_e} - \partial_i\frac{\partial e_{xc}}{\partial\partial_i\rho_t}, \\ \tilde{\hat{h}}_n =& -\frac{1}{2}\boldsymbol{\nabla}^2 + v_{ext} + v_H + \frac{\partial e_{xc}}{\partial \rho_n} - \partial_i\frac{\partial e_{xc}}{\partial\partial_i\rho_t} - \frac{eV_b}{2}.\end{aligned} \tag{2.46}$$

Note that the mean field Hamiltonians in Eqn. 2.45 and 2.46 are for the ground-state reference system. In order to calculate electron densities by Eqn. 2.43, we need the Hamiltonians for the steady-state reference system. In other words, it remains to specify the correspondence between the real non-equilibrium system and the effective equilibrium system in the EN representation. As discussed in section 2.2.1, in the LR representation,

$$\begin{aligned}\hat{h}_L =& \tilde{\hat{h}}_L + \frac{eV_b}{2}, \\ \hat{h}_R =& \tilde{\hat{h}}_R - \frac{eV_b}{2},\end{aligned} \tag{2.47}$$

which is a result of the term $-eV_bN_n/2$ in the effective ground state energy. Differently, in the EN representation, the term $-eV_bN_n/2$ affects $\tilde{\hat{h}}_n$ but has no contribu-

tion to $\tilde{\hat{h}}_e$. It indicates that the correspondence in the EN representation is

$$\begin{aligned} \hat{h}_e =& \tilde{\hat{h}}_e, \\ \hat{h}_n =& \tilde{\hat{h}}_n + \frac{eV_b}{2}. \end{aligned} \tag{2.48}$$

The mean field Hamiltonians $\hat{h}_e$ and $\hat{h}_n$ in Eqn. 2.48 govern the following eigenvalue equations

$$\begin{aligned} \hat{h}_e \phi_{\boldsymbol{k}\alpha} =& \epsilon_{\boldsymbol{k}\alpha} \phi_{\boldsymbol{k}\alpha}, \\ \hat{h}_n \phi_{\boldsymbol{k}\beta} =& \epsilon_{\boldsymbol{k}\beta} \phi_{\boldsymbol{k}\beta}, \end{aligned} \tag{2.49}$$

where $\alpha \in e$ and $\beta \in n$.

Eqn. 2.49 and Eqn. 2.43 need to be satisfied simultaneously. They can be solved self-consistently with the aid of the Green's function expressions for the electron densities. As a final remark, we need the concrete form of the exchange correlation potentials before solving the mean field equations.

2.3 Generalized Thomas-Fermi-Dirac Model

In this section, we will generalize the TFD model to non-equilibrium cases and derive the exchange and kinetic energies analytically for a biased non-interacting uniform electron gas.[55] In the generalized TFD (gTFD) model, the equilibrium and current-carrying electron densities indeed determine the exchange and kinetic energies. From the exchange energy functional obtained in the gTFD model, we will also derive the exchange potentials which are ready to be applied in the DMF approach.

2.3.1 Non-equilibrium Non-interacting Free Electron Gas

Consider some non-interacting free electron gas in a box of dimensions $L \times L \times L$ with periodic boundary conditions, the electrons are described by the Hamiltonian

$$\hat{H} = \frac{\hat{\boldsymbol{P}}^2}{2m} + \text{const.} \tag{2.50}$$

The eigenvalue equation for the above Hamiltonian

$$\hat{H}\phi_{\boldsymbol{k}\sigma}(\boldsymbol{r}, s) = E\phi_{\boldsymbol{k}\sigma}(\boldsymbol{r}, s) \tag{2.51}$$

bears the solution

$$\phi_{\boldsymbol{k}\sigma}(\boldsymbol{r}, s) = \frac{1}{L^{3/2}} e^{i\boldsymbol{k}\cdot\boldsymbol{r}} \chi_\sigma(s). \tag{2.52}$$

In Eqn. 2.52, $\boldsymbol{k} = \frac{2\pi}{L}\boldsymbol{n}$ with $n_i = 0, \pm 1, \pm 2, \cdots$ is the wavevector; $\sigma = -1, 1$ is the spin index; $\chi_\sigma(s) = 1$ if $s = \sigma$ and $\chi_\sigma(s) = 0$ if $s \neq \sigma$. $\chi_\sigma(s)$ satisfies

$$\sum_s \chi_\sigma(s)\chi_{\sigma'}(s) = \delta_{\sigma\sigma'}. \tag{2.53}$$

The eigenstates in Eqn. 2.52 are normalized in the following way

$$\langle \boldsymbol{k}'\sigma' |\, \boldsymbol{k}\sigma \rangle = \sum_s \int \mathrm{d}\boldsymbol{r} \frac{1}{L^3} e^{i(\boldsymbol{k}-\boldsymbol{k}')\cdot\boldsymbol{r}} \chi_{\sigma'}(s)\chi_\sigma(s) = \delta_{\boldsymbol{k}\boldsymbol{k}'}\delta_{\sigma\sigma'}. \tag{2.54}$$

In the TFD model, the electron gas is in equilibrium ground state thus all single particle states below Fermi energy $\epsilon_F = k_F^2/2$ are occupied.[65] Here k_F is the Fermi wavevector. The occupied single particle states form a sphere of radius k_F in momentum space as shown in Fig. 2.3.

In order to drive the electron gas in the TFD model into non-equilibrium, we sandwich it between two reservoirs of non-interacting and free electron gas as depic-

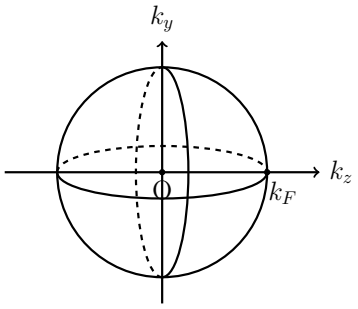

Figure 2.3: Occupation of states in k space for the TFD model. The occupation forms a sphere with radius of k_F (the Fermi wavevector).

ted in Fig. 2.4. Moreover, the reservoirs are connected to a battery. When a positive

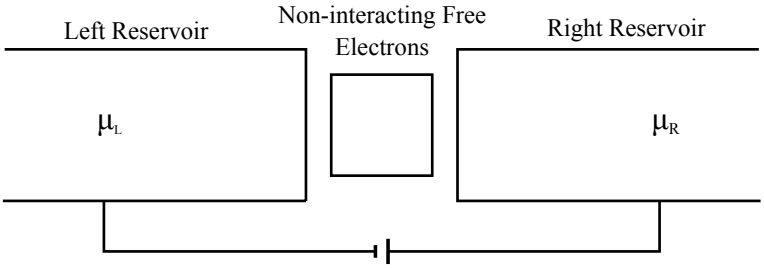

Figure 2.4: Model setup for the gTFD model. A box of non-interacting free electron gas is sandwiched between two reservoirs which are connected to a battery. Electrons in both reservoirs are also free and non-interacting. The difference between left and right chemical potentials determines the bias voltage by $eV_b = \mu_L - \mu_R$.

bias voltage is applied, the left chemical potential $\mu_L = k_L^2/2$ is higher than the right one $\mu_R = k_R^2/2$. As a result, the occupation of states in k space becomes Fig. 2.5 where one beholds two hemispheres with different radii, the right half with radius k_L (the Fermi wavevector for the left reservoir) and the left half with radius k_R (the Fermi wavevector for the right reservoir).

2.3.2 Exchange Energy Density

In this subsection, we will derive the exchange energy density $\mathcal{E}_x^n$ of the non-equilibrium electron gas in the gTFD model. We will first express $\mathcal{E}_x^n$ in terms of the Fermi wavevectors. Then, after change of variables, we will express it as a function of the electron densities.

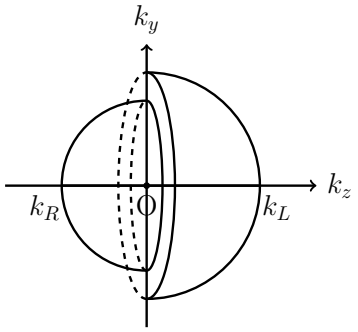

Figure 2.5: Occupation of states in k space for the gTFD model under finite bias. The occupation forms two hemispheres, one with radius k_R (the Fermi wavevector for the right reservoir) and the other with radius k_L (the Fermi wavevector for the left reservoir).

Let Φ_{SD} be a single Slater determinant of the occupied eigenstates

$$\Phi_{SD} = \det(\phi_{\boldsymbol{k}_1\sigma_1}, \phi_{\boldsymbol{k}_2\sigma_2}, \cdots, \phi_{\boldsymbol{k}_N\sigma_N}). \tag{2.55}$$

The Coulomb interaction between electrons writes

$$\hat{W} = \sum_{i\neq j} \frac{1}{|\boldsymbol{r}_i - \boldsymbol{r}_j|}. \tag{2.56}$$

Then the exchange energy density for the gTFD model is

$$\begin{aligned}
\mathcal{E}_x^n &\equiv \frac{1}{V}\left(\langle\Phi_{SD}|\,\hat{W}\,|\Phi_{SD}\rangle - E_H\left[\rho\right]\right) \\
&= -\frac{1}{2V}\sum_{\boldsymbol{k},\sigma,\boldsymbol{k}',\sigma'}\left[\phi_{\boldsymbol{k}'\sigma'}\phi_{\boldsymbol{k}\sigma}\left|\hat{W}\right|\phi_{\boldsymbol{k}\sigma}\phi_{\boldsymbol{k}'\sigma'}\right] \\
&= -\frac{1}{2V\left(2\pi\right)^6}\sum_{\sigma,\sigma',s,s'}\int \mathrm{d}\boldsymbol{k}\mathrm{d}\boldsymbol{k}'\mathrm{d}\boldsymbol{r}_1\mathrm{d}\boldsymbol{r}_2\frac{e^{i(\boldsymbol{k}-\boldsymbol{k}')\cdot(\boldsymbol{r}_1-\boldsymbol{r}_2)}}{|\boldsymbol{r}_1-\boldsymbol{r}_2|}\chi_{\sigma'}(s')\chi_{\sigma}(s) \\
&= -\frac{1}{\left(2\pi\right)^6 V}\int \mathrm{d}\boldsymbol{k}\mathrm{d}\boldsymbol{k}'\mathrm{d}\boldsymbol{r}_1\mathrm{d}\boldsymbol{r}_2\frac{e^{i(\boldsymbol{k}-\boldsymbol{k}')\cdot(\boldsymbol{r}_1-\boldsymbol{r}_2)}}{|\boldsymbol{r}_1-\boldsymbol{r}_2|} \\
&\overset{5}{=} -\frac{1}{\left(2\pi\right)^6 V}\int \mathrm{d}\boldsymbol{k}\mathrm{d}\boldsymbol{k}'\mathrm{d}\boldsymbol{r}\mathrm{d}\boldsymbol{s}\left|\frac{\partial(\boldsymbol{r}_1,\boldsymbol{r}_2)}{\partial(\boldsymbol{r},\boldsymbol{s})}\right|\frac{e^{i(\boldsymbol{k}-\boldsymbol{k}')\cdot\boldsymbol{r}}}{|\boldsymbol{r}|} \\
&= -\frac{1}{\left(2\pi\right)^6}\int \mathrm{d}\boldsymbol{k}\mathrm{d}\boldsymbol{k}'\mathrm{d}\boldsymbol{r}\frac{e^{i(\boldsymbol{k}-\boldsymbol{k}')\cdot\boldsymbol{r}}}{|\boldsymbol{r}|}\cdot\frac{1}{V}\int \mathrm{d}\boldsymbol{s}
\end{aligned}$$

$$
\begin{aligned}
&= -\frac{1}{(2\pi)^6}\int \mathrm{d}\boldsymbol{k}\mathrm{d}\boldsymbol{k}'\mathrm{d}\boldsymbol{r}\frac{e^{i(\boldsymbol{k}-\boldsymbol{k}')\cdot\boldsymbol{r}}}{|\boldsymbol{r}|} \\
&\overset{8}{=} \lim_{\mu\to 0^+} -\frac{1}{(2\pi)^6}\int \mathrm{d}\boldsymbol{k}\mathrm{d}\boldsymbol{k}'\mathrm{d}\boldsymbol{r}e^{-\mu r}\frac{e^{i(\boldsymbol{k}-\boldsymbol{k}')\cdot\boldsymbol{r}}}{|\boldsymbol{r}|} \\
&= \lim_{\mu\to 0^+} -\frac{1}{(2\pi)^6}\int \mathrm{d}\boldsymbol{k}\mathrm{d}\boldsymbol{k}'\cdot r^2 sin\theta \mathrm{d}r\mathrm{d}\theta\mathrm{d}\varphi e^{-\mu r}\frac{e^{i|\boldsymbol{k}-\boldsymbol{k}'|rcos\theta}}{r} \\
&= \lim_{\mu\to 0^+} -\frac{1}{(2\pi)^6}\int \mathrm{d}\boldsymbol{k}\mathrm{d}\boldsymbol{k}'\cdot 2\pi r\mathrm{d}r\mathrm{d}\left(-cos\theta\right)e^{-\mu r}e^{i|\boldsymbol{k}-\boldsymbol{k}'|rcos\theta} \\
&= \lim_{\mu\to 0^+} -\frac{1}{(2\pi)^6}\int \mathrm{d}\boldsymbol{k}\mathrm{d}\boldsymbol{k}'\cdot 2\pi\mathrm{d}r\frac{e^{(-\mu+i|\boldsymbol{k}-\boldsymbol{k}'|)r}-e^{(-\mu-i|\boldsymbol{k}-\boldsymbol{k}'|)r}}{i\left|\boldsymbol{k}-\boldsymbol{k}'\right|} \\
&\overset{12}{=} \lim_{\mu\to 0^+} -\frac{1}{(2\pi)^6}\int \mathrm{d}\boldsymbol{k}\mathrm{d}\boldsymbol{k}'\cdot 2\pi\frac{\frac{1}{\mu-i|\boldsymbol{k}-\boldsymbol{k}'|}-\frac{1}{\mu+i|\boldsymbol{k}-\boldsymbol{k}'|}}{i\left|\boldsymbol{k}-\boldsymbol{k}'\right|} \\
&= -\frac{4\pi}{(2\pi)^6}\int \mathrm{d}\boldsymbol{k}\mathrm{d}\boldsymbol{k}'\frac{1}{\left|\boldsymbol{k}-\boldsymbol{k}'\right|^2}
\end{aligned}
\tag{2.57}
$$

In the step 5, we changed variables from $(\boldsymbol{r}_1, \boldsymbol{r}_2)$ to $(\boldsymbol{r}, \boldsymbol{s})$ by $\boldsymbol{r} = \boldsymbol{r}_1 - \boldsymbol{r}_2$ and $\boldsymbol{s} = \boldsymbol{r}_2$. In the step 8, we multiplied a factor of $e^{-\mu r}$ to the integrand with $\mu \to 0^+$. In the step 12, we took the limit of $L \to \infty$. Next we split the integral in Eqn. 2.57 into three parts

$$
\int_\Omega\int_\Omega = \int_{\Omega_1}\int_{\Omega_1} + 2\int_{\Omega_2}\int_{\Omega_1} + \int_{\Omega_2}\int_{\Omega_2} \equiv I_1 + I_2 + I_3 \tag{2.58}
$$

where $\Omega = \Omega_1 + \Omega_2$ as shown in Fig. 2.6. The first integral is

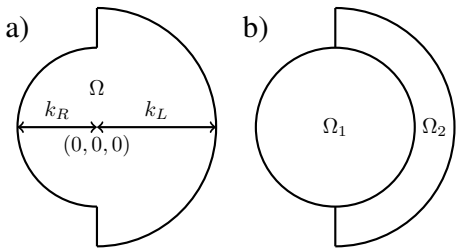

Figure 2.6: Division of the occupation of states Ω (a) into Ω_1 and Ω_2 (b).

$$
I_1 = -\frac{4\pi}{(2\pi)^6}\int_{\Omega_1}\mathrm{d}\boldsymbol{k}\int_{\Omega_1} k'^2 sin\theta'\mathrm{d}k'\mathrm{d}\theta'\mathrm{d}\varphi'\frac{1}{k^2+k'^2-2kk'cos\theta'}
$$

$$
\begin{aligned}
&= -\frac{4\pi}{(2\pi)^6}\int_{\Omega_1} \mathrm{d}\boldsymbol{k}\int_0^{k_R} \mathrm{d}k'\pi\frac{k'}{k}\left[ln(k+k')^2 - ln(k-k')^2\right] \qquad (2.59)\\
&= -\frac{1}{2\pi^3}\int_0^{k_R}\mathrm{d}k\int_0^{k_R}\mathrm{d}k'kk'\left[ln(k+k') - ln|k-k'|\right]\\
&= -\frac{1}{4\pi^3}k_R^4
\end{aligned}
$$

The second integral is tackled similarly bearing the result

$$
I_2 = -\frac{1}{16\pi^3}\Big[(k_L^2-k_R^2)^2 ln\Big(\frac{k_L-k_R}{k_R+k_L}\Big) + 2(k_R^3k_L + k_Rk_L^3 - 2k_R^4)\Big]. \qquad (2.60)
$$

The third integral is a bit complex and can be tackled as follows

$$
\begin{aligned}
I_3 = &-\frac{4\pi}{(2\pi)^6}\int_{k_1}^{k_2}\mathrm{d}k\int_{k_1}^{k_2}\mathrm{d}k'\int_0^{\frac{\pi}{2}}\mathrm{d}\theta\int_0^{\frac{\pi}{2}}\mathrm{d}\theta'\int_0^{2\pi}\mathrm{d}\varphi\int_0^{2\pi}\mathrm{d}\varphi'\\
&\frac{k^2k'^2 sin\theta sin\theta'}{k^2+k'^2-2kk'\left[sin\theta sin\theta' cos\left(\varphi-\varphi'\right)+cos\theta cos\theta'\right]}\\
= &-\frac{1}{8\pi^3}\int_{k_1}^{k_2}k\mathrm{d}k\int_{k_1}^{k_2}k'\mathrm{d}k'\int_0^{\frac{\pi}{2}}\mathrm{d}cos\theta\int_0^{\frac{\pi}{2}}\mathrm{d}cos\theta'\\
&\frac{1}{\sqrt{cos^2\theta+cos^2\theta'+Ccos\theta cos\theta'+\frac{1}{4}C^2-1}} \qquad (2.61)\\
= &-\frac{1}{16\pi^3}\int_{k_1}^{k_2}k\mathrm{d}k\int_{k_1}^{k_2}k'\mathrm{d}k'\Big\{-2ln\Big(-2+\frac{k}{k'}+\frac{k'}{k}\Big)\\
&+ln\Big[\frac{2k^2k'^2}{k^4+k'^4-\left(k^2+k'^2\right)\left|k^2-k'^2\right|}\Big]\Big\}\\
= &-\frac{1}{16\pi^3}\Big[-(k_L^2-k_R^2)^2ln(k_L-k_R)+(k_L^4-2k_R^2k_L^2)ln(k_L)\\
&+k_R^4ln(k_R)+k_R^4-k_R^3k_L-\frac{1}{2}k_R^2k_L^2-k_Rk_L^3+\frac{3}{2}k_L^4\Big].
\end{aligned}
$$

In Eqn. 2.61, $C=-(k^2+k'^2)/kk' < -2$ when $k \neq k'$.[†] Finally, summing up I_1, I_2, and I_3, we get the exchange energy density as a function of the Fermi wavevectors

$$
\mathcal{E}_x^n(k_L,k_R) = -\frac{1}{16\pi^3}\Big[-\left(k_L^2-k_R^2\right)^2 ln\left(k_R+k_L\right)+\left(k_L^4-2k_R^2k_L^2\right)ln\left(k_L\right)
$$

[†] I_3 can be checked by *Mathematica* with the codes listed in Appendix A.

$$+k_R^4 ln\left(k_R\right)+k_R^4+k_R^3k_L-\frac{1}{2}k_R^2k_L^2+k_Rk_L^3+\frac{3}{2}k_L^4\Big]. \tag{2.62}$$

Now we change variables from the Fermi wavevectors to the electron densities for the exchange energy density. In the gTFD model, the total electron density ρ_t and current-carrying electron density ρ_n are

$$\begin{aligned}\rho_t =&\frac{1}{6\pi^2}\left(k_L^3+k_R^3\right),\\ \rho_n =&\frac{1}{6\pi^2}\left(k_L^3-k_R^3\right).\end{aligned} \tag{2.63}$$

Define a non-equilibrium index $\eta \equiv \rho_n/\rho_t$ which measures the local degree of non-equilibrium. In terms of ρ_t and η, we rewrite the exchange energy density as

$$\begin{aligned}\mathcal{E}_x^n(\rho_t,\eta) =&\frac{1}{4}\left(1+\eta\right)^{4/3}\Big[-\left(1-\tilde{\eta}^2\right)^2 ln\left(1+\tilde{\eta}\right)+\tilde{\eta}^4 ln\left(\tilde{\eta}\right)\\ &+\tilde{\eta}^4+\tilde{\eta}^3-\frac{1}{2}\tilde{\eta}^2+\tilde{\eta}+\frac{3}{2}\Big]\mathcal{E}_x^0(\rho_t).\end{aligned} \tag{2.64}$$

In Eqn. 2.64, $\mathcal{E}_x^0(\rho_t) = -(3\pi^2\rho_t)^{4/3}/4\pi^3$ is the exchange energy density for the TFD model; $\tilde{\eta} = [(1-\eta)/(1+\eta)]^{1/3}$; and the prefactor $f(\eta) = \mathcal{E}_x^n/\mathcal{E}_x^0$ contains the non-equilibrium correction. As shown in Fig. 2.7, when $\eta \to 0$, $f \to 1$. Therefore, the gTFD exchange energy density falls back to the TFD result under zero bias which is expected. As η increases, f monotonically decreases thus the non-equilibrium correction becomes larger. When $\eta \to 1$, $f \to 0.9449$. Therefore, the highest non-equilibrium correction to the exchange energy density is about 5.5%. Since $\mathcal{E}_x^0 < 0$ and $0 < f \leq 1$, $\mathcal{E}_x^n$ is always greater than the TFD result $\mathcal{E}_x^0$.

2.3.3 Kinetic Energy Density

In this subsection, we derive the kinetic energy density $\mathcal{T}^n$ of the non-equilibrium electron gas in the gTFD model. We first divide the integral region Ω into Ω_3 and Ω_4 as shown in Fig. 2.8. Then the calculation follows

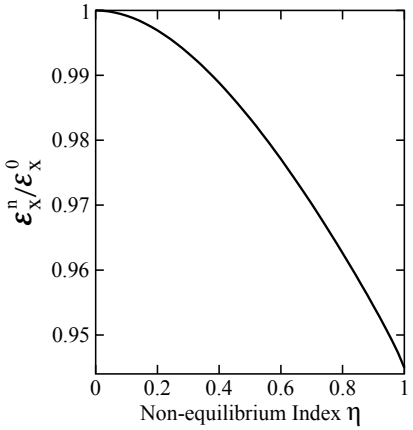

Figure 2.7: Non-equilibrium correction factor $f(\eta) = \mathcal{E}_x^n/\mathcal{E}_x^0$ versus the non-equilibrium index η. $\mathcal{E}_x^n$ and $\mathcal{E}_x^0$ are the exchange energy densities for the gTFD and TFD models respectively.

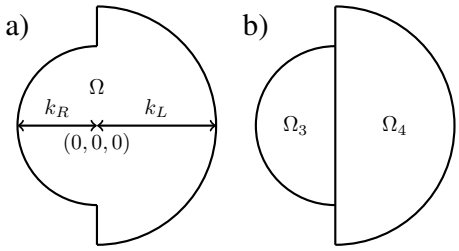

Figure 2.8: Division of the occupation of states Ω (a) into Ω_3 and Ω_4 (b).

$$
\begin{aligned}
&\mathcal{T}^n \equiv \langle \Phi_{SD}| \sum_{i=1}^{N} \hat{t}_i |\Phi_{SD}\rangle \\
=&\frac{1}{V}\sum_{\boldsymbol{k},\sigma}\langle \boldsymbol{k}\sigma|\hat{t}|\boldsymbol{k}\sigma\rangle = \frac{1}{V}\sum_{\boldsymbol{k},\sigma}\frac{k^2}{2} = \frac{1}{V}\sum_{\boldsymbol{k}} k^2 \\
=&\frac{1}{V}\int\limits_{\Omega_3+\Omega_4}\frac{\mathrm{d}\boldsymbol{k}}{(2\pi/L)^3}k^2 = \frac{1}{20\pi^2}(k_R^5 + k_L^5) \\
=&\frac{1}{2}\left[(1-\eta)^{5/3} + (1+\eta)^{5/3}\right]\mathcal{T}^0(\rho_t).
\end{aligned}
\tag{2.65}
$$

In Eqn. 2.65, $\mathcal{T}^0(\rho_t) = (3\pi^2\rho_t)^{5/3}/10\pi^2$ is the TFD kinetic energy density; η is the previously defined non-equilibrium index; and the prefactor $g(\eta) = \mathcal{T}^n/\mathcal{T}^0$ contains the non-equilibrium correction. As shown in Fig. 2.9, when $\eta \to 0$, $g \to 1$. Therefore, the gTFD kinetic energy density falls back to the TFD result under zero bias which is expected. As η increases, g monotonically increases thus the non-equilibrium correction becomes larger. When $\eta \to 1$, $g \to 1.5874$. Therefore, the

highest non-equilibrium correction to the kinetic energy density is about 58.74%. Since $\mathcal{T}^0 > 0$ and $g \geq 1$, the gTFD kinetic energy density $\mathcal{T}^n$ is always greater than the TFD result $\mathcal{T}^0$.

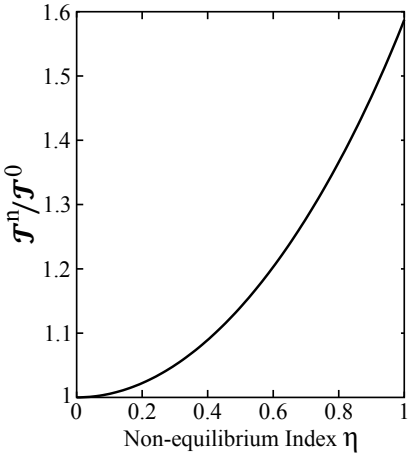

Figure 2.9: Non-equilibrium correction factor $g(\eta) = \mathcal{T}^n/\mathcal{T}^0$ versus the non-equilibrium index η. $\mathcal{T}^n$ and $\mathcal{T}^0$ are the kinetic energy densities for the gTFD and TFD models respectively.

Similar to GS-DFT, the kinetic energy functional for the non-equilibrium non-interacting free electron gas derived here may be a bad approximation to the exact one for general cases. Actually in the DMF approach, the kinetic energy is calculated from single particle orbitals in the non-interacting reference system instead of $\mathcal{T}^n$.

2.3.4 Exchange Potentials from the gTFD Model

In this subsection, we will derive the exchange potentials for equilibrium and current-carrying electrons based on the gTFD exchange energy density $\mathcal{E}_x^n$ in Eqn. 2.64.

When the exchange energy density is approximated by LDA with $e_x = \mathcal{E}_x^n(\rho_e, \rho_n)$, the exchange potentials $v_x^e = \partial e_x/\partial\rho_e\big|_{\rho_n}$ and $v_x^n = \partial e_x/\partial\rho_n\big|_{\rho_e}$ are

$$v_x^e = \frac{1}{4}(1+\eta)^{1/3}\Big[\frac{(1-\tilde{\eta}^2)(1-\tilde{\eta})}{\tilde{\eta}} ln(1+\tilde{\eta}) + \tilde{\eta} ln\tilde{\eta} - \frac{1}{2}\tilde{\eta}^2 + 2\tilde{\eta} + \frac{5}{2}\Big] v_x^0,$$
$$v_x^n = \frac{1}{4}(1+\eta)^{1/3}\Big[-2(1-\tilde{\eta}^2) ln(1+\tilde{\eta}) - \tilde{\eta}^2 + 2\tilde{\eta} + 3\Big] v_x^0. \qquad (2.66)$$

In Eqn. 2.66, $v_x^0 = \mathrm{d}\mathcal{E}_x^0/\mathrm{d}\rho_t = -(3\rho_t/\pi)^{1/3}$ is the exchange potential for the TFD model; the prefactors $p(\eta) = v_x^e/v_x^0$ and $q(\eta) = v_x^n/v_x^0$ contain the non-equilibrium correction. As shown in Fig. 2.10a, when $\eta \to 0$, $p \to 1$. Therefore the exchange potential for the equilibrium electrons falls back to the TFD result under zero bias. As η increases, p increases monotonically thus the non-equilibrium correction becomes larger. When $\eta \to 1, p \to 1.102$. Therefore, the highest non-equilibrium correction to v_x^e is about 10.2%. However, the non-equilibrium correction to v_x^e is smaller than 2% when $\eta < 0.9$. Since $v_x^0 < 0$ and $p > 1$, the non-equilibrium correction tends to decrease the exchange potential for the equilibrium electrons. As shown in Fig. 2.10b, when $\eta \to 0$, $q \to 1$. Therefore the exchange potential for the non-equilibrium electrons also falls back to the TFD result under zero bias. As η increases, q decreases monotonically thus the non-equilibrium correction becomes larger. When $\eta \to 1$, $q \to 0.9449$. Therefore, the highest non-equilibrium correction to v_x^n is about 5.5%. Since $v_x^0 < 0$ and $0 < q < 1$, the non-equilibrium correction tends to increase the exchange potential for the non-equilibrium electrons.

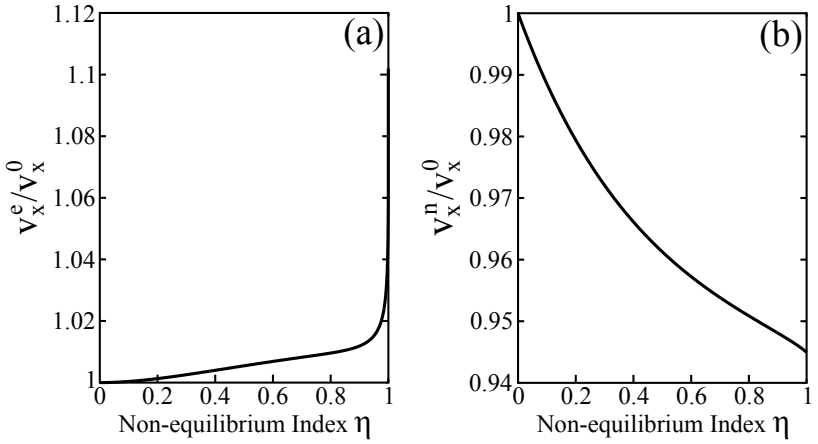

Figure 2.10: Non-equilibrium correction factors $p(\eta) = v_x^e/v_x^0$ (a) and $q(\eta) = v_x^n/v_x^0$ (b) versus the non-equilibrium index η. v_x^0 is the exchange potential for the TFD model. v_x^e (v_x^n) is the exchange potential for the equilibrium (current-carrying) electrons in the gTFD model.

When the exchange energy density is approximated by GGA with $e_x =$

$\mathcal{E}_x^n(\rho_e, \rho_n)F(\rho_t, \boldsymbol{\nabla}\rho_t)$, the exchange potentials are

$$\begin{aligned} v_x^e =& \frac{\partial e_x}{\partial \rho_e} - \partial_i \frac{\partial e_x}{\partial \partial_i \rho_t} = \frac{\partial \mathcal{E}_x^n}{\partial \rho_e} F + \mathcal{E}_x^g \frac{\partial F}{\partial \rho_t} - \partial_i (\mathcal{E}_x^n \frac{\partial F}{\partial \partial_i \rho_t}), \\ v_x^n =& \frac{\partial e_x}{\partial \rho_n} - \partial_i \frac{\partial e_x}{\partial \partial_i \rho_t} = \frac{\partial \mathcal{E}_x^n}{\partial \rho_n} F + \mathcal{E}_x^n \frac{\partial F}{\partial \rho_t} - \partial_i (\mathcal{E}_x^n \frac{\partial F}{\partial \partial_i \rho_t}), \end{aligned} \tag{2.67}$$

where $\partial \mathcal{E}_x^n / \partial \rho_e$ and $\partial \mathcal{E}_x^n / \partial \rho_n$ are given in Eqn. 2.66. Note that the explicit form of the exchange potentials in Eqn. 2.67 depends on the gradient correction $F(\rho_t, \boldsymbol{\nabla}\rho_t)$ which varies among different flavors of GGA.

2.4 Implementation in SIESTA

In this section, we will present the implementation of SS-DFT in SIESTA.[56] The goal is to devise a self-consistent procedure to solve the coupled mean field equations in the EN representation of the DMF approach. Especially, the gTFD exchange energy density $\mathcal{E}_x^n$ will be used to include non-equilibrium effects in the energy functional level. For clarity, we will first review the Green's function expression of the electron densities and the formalism in the representation with localized basis functions.

2.4.1 Formula for the Electron Densities

In this subsection, we review the Green's function expression of the electron densities ρ_e and ρ_n. In general, the lesser Green's function is defined as

$$G^<(\boldsymbol{r}t, \boldsymbol{r}'t') = i\langle \hat{\psi}^\dagger(\boldsymbol{r}'t')\hat{\psi}(\boldsymbol{r}t)\rangle. \tag{2.68}$$

The total electron density ρ_t can be expressed in terms of the lesser Green's function, namely

$$\rho_t(\boldsymbol{r}, t) = -iG^<(\boldsymbol{r}t, \boldsymbol{r}t^+). \tag{2.69}$$

For a molecular junction in steady state, the Green's function only depends on the time difference $\Delta = t - t'$. Thus Fourier transform can be applied

$$\rho_t(\boldsymbol{r}) = -\frac{i}{2\pi}\int \mathrm{d}\epsilon G^<(\boldsymbol{r},\epsilon), \tag{2.70}$$

with

$$G^<(\boldsymbol{r},\epsilon) = \int \mathrm{d}\Delta e^{-i\epsilon\Delta} G^<(\boldsymbol{r},\Delta). \tag{2.71}$$

Then we split the integral in Eqn. 2.70 into two parts and get the equilibrium electron density ρ_e and current-carrying electron density ρ_n,

$$\begin{aligned}\rho_e(\boldsymbol{r}) &= -\frac{i}{2\pi}\int_{-\infty}^{\mu_R} \mathrm{d}\epsilon G^<(\boldsymbol{r},\epsilon),\\ \rho_n(\boldsymbol{r}) &= -\frac{i}{2\pi}\int_{\mu_R}^{\mu_L} \mathrm{d}\epsilon G^<(\boldsymbol{r},\epsilon).\end{aligned} \tag{2.72}$$

2.4.2 LCAO Representation

In this subsection, we review the formalism for obtaining the electron densities ρ_e and ρ_n in the representation with localized basis functions.[40]

SIESTA employs numerical linear combination of atomic orbitals (LCAO) basis set to represent mean field equations. Fig. 2.11 illustrates an abstract molecular junction which consists of an inhomogeneous center region and periodic left and right leads. The two leads can be different. With a localized basis set, the Hamiltonian for

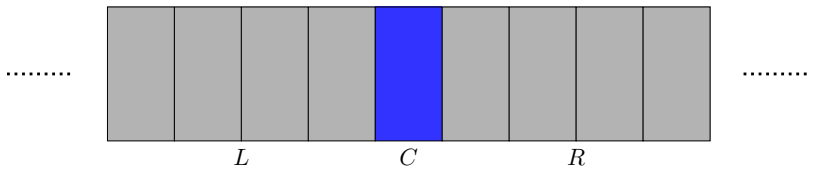

Figure 2.11: An abstract molecular junction. $L(R)$ is the periodic left (right) lead. C is the inhomogeneous center region.

the molecular junction shown in Fig. 2.11 writes

$$\begin{pmatrix} \boldsymbol{h}_{l,\infty} & \boldsymbol{h}_{l,l+1} & 0 & 0 & 0 \\ \boldsymbol{h}_{l,l-1} & \boldsymbol{h}_{l,l} & \boldsymbol{h}_{l,c} & 0 & 0 \\ 0 & \boldsymbol{h}_{c,l} & \boldsymbol{h}_{c,c} & \boldsymbol{h}_{c,r} & 0 \\ 0 & 0 & \boldsymbol{h}_{r,c} & \boldsymbol{h}_{r,r} & \boldsymbol{h}_{r,r+1} \\ 0 & 0 & 0 & \boldsymbol{h}_{r,r-1} & \boldsymbol{h}_{r,\infty} \end{pmatrix}. \tag{2.73}$$

In Eqn. 2.73, $\boldsymbol{h}_{c,c}$ is the Hamiltonian for the center region; while $\boldsymbol{h}_{l,\infty}$ and $\boldsymbol{h}_{r,\infty}$ are the Hamiltonians for the left and right leads respectively

$$\boldsymbol{h}_{l,\infty} \equiv \begin{pmatrix} \ddots & \ddots & \ddots & 0 \\ 0 & \boldsymbol{h}_{l,l-1} & \boldsymbol{h}_{l,l} & \boldsymbol{h}_{l,l+1} \\ 0 & 0 & \boldsymbol{h}_{l,l-1} & \boldsymbol{h}_{l,l} \end{pmatrix}, \tag{2.74}$$

and

$$\boldsymbol{h}_{r,\infty} \equiv \begin{pmatrix} \boldsymbol{h}_{r,r} & \boldsymbol{h}_{r,r+1} & 0 & 0 \\ \boldsymbol{h}_{r,r-1} & \boldsymbol{h}_{r,r} & \boldsymbol{h}_{r,r+1} & 0 \\ 0 & \ddots & \ddots & \ddots \end{pmatrix}. \tag{2.75}$$

In order to calculate the lesser Green's function, define the surface Green's functions $\boldsymbol{g}_{l,\infty} \equiv [(\epsilon + i\eta)\boldsymbol{s}_{l,\infty} - \boldsymbol{h}_{l,\infty}]^{-1}$ and $\boldsymbol{g}_{r,\infty} \equiv [(\epsilon + i\eta)\boldsymbol{s}_{r,\infty} - \boldsymbol{h}_{r,\infty}]^{-1}$, where $\boldsymbol{s}_{l,\infty}$ and $\boldsymbol{s}_{r,\infty}$ are the overlapping matrices; define the self energies $\boldsymbol{\Sigma}^L_{l,l} \equiv \boldsymbol{h}^{\epsilon}_{l,l-1}\boldsymbol{g}_{l,\infty}(c-2, c-2)\boldsymbol{h}^{\epsilon}_{l,l+1}$ and $\boldsymbol{\Sigma}^R_{r,r} \equiv \boldsymbol{h}^{\epsilon}_{r,r-1}\boldsymbol{g}_{r,\infty}(c+2, c+2)\boldsymbol{h}^{\epsilon}_{r,r+1}$ where $\boldsymbol{h}^{\epsilon}_{i,j} = (\epsilon + i\eta)\boldsymbol{s}_{i,j} - \boldsymbol{h}_{i,j}$; define the lesser self energy

$$\boldsymbol{\Sigma}^{<}[f_L, f_R] = -2i\,\mathrm{Im}(f_L\boldsymbol{\Sigma}^L_{l,l} + f_R\boldsymbol{\Sigma}^R_{r,r}), \tag{2.76}$$

where f_L and f_R are the equilibrium distributions for the left and right leads $f_L(\epsilon) = f_{FD}(\epsilon - \mu_L)$ and $f_R(\epsilon) = f_{FD}(\epsilon - \mu_R)$. Then the lesser Green's function can be

calculated by

$$\boldsymbol{G}^{<} = \boldsymbol{G}^{R}\boldsymbol{\Sigma}^{<}[f_L, f_R]\boldsymbol{G}^{A}. \tag{2.77}$$

In Eqn. 2.77, the advanced Green's function $\boldsymbol{G}^{A} = (\boldsymbol{G}^{R})^{\dagger}$ and the retarded Green's function $\boldsymbol{G}^{R}$ for the center region can be calculated by

$$\boldsymbol{G}^{R} = \begin{pmatrix} \boldsymbol{h}^{\epsilon}_{l,l} - \boldsymbol{\Sigma}^{l}_{l,l} & \boldsymbol{h}^{\epsilon}_{l,c} & 0 \\ \boldsymbol{h}^{\epsilon}_{c,l} & \boldsymbol{h}^{\epsilon}_{c,c} & \boldsymbol{h}^{\epsilon}_{c,r} \\ 0 & \boldsymbol{h}^{\epsilon}_{r,c} & \boldsymbol{h}^{\epsilon}_{r,r} - \boldsymbol{\Sigma}^{r}_{r,r} \end{pmatrix}^{-1}. \tag{2.78}$$

When $f_L(\epsilon) = f_R(\epsilon) = 1$, the lesser Green's function reduces to the retarded Green's function $\mathrm{Im}[\boldsymbol{G}^{<}(\epsilon)] = -2f_{FD}(\epsilon)\,\mathrm{Im}[\boldsymbol{G}^{R}(\epsilon)]$. Then the equilibrium and current-carrying electron densities in Eqn. 2.72 can be rewritten as

$$\begin{aligned} \boldsymbol{\rho}_e &= -\frac{1}{\pi}\,\mathrm{Im}\left[\int_{\infty}^{\mu_r} \mathrm{d}\epsilon \boldsymbol{G}^{R}(\epsilon)\right], \\ \boldsymbol{\rho}_n &= -\frac{i}{2\pi}\int_{\mu_r}^{\mu_l} \mathrm{d}\epsilon \boldsymbol{G}^{<}(\epsilon). \end{aligned} \tag{2.79}$$

Note that, in the DMF approach, the junction is described by two mean field Hamiltonians $\hat{h}_e$ and $\hat{h}_n$. Thus the equilibrium electron density ρ_e should be calculated from $\hat{h}_e$ via G^{R}_{e} while the current-carrying electron density ρ_n should be calculated from $\hat{h}_n$ via $G^{<}_{n}$.

2.4.3 Self-consistent Procedure

In this section, we present the self-consistent (SC) procedure for solving the dual mean field equations in Eqn. 2.45. Our implementation is modified from the TranSIESTA subroutines in the SIESTA package.[42,57]

The SC procedure is shown in Fig. 2.12. Given the initial equilibrium and current-carrying electron densities, ρ_e and ρ_n, the mean field Hamiltonians for equilibrium

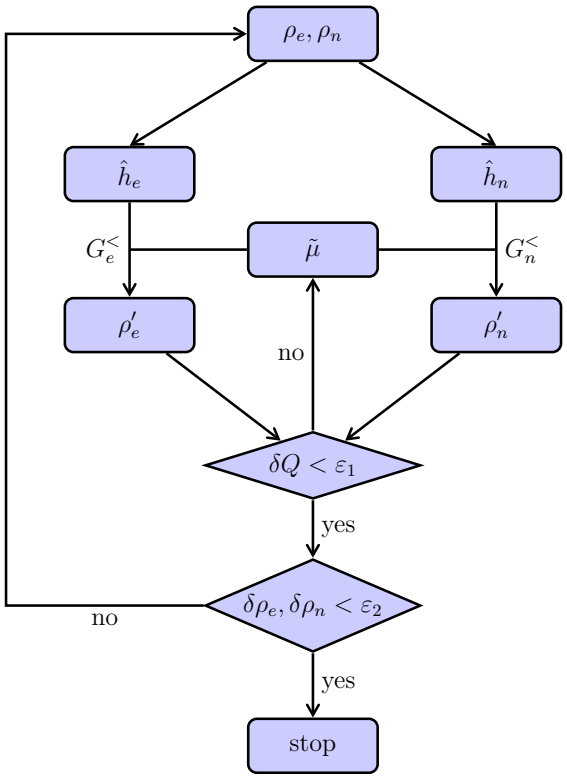

Figure 2.12: Self-consistent procedure for solving the DMF equations.

and current-carrying electrons, $\hat{h}_e$ and $\hat{h}_n$, are constructed. With the initial effective chemical potential $\tilde{\mu}$, the new electron densities ρ'_e and ρ'_n are computed via the lesser Green's functions $G_e^<$ and $G_n^<$. If the difference between the old and new number of electrons in the center region, δQ, is greater than a small real number ε_1, the charge is not conserved and $\tilde{\mu}$ will be tuned until $\delta Q < \varepsilon_1$ is satisfied. After the charge is conserved, we compare the old and new electron densities. If their differences, $\delta\rho_e$ and $\delta\rho_n$, are smaller than a small real number ε_2, the electron densities are considered converged and the SC procedure will stop. Otherwise, the new electron densities will be taken as inputs and the SC procedure will continue until the convergence is achieved.

It should pointed out that, without the charge conservation loop, the absolute deviation in the number of electrons is usually in the order of 10^{-1}. Our simulations showed that such deviations are not important for non-magnetic systems. However, for magnetic systems, the charge conservation may be crucial.

Xue Yi Zhi Yong.

<Han Shu>

3

Applications of Steady-State DFT

In this chapter, we will present the simulation results for several realistic molecular junctions. By these calculations, we show the features, the validity and the usefulness of SS-DFT. Specifically, we consider three molecular junctions which are 1) a graphene nanoribbon (GNR) junction, 2) a junction consisting of carbon nanotube (CNT) leads and a benzene molecule, and 3) a junction with silver leads and self-assembled monolayer (SAM) of alkanethiolate molecules sandwiched between. In the follows, the DFT+NEGF simulations are performed via TranSIESTA; and the SS-DFT simulations are done without charge conservation.

3.1 Graphene Nanoribbon Junction

In this section, we present simulation results for the GNR junction by which we show the non-equilibrium effects of SS-DFT exchange energy as mentioned in section 2.3. In addition, we will also analyze the local extent of non-equilibrium by the non-equilibrium index $\eta(\boldsymbol{r})$ in SS-DFT.

With tunable electronic structure, GNRs are promising building blocks for electronic devices.[77,78] Two types of GNRs with zero chiral angle exist, namely armchair GNR (AGNR) and zigzag GNR (ZGNR). It was found that ZGNRs are metalic and, for ZGNR based junctions under low biases, the current flows through edge states.[77,79] For one-dimensional systems under a finite temperature, long-range magnetic order may not be stable.[80] Thus we follow previous studies and set the total spin of our GNR junction to be zero in this work.[81]

The simulation details are as follows. We relaxed the atomic structure of the GNR junction using SIESTA package and performed finite bias calculations using both SS-DFT and DFT+NEGF methods. In all calculations, we adopted non-relativistic norm-conserving pseudopotential without core correction, single-ζ basis set and $1 \times 1 \times 30$ Monkhorst_Pack k grid.[82] For the relaxation calculations, PBE GGA exchange correlation energy functional,[72] 200 Ry mesh cutoff and 0.04 eV/Å force tolerance were used. For the transport calculations, CA LDA exchange correlation energy functional,[66] and 100 Ry mesh cutoff were applied.

The GNR junction under study is formed by joining a 5-ZGNR with a 3-ZGNR where n-ZGNR denotes a ZGNR with n zigzag lines of carbon atoms. The relaxed atomic structure of the GNR junction is shown in Fig. 3.1 where the dash lines mark the boundary of the center region. The interface between 5-ZGNR and 3-ZGNR works as a scatterer. To meet the requirements for finite bias simulation we choose the following settings. 1) The center region is made of three unit cells of 5-ZGNR

and three unit cells of 3-ZGNR so that the distortion of electron density caused by electron scattering happens only within the center region; 2) Two unit cells of ZGNR are used for both left and right leads so that the initial electron density on the left-center and right-center boundaries recover the bulk electron density.

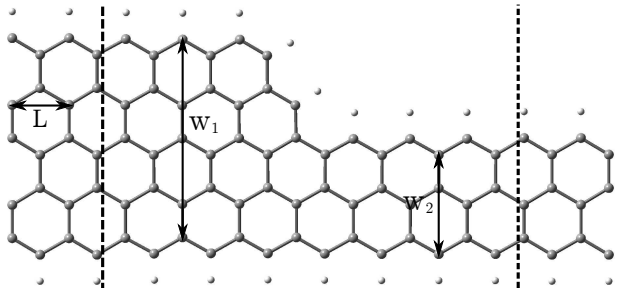

Figure 3.1: Relaxed structure of the GNR junction. $L = 2.53$ Å, $W_1 = 8.80$ Å, $W_2 = 4.41$ Å.

In Fig. 3.2, both I-V curves from SS-DFT and DFT+NEGF calculations for the GNR junction are presented. When bias voltage is small (< 0.1 V), SS-DFT essentially reproduces DFT+NEGF results. Starting from 0.1 V, significant deviations between the two calculations occur. As shown in the figure, the current from SS-DFT is always lower than that obtained from DFT+NEGF. To understand this difference, we plot in the inset of Fig. 3.2 the iso-surface of the difference between SS-DFT non-equilibrium exchange potential (v_x^n) and the exchange potential calculated from DFT+NEGF. The iso-surface value is 15 meV. This plot shows that the exchange potential increases significantly at edges where the current flows through. However for other parts of the system, the non-equilibrium correction to the potential is insignificant. The increase of the exchange potential leads to a higher scattering barrier in the scattering region, and in turn, decreases the current as we see in Fig. 3.2.

In Fig. 3.3, we plot the color map of $\eta(\boldsymbol{r})$ in the scattering region of the GNR junction under 0.2 V. The plot provides detailed spacial information for the non-equilibrium degree of the system. As seen from the figure, the extent of non-equilibrium at different places in the scattering region is quite different: Edges are far away from equilibrium while the middle part of the GNR is still approximately

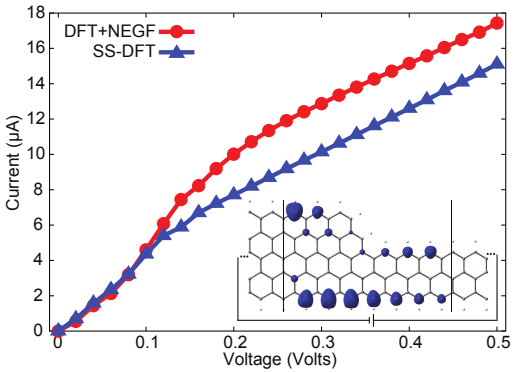

Figure 3.2: I-V curves for the GNR junction calculated from both SS-DFT and DFT+NEGF. The inset shows the iso-surface of the difference between SS-DFT non-equilibrium exchange potential and the exchange potential calculated from DFT+NEGF.

in local equilibrium.

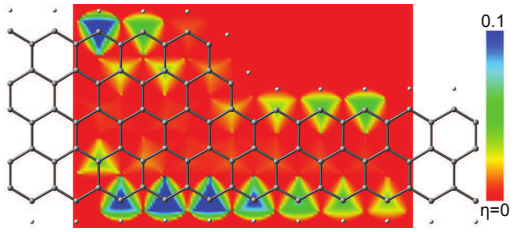

Figure 3.3: Color map of the non-equilibrium index $\eta(\boldsymbol{r})$ in the scattering region of the GNR junction. The plotting plane is 2.2 Å above the GNR. The degree of non-equilibrium becomes higher when the color changes from red to blue.

In conclusion, we have presented the simulation results for a GNR junction by both SS-DFT and DFT+NEGF methods. In comparison, SS-DFT leads to significantly lower electric current than DFT+NEGF for the GNR junction due to the non-equilibrium correction to the exchange energy. In addition, the non-equilibrium index $\eta(\boldsymbol{r})$ provides detailed spacial information for the extent of the non-equilibrium in the scattering region, which improves our understanding of properties of molecular junctions under a finite bias.

3.2 CNT-Benzene-CNT Junction

In this section, we will present the simulation results for the CNT-Benzene-CNT junction and its decoupled twin. The energetics, I-V characteristics, and elec-

tronic structure calculated from SS-DFT will be compared to those calculated from DFT+NEGF. Particularly, we show that SS-DFT is able to predict the local equilibrium for the decoupled junction under finite bias.

CNTs have fantastic one-dimensional characteristics[83,84] and tunable electronic properties.[85–87] They are promising building blocks in future nano-electronic devices.[88–91] The benzene molecule, on the other hand, has been extensively used as a molecular center in various kinds of junctions in both experimental and theoretical studies.[90,92,93] Combining the two, we use a CNT-benzene-CNT junction as an example to demonstrate SS-DFT.

We relaxed the atomic structure of the junction by SIESTA with the following parameters: PBE GGA exchange correlation energy functional,[72] 200 Ry mesh cutoff, 1×10^{-4} eV for the energy tolerance, and 0.04 eV/Å for the force tolerance. For finite bias calculations, we used CA LDA exchange-correlation energy functional[66] and 120 Ry mesh cutoff. Non-equilibrium exchange energy functional was adopted in SS-DFT calculations.[55] In addition, $1 \times 1 \times 30$ k-point mesh was employed for the separate lead calculations. Through all calculations, single-ζ basis set and non-relativistic norm-conserving pseudopotential without core correction were applied.

The atomic structure of CNT and the distance between two leads were optimized in sequence. To relax the distance between two leads, we first made a series of CNT-benzene-CNT junctions with different separations. Then we relax the center region with the two leads fixed for each junction. Finally, the relaxed junction with lowest energy has optimal atomic configuration. A plot of the energy versus the distance between two leads is shown in Fig. 3.4. The optimized CNT-benzene-CNT molecular junction is shown in Fig. 3.5. As can be seen, the junction consists of two semi-infinite metallic $(5, 5)$ CNTs and a benzene molecule in between. Both CNTs are closed at one end with a C_{30} cap. In order to form good contacts, two H atoms in the benzene molecule are taken away. In addition, the two vertical lines across the

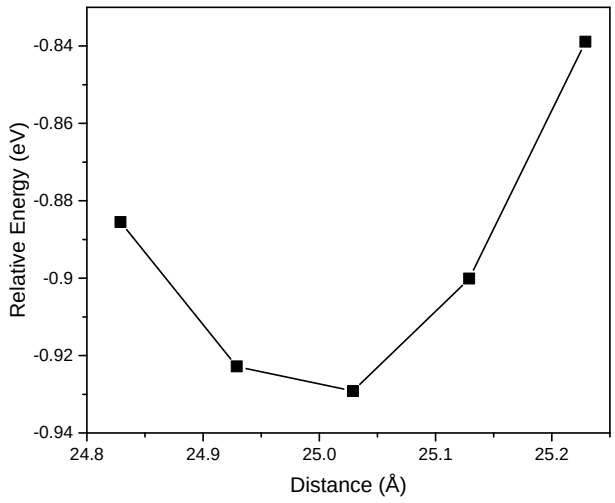

Figure 3.4: The energy of the CNT-Benzene-CNT junctions versus the distance between the left and right leads. The configuration with lowest energy is optimal.

junction mark the boundary between the leads and the contact region.

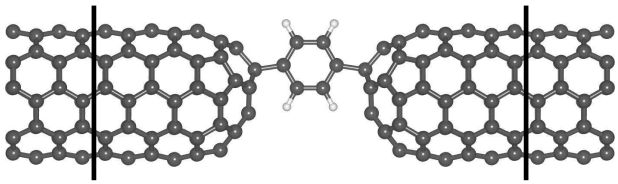

Figure 3.5: Relaxed atomic structure of the CNT-Benzene-CNT junction. Color scheme: C, grey; H, white.

At finite bias, we calculated the energy of the CNT-Benzene-CNT junction by both SS-DFT and DFT+NEGF. The energy difference between the two methods is shown Fig. 3.6 where E and $\tilde{E}$ are the ensemble averages of the Hamiltonian $\hat{H}$ and the effective Hamiltonian $\hat{\tilde{H}} = \hat{H} - eV_b/2$ respectively. Clearly, SS-DFT bears lower energies at all bias voltages, which is expected since SS-DFT searches the lowest-energy steady state with one more degree of freedom than DFT+NEGF, namely the current-carrying electron density. At zero bias, the junction is in equilibrium and SS-DFT reduces to GS-DFT. Consequently, the energy difference between SS-DFT and DFT+NEGF vanishes at zero bias.

Fig. 3.7 plots the I-V curves for the junction calculated from both SS-DFT and DFT+NEGF. The two methods predict similar electric current for biases between 0.2

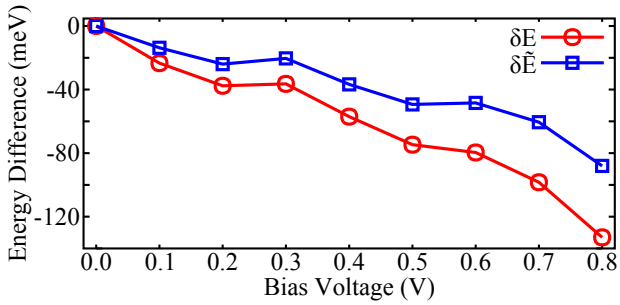

Figure 3.6: The energy differences between SS-DFT and DFT+NEGF, i.e. $\delta E = E_{\text{SS-DFT}} - E_{\text{DFT+NEGF}}$. Both the energy δE and the effective energy $\delta \tilde{E}$ are presented.

and 0.8 V and a prominent negative-differential-resistance (NDR) peak at around 0.05 V. However, the NDR peak predicted by SS-DFT occurs slightly earlier. To

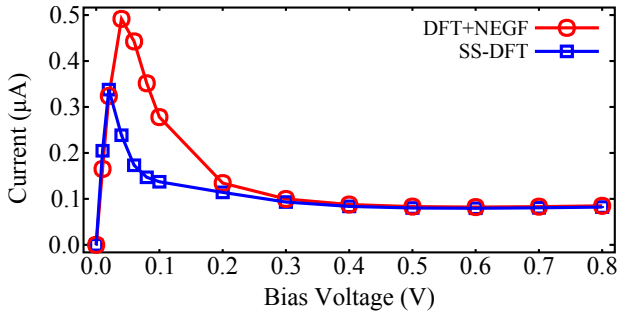

Figure 3.7: The I-V characteristics of the CNT-Benzene-CNT junction calculated from both SS-DFT and DFT+NEGF.

understand the reason, we plot the projected density of states (PDOS) for the benzene molecule in Fig. 3.8a and the transmission function of the junction in Fig. 3.8b. As shown in Fig. 3.8a, there are two degenerate states when the bias voltage is small; they split and become non-degenerate at large bias voltages. Fig. 3.8b shows that the state with lower energy is not conductive while the one with higher energy is conductive. Furthermore, the conductive state calculated from SS-DFT enters (and also exits) the bias window earlier than the one calculated from DFT+NEGF. As a result, the NDR peak for SS-DFT occurs earlier. Due to the relative shift of the NDR peaks, SS-DFT predicts significantly lower current than DFT+NEGF between the bias voltages 0.05 and 0.2 V.

A feature in the PDOS plotted in Fig. 3.8a is that the state with lower energy

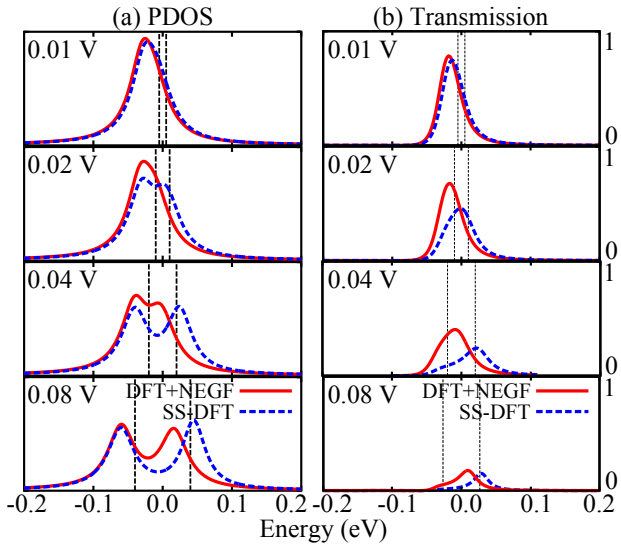

Figure 3.8: (a) PDOS for the benzene molecule within the CNT-benzene-CNT junction. (b) Transmission function of the CNT-benzene-CNT junction.

shifts with the right chemical potential μ_r while the one with higher energy shifts with the left chemical potential μ_l. This is because the state with lower (higher) energy is coupled with the right (left) lead which can be seen from the local density of states (LDOS) plotted in Fig. 3.9. Due to the coupling, when the right (left) chemical potential μ_r (μ_l) becomes lower (higher), the energy of the state with lower (higher) energy decreases (increases).

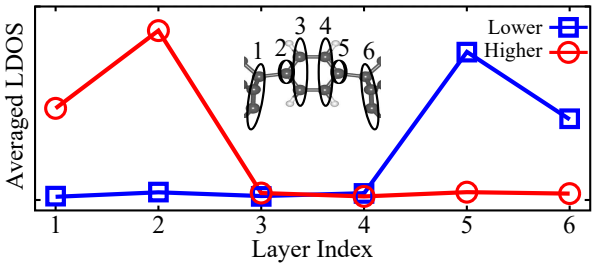

Figure 3.9: Averaged LDOS for the CNT-benzene-CNT junction under 0.08 V. The layer indexes 1-6 are illustrated in the inset. Each layer contains one or more carbon atoms. The averaged LDOS for a layer is defined as the PDOS to this layer divided by the number of atoms within the same layer. Larger LDOS means stronger coupling.

Now we decouple the CNT leads and the benzene molecule by pulling them apart. The resultant atomic structure is shown in Fig. 3.10. In this case, the benzene molecule in the center is known to be in local equilibrium even under finite bias

voltage. We simulated the decoupled CNT-Benzene-CNT junction under 0.5 V of

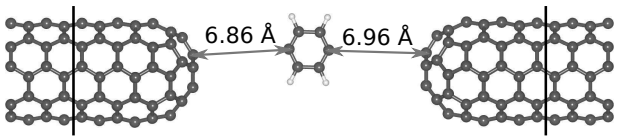

Figure 3.10: The atomic structure of the decoupled CNT-Benzene-CNT junction where the distance between the center molecule and either lead is more than 6.5 Å. In this case, the center molecule is essentially isolated.

bias voltage using both SS-DFT and DFT+NEGF. For comparison, we also did GS-DFT calculation for the decoupled junction under zero bias. From the self-consistent fields calculated from all these three methods, we obtained the PDOS of the benzene molecule and plotted them in Fig. 3.11. As shown in Fig. 3.11, SS-DFT agrees with GS-DFT very well, while DFT+NEGF bears different electronic structures. To further il-

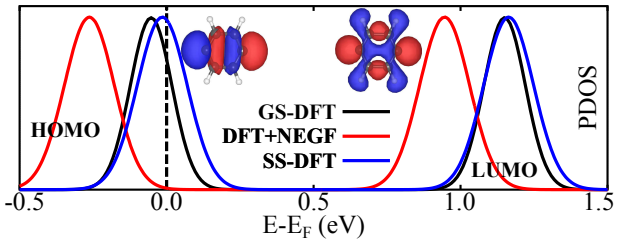

Figure 3.11: PDOS of the benzene molecule calculated from three different methods, GS-DFT for the decoupled CNT-Benzene-CNT junction under zero bias, DFT+NEGF and SS-DFT for the decoupled junction under 0.5 V of bias voltage. The Fermi energy for GS-DFT and the effective Fermi energies for DFT+NEGF and SS-DFT are set to zero. The HOMO and LUMO are plotted aside the corresponding PDOS peaks with the positive (negative) phase in red (blue).

lustrate the difference between different methods, we plot the difference between the total electron densities around the center molecule $\delta\rho_1 = \rho_{(\text{GS-DFT})} - \rho_{(\text{DFT+NEGF})}$ in Fig. 3.12a, and $\delta\rho_2 = \rho_{(\text{SS-DFT})} - \rho_{(\text{DFT+NEGF})}$ in Fig. 3.12b. Clearly, DFT+NEGF yields quite different total electron density from the other two methods, and the densities from GS-DFT and SS-DFT are similar. Furthermore, the asymmetrical distribution of $\delta\rho_1$ in Fig. 3.12a is casued by the absence of external electric field in the GS-DFT calculation. To illustrate the polarization effect of the external field, we perform a GS-DFT calculation for solely an benzene molecule (without $1, 4$ hydrogen atoms) under an external electric field of strength 0.014 V/Å which equals 0.5 V divided by

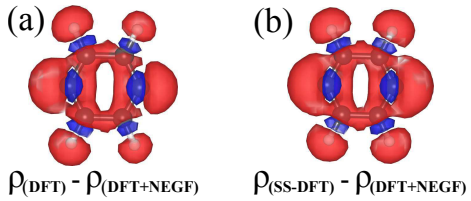

Figure 3.12: The difference in the total electron densities calculated from different methods: $\delta\rho_1 = \rho_{\text{(DFT)}} - \rho_{\text{(DFT+NEGF)}}$ in panel (a) and $\delta\rho_2 = \rho_{\text{(SS-DFT)}} - \rho_{\text{(DFT+NEGF)}}$ in panel (b). The isosurface value is 5×10^{-5} Bohr^{-3} for both plots. The positive (negative) is in red (blue).

the distance between left and right leads of the decoupled CNT-benzene-CNT junction. This GS-DFT calculation bears the electron density $\rho'_{\text{(GS-DFT)}}$. Then we plot the electron density difference $\delta\rho_3 = \rho'_{\text{(GS-DFT)}} - \rho_{\text{(DFT+NEGF)}}$ in Fig. 3.13b which clearly shows the $\delta\rho_3$ becomes symmetrical.

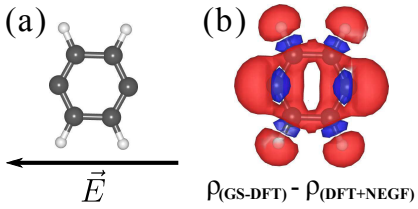

Figure 3.13: (a) A benzene molecule (without $1,4$ hydrogen atoms) under an external electric field. Its electron density calculated from GS-DFT is denoted as $\rho'_{\text{(GS-DFT)}}$. (b) Total electron density difference $\delta\rho_3 = \rho'_{\text{(GS-DFT)}} - \rho_{\text{(DFT+NEGF)}}$ around the benzene molecule. The iso-value is 1.5×10^{-4} Bohr^{-3}. The positive (negative) is in red (blue).

In conclusion, we have simulated a CNT-benzene-CNT junction and its decoupled twin. For the coupled junction, both SS-DFT and DFT+NEGF captures a significant NDR; however SS-DFT always bears a steady state with lower energy compared with DFT+NEGF. Furthermore for the decoupled junction, SS-DFT is able to predict the correct local equilibrium electronic structure.

3.3 SAM of Alkanethiolates

In this section we apply SS-DFT to a molecular junction involving self-assembled monolayer (SAM) of alkanethiolate molecules.[94] Especially, the experimentally observed odd-even effects in the charge mobility of the alkanethiolate SAM junction

will be explained.

The self-assembled monolayer (SAM) of molecules is a promising building block for future molecular electronics.[95,96] The most extensively studied SAM is made of alkanethiolate molecules, e.g. $CH_3(CH_2)_{n-1}SH$ which contains n methylene groups.[97] Experimentally the SAM of alkanethiolates shows odd–even effects in its charge mobility, namely 1) the SAM with even n has higher charge mobility than the odd, and 2) the length dependence of the electric current is significantly different between the odd and even SAMs.[98]

The simulation details are given below. We used SIESTA to optimize the geometry of the molecular junction. The energy and force tolerances were set to 1×10^4 eV and 0.01 eV/Å respectively. In all calculations, PBE GGA exchange correlation energy functional[72], single-ζ polarized basis set, 100 Ry mesh cutoff, and $3 \times 3 \times 1$ k point sampling in the Brillouin zone were applied.

To get the optimized atomic structure, we first investigate the binding sites for the S atoms on the Ag $[111]$ substrate which contains five Ag layers. It turned out that the preferred binding site is between the bridge and hollow sites. Next we relaxed the alkanethiolate SAM on the substrate without the top lead. Then we optimized the distance between the top lead and the SAM during which all atoms except for the two outermost layers of Ag are fully relaxed. Some optimization procedures are shown in Fig. 3.14 as examples. The relaxed atomic structures of the alkanethiolate SAM, with $n = 11$ and 12, on the Ag substrate are shown in Fig. 3.15a. Fig. 3.15b shows the structure of the top lead which consists of a GaO monolayer on the Ag $[111]$ surface. The transport direction is perpendicular to the Ag surface which is along the z axis and the molecular junction is periodic in xy plane. As shown in Fig. 3.15c, there are four alkanethiolate molecules in each unit cell. According to previous studies, the alkanethiolate molecules exhibit a tilt angle relative to z axis and a twist angle relative to each other which are illustrated in Fig. 3.15d and 3.15e respectively.

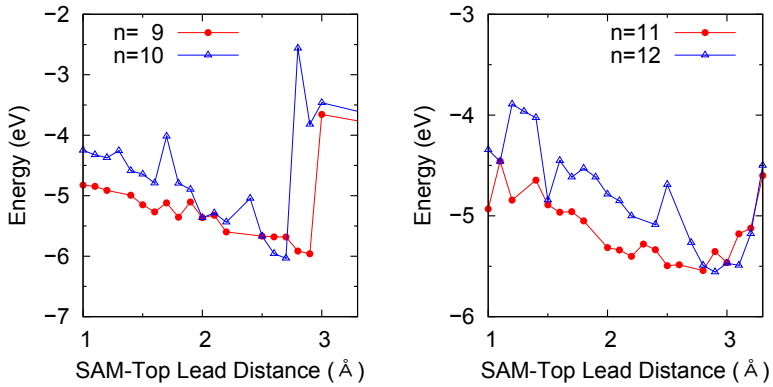

Figure 3.14: Procedures for optimizing the distance between the alkanethiolate SAM and the top Ag probe for $n = 9, 10, 11, 12$. The optimized distance is typically around 3 Å.

From our geometry optimization, the tilt angle is about $13°$ and the twist angle is about $50°$ in agreement with experimental observations. Furthermore, it was found that a change of $3°$in the tilt angle leads to at least 0.5 eV of energy increase indicating that the SAM layer is stable at room temperature.

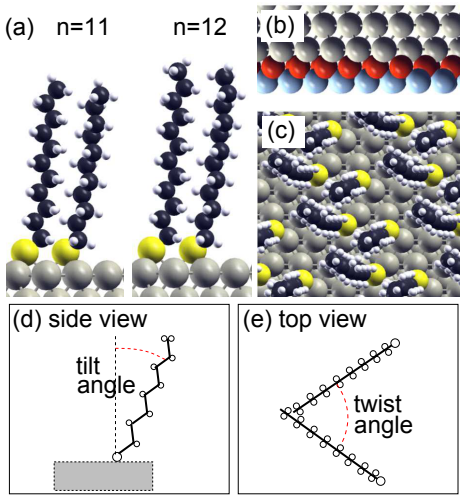

Figure 3.15: (a) Side view of alkanethiolates for $n = 11$ and 12. The S atom at the bottom end of the molecule is adsorbed on the Ag $[111]$ substrate. Note the difference in the tip structures of odd and even alkanethiolates. (b) Side view of the top electrode which consists of a GaO monolayer on Ag $[111]$ surface. (c) Top view of the SAM on the Ag $[111]$ surface. (d,e) Definitions of tilt and twist angles. [Color scheme: C, black; H, white; S, yellow; Ag, gray; O, red; Ga, blue.]

Let n be an odd integer, define $(n, n+1)$ as a pair of the SAM junctions while $(n-1, n)$ is not. In the same pair, the binding strength for the even junction is stronger than the odd one. This can be seen from Tab. 3.1 which shows the bind-

ing energies (between the SAM and the top lead) for various junctions with different molecular length n. The difference in the binding energies of the junctions in an even-odd pair originates from the geometry of the SAMs. Due to the presence of the tilt angle, the H atoms in the methyl group of the even SAM are closer to the top lead than those of the even SAM in the same pair as shown in Fig. 3.15a. Therefore, the even junction has more molecular orbital overlap between the SAM and the top lead thus stronger interaction. As a consequence of the stronger interaction, the even SAM is more distorted than the odd one which is particularly noticeable for $n > 8$ since longer SAMs are more flexible.

n	7	8	9	10	11	12	13	14	15	16
E_b (eV)	-0.13	-1.07	-0.20	-0.31	-0.11	-0.48	-0.12	-0.47	-0.84	-1.11

Table 3.1: Binding energy E_b per alkanethiolate molecule between the SAM and the top electrode for $7 \leq n \leq 16$. In each odd-even pair, the binding energy for the odd is always less than its even partner.

Furthermore, the difference in the binding strengths leads to the odd-even effects in the charge mobility. Fig. 3.16 shows the dependence of the electric current on the SAM length n for the SAM junctions under 0.2 V. When $n < 9$, the odd-even effects are absent and the current follows the Simmons law $J = J_0 e^{-\beta n}$.[99] When $n > 10$, the odd-even effects become significant with $J_{\text{odd}} = 3.5 \times 10^{-5} e^{-1.14n}$ for the odd junctions and $J_{\text{even}} = 1.1 \times 10^{-4} e^{-1.14n}$ for the even ones. The pair $(9, 10)$ appears as a transition state from the homogeneous Simmons law to the separate odd-even series. The exponential decay constant $\beta = 1.14$ is the same for both odd and even SAM junctions under biases between -0.6 and 0.6 V. This predicted decay constant is equivalent to $\beta = 0.74 \text{Å}^{-1}$ which is comparable to experimental values $0.6 < \beta < 1.0$ Å^{-1}.[98,100–102] It is worth mentioning that the odd-even effects would disappear if the tilt angle between the alkanethiolate molecules is gone according to our calculations.

In order to better understand the odd-even effects, in Fig. 3.17, we plot the trans-

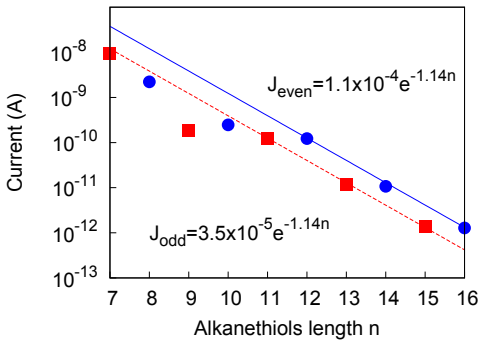

Figure 3.16: Odd–even effects at bias voltage 0.2 V. The current J versus n follows exponential decay. The lines represent fits to the simplified form of the Simmons equation, $J = J_0 e^{-\beta n}$.

mission function averaged over k_x and k_y for the SAM junctions under 0.2 V of bias voltage. As shown in the figure, the transmission decreases as n increases before the odd-even effects occur ($n \leq 10$). After the odd-even effects occur ($n > 10$), the transmission profiles for the SAM junctions in a pair become almost identical.

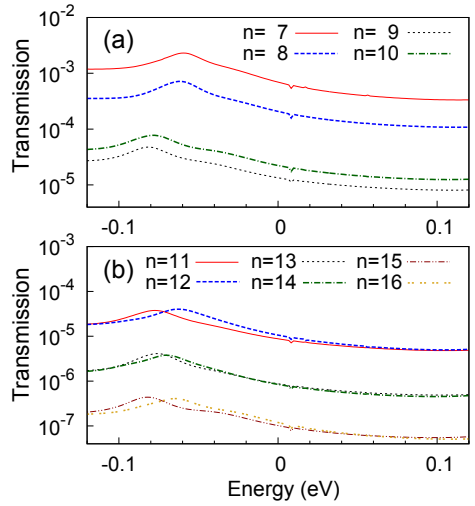

Figure 3.17: Average transmission for the SAM junctions under 0.2 V of bias voltage for $n \leq 10$ (a) and for $n > 10$ (b). The transmission is averaged over k_x and k_y.

Fig. 3.18 shows the I-V curves for various alkanethiolate SAM junctions. The electric current is symmetric about the zero bias voltage for each junction. Fig. 3.18b shows that the I-V curves for the SAM junctions in an odd-even pair are nearly identical when $n > 10$. The odd-even difference in the tip structure remains for the pair $(17, 18)$, therefore the odd-even effects in charge mobility are expected. How-

ever, we didn't simulate the transport properties for SAM junctions with $n > 16$ because the electric current for long molecules is very low (10^{-12} A), whose computation requires high accuracy in the non-equilibrium contour integral and this is beyond our computation ability. In addition, the odd-even effects may disappear for $n > 18$ due to flexural distortions and excessive twisting in the alkanethiolate molecules.

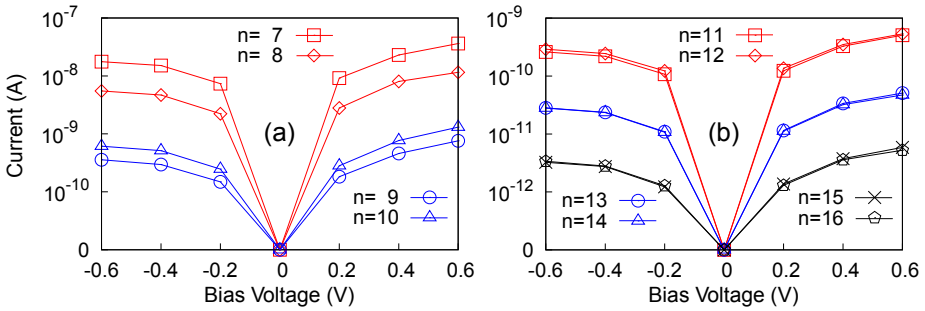

Figure 3.18: I-V curves for the SAM junctions with different n. (a) For $n \leq 10$, the current does not show odd-even effects. The current for $n = 10$ is larger than that for $n = 9$, indicating a transitional region. (b) For $n > 10$, the odd-even effects occur and the electric currents for the SAM junctions in an odd-even pair are almost identical.

To see how the tip geometry affects the electron transport, we plot the xy-plane averaged mean field potential for current-carrying electrons in Fig. 3.19. It is obvious that there is no difference in the potential along the odd and even SAMs except at the top contact between the methyl group and the GaO monolayer. As shown in Fig. 3.19a, for the pair $(7, 8)$, the height and width of potential barriers across the top contact are similar, indicating that the electric current is governed by the length of molecule n for $n < 9$. However, for the pair $(11, 12)$, as shown in Fig. 3.19b, the tunneling barrier across the top contact for the even junction is much lower (1.34 eV) than that for the odd one due to the stronger binding between the SAM and the top electrode. As a consequence, it is easier for electrons to tunnel through the top contact of the even junction ($n = 12$) and the reduction of the tunneling barrier compensates the longer tunneling length, leading to a similar electric current with the odd junction ($n = 11$). Our calculations clearly suggest that, for the Simmons

law $J = J_0 e^{-\beta n}$, 1) the prefactor J_0 is determined by the electron tunneling through the potential barrier across the top contact for the SAM junctions under study; 2) the parameter β describes the dependence on the molecular length n and β is the same for odd and even cases.

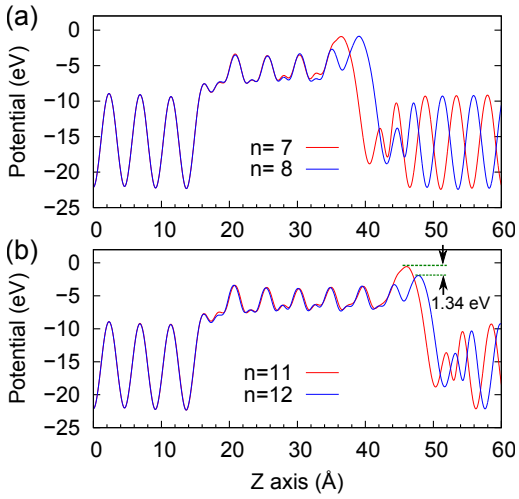

Figure 3.19: Plane averaged mean-field potential for the current-carrying electrons in the SAM junctions with $n = 7, 8$ (a) and $n = 11, 12$ (b). The SAMs span from 14 Å to $41, 43, 50$, and 52 Å for $n = 7, 8, 11, 12$ respectively. In panel (a), the heights of the tunnel barriers across the top contact are approximately the same, while in panel (b) the barrier for the even n is lower by 1.34 eV.

The transmission eigenchannel analysis is helpful in understanding how electrons propagate through the junction. In Fig. 3.20a, we plot the isosurfaces of the dominant transmission eigenchannels for several SAM junctions under 0.2 V of bias voltage. For comparison, in Fig. 3.20b, we plot the isosurface of the partial electron density for the highest valence band (σ_z) of an infinite alkane chain. The plots in Fig. 3.20a and 3.20b resemble each other, suggesting that electrons tunnel through the SAM via the σ_z orbital of the alkane chain. Further analysis shows that the eigenchannels are made of 80% C pz and some minor s and d orbitals.

Let v_e and v_n be the mean field potentials for the equilibrium and current-carrying electrons respectively. Define $\delta v = v_n - v_e$ as the non-equilibrium correction to the mean-field potential. In Fig. 3.21, we plot the isosurface of δv for $n = 7$ and show that the non-equilibrium correction happens mainly at the contact between the SAM

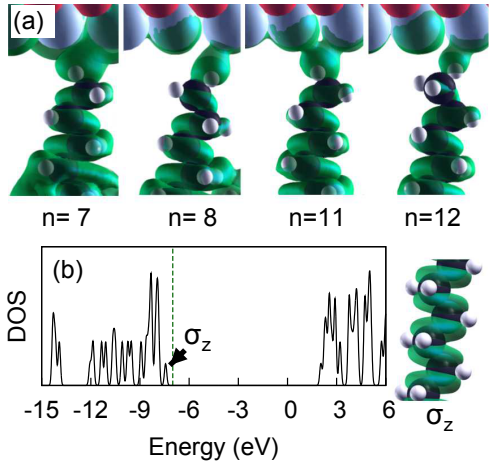

Figure 3.20: (a) Isosurfaces of transmission eigenchannels for $n = 7, 8, 11,$ and 12 under 0.2 V bias voltage. (b) DOS and the highest valence band (σ_z) of an infinite alkane. The green dashed line marks the Fermi level.

and the top lead. Such an observation is valid for both odd and even SAM junctions.

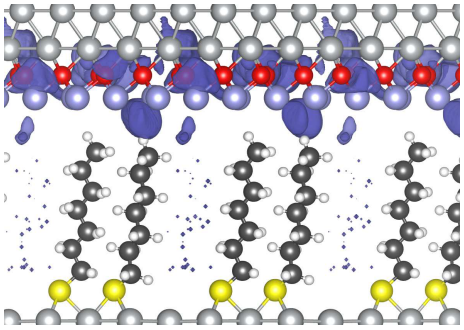

Figure 3.21: Isosurface of non-equilibrium correction to the mean field potential $\delta v = v_n - v_e$ for $n = 7$ under 0.2 V bias voltage.

In conclusion, we have explained the experimentally observed odd-even effects in alkanethilate SAM junctions by first-principles calculations based on SS-DFT. The conformation of the SAMs was found to be crucial for the odd-even effects. As a final remark, the upper Ag-GaO probe used in this study is different from any experiment to our knowledge, yet the odd-even effect was clearly demonstrated and our predicted β value is comparable to experimental ones.

Knowledge is in the end based on acknowledgement.

Ludwig Wittgenstein

4

Conclusion

In conclusion, we proposed the steady-state density functional theory for calculating the electronic structure of open quantum systems in steady state. We proved that two electron densities, the equilibrium electron density ρ_e and the current-carrying electron density ρ_n, together determine the properties of an open system in steady state. This is different from the ground-state density functional theory where total electron density alone determines ground-state properties. By generalizing the Thomas-Fermi-Dirac model to non-equilibrium cases, we derived the exchange energy as a functional of ρ_e and ρ_n for a non-equilibrium uniform non-interacting electron gas. This result enables us to encode the non-equilibrium effects in the energy func-

tional level explicitly. In addition, we also showed that the desired steady state can be obtained from the stationary condition of the effective ground state energy, i.e. $\delta\tilde{E}_0[\rho_e, \rho_n] = 0$. As a consequence, two sets of coupled mean field equations have to be solved. These equations indicate that the current-carrying electrons experience one mean field and the remaining electrons experience another one. This is different from the DFT+NEGF method where all electrons experience the same mean field. Notably, our results may serve as the basis for first-principles studies of the electronic and transport properties of molecular junctions under a finite bias.

After establishing the theory, we have implemented SS-DFT in SIESTA package and used it to study several molecular junctions. In the first study, we focused on a conductive ZGNR junction and showed that the exchange potential v_x increased in the device region. As a result, electric current decreased by around 10% for both low and high biases. It implies that non-equilibrium corrections generally decrease the electric current for metallic systems. By analyzing the non-equilibrium index $\eta(\boldsymbol{r})$, we found that the edges of the ZGNR junction are in a higher degree of non-equilibrium than the middle region. This is the first analysis of the local degree of non-equilibrium in a molecular junction. In the second study, we considered a CNT-benzene-CNT junction for which SS-DFT bore lower energy than the DFT+NEGF method at all biases. This is not surprising because SS-DFT searches for the minimum energy in a larger Hilbert space. To test the validity of SS-DFT, we decoupled the center benzene molecule from the CNT leads. In this limiting case, SS-DFT produced the correct local equilibrium state for the benzene molecule while DFT+NEGF didn't. Finally, we simulated a alkanethilate SAM junction and explained the experimentally observed odd-even effect in the conductivity. According to our simulaltions, the odd-even effect originates from different binding strengths between the SAM and the top electrode. An even SAM is better bound to the top electrode than an odd SAM due to different conformations of the SAM tips.

However, it should be pointed out that SS-DFT applies only when the temperature approaches zero. In the case of finite temperature, the two electron densities, ρ_e and ρ_n, are not basic variables any more and SS-DFT should be treated as an approximation. Another limitation of SS-DFT is that the correlation energy functional is still unknown. Incorporating the correlation effects into SS-DFT is an important direction for future studies, which probably can be done by combining SS-DFT with Gutzwiller DFT.[103] In addition, we hope to report the spin dependent SS-DFT, which is under study at the moment, in the near future. A disadvantage of our implementation is that the computational cost for conserving the number of electrons in the device region is high. This is however unavoidable as long as significant tuning of the effective chemical potential is required. Another problem is that the electron densities in the leads are fixed to be the ground state ones. This is actually inconsistent with the scattering boundary conditions at finite biases. It remains challenging to consider non-equilibrium effects in the leads.

Bibliography

[1] J. W. Negele and H. Orland, *Quantum Many-particle Systems* (Westview Press, 2008).

[2] E. K. U. Gross, E. Runge, and O. Heinonen, *Many-Particle Theory* (IOP Publishing, Bristol, 1991).

[3] H. Haug and A.-P. Jauho, *Quantum Kinetics in Transport and Optics of Semiconductors* (Springer Science & Business Media, 2007).

[4] R. G. Parr and W. Yang, *Density-Functional Theory of Atoms and Molecules* (Oxford University Press, New York and Clarendon Press, Oxford, 1989).

[5] E. Engel and R. M. Dreizler, *Density Functional Theory - An Advanced Course* (Springer Science & Business Media, 2011).

[6] S. Datta, *Electronic Transport in Mesoscopic Systems* (Cambridge University Press, New York, 1995).

[7] P. Hohenberg and W. Kohn, Phys. Rev. **136**, B864 (1964).

[8] Y. Meir and N. S. Wingreen, Phys. Rev. Lett. **68**, 2512 (1992).

[9] A. Aviram and M. A. Ratner, Chem. Phys. Lett. **29**, 277 (1974).

[10] V. V. Zhirnov, R. K. Cavin, J. A. Hutchby, and G. I. Bourianoff, Proc. of IEEE **91**, 1934 (2003).

[11] H. Lee, L.-E. Yu, S.-W. Ryu, J.-W. Han, K. Jeon, D.-Y. Jang, K.-H. Kim, J. Lee, J.-H. Kim, S. C. Jeon, G. S. Lee, J. S. Oh, Y. C. Park, W. H. Bae, H. M. Lee, J. M. Yang, J. J. Yoo, S. I. Kim, and Y.-K. Choi, Proc. VLSI Symp. Tech. Dig. , pp. 58 (2006).

[12] M. Tsutsui and M. Taniguchi, Sensors **12**, 7259 (2012).

[13] A. Batra, P. Darancet, Q. Chen, J. S. Meisner, J. R. Widawsky, J. B. Neaton, C. Nuckolls, and L. Venkataraman, Nano Lett. **13**, 6233 (2013).

[14] G. Binnig and H. Rohrer, IBM J. Res. Dev. **30**, 355 (1986).

[15] M. F. Crommie, C. P. Lutz, and D. M. Eigler, Phys. Rev. B **48**, 2851 (1993).

[16] C. Joachim, J. K. Gimzewski, R. R. Schlittler, and C. Chavy, Phys. Rev. Lett. **74**, 2102 (1995).

[17] A. Yazdani, D. M. Eigler, and N. D. Lang, Science **272**, 1921 (1996).

[18] B. Xu and N. J. Tao, Science **301**, 1221 (2003).

[19] J. He, O. Sankey, M. Lee, N. J. Tao, X. Li, and S. Lindsay, Faraday Discuss. **131**, 145 (2006).

[20] N. Agrait, A. L. Yeyati, and J. M. van Ruitenbeek, Phys. Rep. **377**, 81 (2003).

[21] H. Park, J. Park, A. K. Lim, E. H. Anderson, A. P. Alivisatos, and P. L. McEuen, Nature **407**, 57 (2000).

[22] J. Park, A. N. Pasupathy, J. I. Goldsmith, C. Chang, Y. Yaish, J. R. Petta, M. Rinkoski, J. P. Sethna, H. D. A. na, P. L. McEuen, and D. C. Ralph, Nature **417**, 722 (2002).

[23] L. H. Yu and D. Natelson, Nano Lett. **4**, 79 (2004).

[24] M. A. Reed, C. Zhou, C. J. Muller, T. P. Burgin, and J. M. Tour, Science **278**, 252 (1997).

[25] S. Y. Quek, L. Venkataraman, H. J. Choi, S. G. Louie, M. S. Hybertsen, and J. B. Neaton, Nano Lett. 7, 3477 (2007).

[26] Z.-L. Cheng, R. Skouta, H. Vazquez, J. R. Widawsky, S. Schneebeli, W. Chen, M. S. Hybertsen, R. Breslow, and L. Venkataraman, Nature Nanotechnology **6**, 353 (2011).

[27] D. Porath, A. Bezryadin, S. de Vries, and C. Dekker, Nature **403**, 635 (2000).

[28] H.-W. Fink and C. Schonenberger, Nature **398**, 407 (1999).

[29] A. Y. Kasumov, M. Kociak, S. Guéron, B. Reulet, V. T. Volkov, D. V. Klinov, and H. Bouchiat, Science **291**, 280 (2001).

[30] J. Reichert, R. Ochs, D. Beckmann, H. B. Weber, M. Mayor, , and H. v. Löhneysen, Phy. Rev. Lett. **88**, 176804 (2002).

[31] R. Landauer, IBM J. Res. Dev. **1**, 223 (1957).

[32] M. Büttiker, Phys. Rev. Lett. **57**, 1761 (1986).

[33] L. V. Keldysh, Sov. Phys. JETP **20**, 1018 (1965).

[34] C. Caroli, R. Combescot, P. Nozières, and D. Saint-James, J. Phys. C **4**, 916 (1971).

[35] C. Caroli, R. Combescot, D. Lederer, P. Nozières, and D. Saint-James, J. Phys. C **4**, 2598 (1971).

[36] M. Cini, Phys. Rev. B **22**, 5887 (1980).

[37] N. D. Lang, Phys. Rev. B **52**, 5335 (1995).

[38] M. D. Ventra, S. T. Pantelides, and N. D. Lang, Phys. Rev. Lett. **84**, 979 (1999).

[39] J. Taylor, H. Guo, and J. Wang, Phys. Rev. B **63**, 121104 (2001).

[40] J. Taylor, H. Guo, and J. Wang, Phys. Rev. B **63**, 245407 (2001).

[41] Y. Xue, S. Datta, and M. A. Ratner, J. Chem. Phys. **115**, 4292 (2001).

[42] M. Brandbyge, J.-L. Mozos, P. Ordejón, J. Taylor, and K. Stokbro, Phys. Rev. B **65**, 165401 (2002).

[43] C. Zhang, X. G. Zhang, P. S. Krstić, H. P. Cheng, W. H. Butler, and J. M. MacLaren, Phys. Rev. B **69**, 134406 (2004).

[44] N. Sergueev, D. Roubtsov, and H. Guo, Phys. Rev. Lett. **95**, 146803 (2005).

[45] T. Frederiksen, M. Paulsson, M. Brandbyge, and A. P. Jauho, Phys. Rev. B **75**, 205413 (2007).

[46] H. Mehrez, A. Wlasenko, B. Larade, J. Taylor, P. Grütter, and H. Guo, Phys. Rev. B **65**, 195419 (2002).

[47] L. Shen, M. Zeng, S. W. Yang, C. Zhang, X. Wang, and Y. Feng, J. Am. Chem. Soc. **132**, 11481 (2010).

[48] S. M. Lindsay and M. A. Ratner, Adv. Mater. **19**, 23 (2007).

[49] C. Toher, A. Filippetti, S. Sanvito, and K. Burke, Phys. Rev. Lett. **95**, 146402 (2005).

[50] S. H. Ke, H. U. Baranger, and W. Yang, J. Chem. Phys. **126**, 201102 (2007).

[51] K. S. Thygesen, Phys. Rev. Lett. **100**, 166804 (2008).

[52] K. S. Thygesen and A. Rubio, Phys. Rev. B 77, 115333 (2008).

[53] N. Sai, M. Zwolak, G. Vignale, and M. D. Ventra, Phys. Rev. Lett. **94**, 186810 (2005).

[54] S. Hershfield, Phys. Rev. Lett. 70, 2134 (1993).

[55] C. Zhang, J. At. Mol. Sci. **5**, 95 (2014).

[56] S. Liu, F. Y. Ping, and C. Zhang, J. Chem. Phys. **139**, 191103 (2013).

[57] J. M. Soler, E. Artacho, J. D. Gale, A. García, J. Junquera, P. Ordejón, and D. Sánchez-Portal, J. Phys.: Condens. Matter **14**, 2745 (2002).

[58] M. Gell-Mann and F. Low, Phys. Rev. **84**, 350 (1951).

[59] G. C. WicK, Phys. Rev. **80**, 268 (1950).

[60] R. P. Feynman, Phys. Rev. **76**, 769 (1949).

[61] J. Goldstone, Proc. Roy. Soc. A **239**, 267 (1957).

[62] J. Rammer and H. Smith, Rev. Mod. Phys. **58**, 323 (1986).

[63] J. T. Devreese and E. V. Doren, *Linear and Nonlinear Electron Transport in Solids* (Plenum Press, 1976).

[64] W. Kohn and L. J. Sham, Phys. Rev. **140**, A1133 (1965).

[65] N. H. March, Adv. Phys. **6**, 1 (1957).

[66] D. M. Ceperley and B. J. Alder, Phys. Rev. Lett. **45**, 566 (1980).

[67] S. J. Vosko, L. Wilk, and M. Nusair, Can. J. Phys. **58**, 1200 (1980).

[68] U. von Barth and L. Hedin, J. Phys. C **5**, 1629 (1972).

[69] M. M. Pant and A. K. Rajagopal, Solid State Commun. **10**, 1157 (1972).

[70] J. P. Perdew and A. Zunger, Phys. Rev. B **23**, 5048 (1981).

[71] K. Knöpfle, L. M. Sandratskii, and J. Kübler, Phys. Rev. B **62**, 5564 (2000).

[72] J. P. Perdew, K. Burke, and M. Ernzerhof, Phys. Rev. Lett. 77, 3865 (1996).

[73] E. Runge and E. K. U. Gross, Phys. Rev. Lett. **52**, 997 (1984).

[74] S. Kurth, G. Stefanucci, C.-O. Almbladh, A. Rubio, and E. K. U. Gross, Phys. Rev. B **72**, 035308 (2005).

[75] E. Khosravi, A.-M. Uimonen, A. Stan, G. Stefanucci, S. Kurth, R. van Leeuwen, and E. K. U. Gross, Phys. Rev. B **85**, 075103 (2012).

[76] S. Liu, A. Nurbawono, and C. Zhang, Sci. Rep. **5**, 15386 (2015).

[77] M. Ezawa, Phys. Rev. B **73**, 045432 (2006).

[78] Y.-W. Son, M. L. Cohen, and S. G. Louie, Phys. Rev. Lett. **97**, 216803 (2006).

[79] M. Fujita, K. Wakabayashi, K. Nakada, and K. Kusakabe, Phys. Soc. Jpn. **65**, 1920 (1996).

[80] N. D. Mermin and H. Wagner, Phys. Rev. Lett. **17**, 1133 (1966).

[81] Q. Yan, B. Huang, J. Yu, F. Zheng, J. Zang, J. Wu, B.-L. Gu, F. Liu, and W. Duan, Nano Lett. 7, 1469 (2007).

[82] H. J. Monkhorst and J. D. Pack, Phys. Rev. B **13**, 5188 (1976).

[83] S. Frank, P. Poncharal, Z. L. Wang, and W. A. de Heer, Science **280**, 1744 (1998).

[84] W. Liang, M. Bockrath, D. Bozovic, J. H. Hafner, M. Tinkham, and H. Park, Nature **411**, 665 (2001).

[85] J. W. Mintmire, B. I. Dunlap, , and C. T. White, Phys. Rev. Lett. **68**, 631 (1992).

[86] N. Hamada, S. Sawada, and A. Oshiyama, Phys. Rev. Lett. **68**, 1579 (1992).

[87] R. Saito, M. Fujita, G. Dresselhaus, and M. S. Dresselhaus, Appl. Phys. Lett. **60**, 2204 (1992).

[88] S. J. Tans, A. R. M. Verschueren, and C. Dekker, Nature **393**, 49 (1998).

[89] R. Martel, T. Schmidt, H. R. Shea, T. Hertel, and P. Avouris, Appl. Phys. Lett. **73**, 2447 (1998).

[90] M. D. Valley, R. Gutiérrez, C. Tejedor, and G. Cuniberti, Nat. Nanotechnol. **2**, 176 (2007).

[91] C. Zhang, L. L. Wang, H. P. Cheng, X. G. Zhang, and Y. Xue, J. Chem. Phys. **124**, 201107 (2006).

[92] C. Zhang, M. H. Du, H. P. Cheng, X. G. Zhang, A. E. Roitberg, and J. L. Krause, Phys. Rev. Lett. **92**, 158301 (2004).

[93] B.-Y. Choi, S.-J. Kahng, S. Kim, H. Kim, H. W. Kim, Y. J. Song, J. Ihm, and Y. Kuk, Phys. Rev. Lett. **96**, 156106 (2006).

[94] A. Nurbawono, S. Liu, C. A. Nijhuis, and C. Zhang, J. Phys. Chem. C **119**, 5657 (2015).

[95] W. C. Bigelow, D. L. Pickett, and W. A. Zisman, J. Colloid Interface Sci. **1**, 513 (1946).

[96] A. Ulman, Chem. Rev. **96**, 1533 (1996).

[97] J. C. Love, L. A. Estroff, J. K. Kriebel, R. G. Nuzzo, and G. M. Whitesides, Chem. Rev. **105**, 1103 (2005).

[98] M. M. Thuo, W. F. Reus, C. A. Nijhuis, J. R. Barber, C. Kim, M. D. Schulz, and G. M. Whitesides, J. Am. Chem. Soc. **133**, 2962 (2011).

[99] J. G. Simmons, J. Appl. Phys. **34**, 1793 (1963).

[100] R. E. Holmlin, R. Haag, M. L. Chabinyc, R. F. Ismagilov, A. E. Cohen, A. Terfort, M. A. Rampi, and G. M. Whitesides, J. Am. Chem. Soc. **123**, 5075 (2001).

[101] D. J. Wold, R. Haag, M. A. Rampi, and C. D. Frisbie, J. Phys. Chem. B **106**, 2813 (2002).

[102] X. D. Cui, X. Zarate, J. Tomfohr, O. F. Sankey, A. Primak, A. L. Moore, T. A. Moore, D. Gust, G. Harris, and S. M. Lindsay, Nanotechnology **13**, 5 (2002).

[103] K. M. Ho, J. Schmalian, and C. Z. Wang, Phys. Rev. B 77, 073101 (2008)

Yin Shui Si Yuan.

Yu Xin

A

Mathematica Codes

Mathematica codes for checking the integral in Eqn. 2.61

$$I_3 = -\frac{4\pi}{(2\pi)^6}\int_{\Omega_2} \mathrm{d}\boldsymbol{k}\int_{\Omega_2} \mathrm{d}\boldsymbol{k}'\frac{1}{|\boldsymbol{k}-\boldsymbol{k}'|^2}.$$

In[1]: Integrate[$1/(a * \mathrm{Cos}[x] + 1), \{x, 0, 2 * \mathrm{Pi}\}$, Assumptions $\rightarrow x \in$ Reals&&$a \in$ Reals&&$a > -1$&&$a < 1$]

Out[1]: ConditionalExpression $\left[\frac{2\pi}{\sqrt{1-a^2}}, a \neq 0\right]$

In[2]: Simplify[2 * Pi * Pi * x1 * x2 * Integrate[1/Sqrt[$x * x + y * y +$
$c * x * y + c * c/4 - 1]$, $\{x, 0, 1\}$, $\{y, 0, 1\}$, Assumptions $\to x \in$
Reals&&$y \in$ Reals&&$c \in$ Reals&&$c < -2$]/.$c \to$ ($-$(x1 * x1+
x2 * x2)/(x1 * x2)), Assumptions $\to$ x1 $\in$ Reals&&x2 $\in$ Reals&&
x1 $>$ 0&&x2 $>$ 0&&x1 $\neq$ x2]

Out[2]: $\pi^2 x1x2 \left(-2\text{Log}\left[-2 + \frac{x1}{x2} + \frac{x2}{x1}\right] + \text{Log}\left[\frac{2x1^2 x2^2}{x1^4 + x2^4 - (x1^2 + x2^2)\,\text{Abs}\,[x1^2 - x2^2]}\right]\right)$

In[3]: Simplify[Integrate[%, {x1, k1, k2}, {x2, k1, k2}, Assumptions $\to$ x1
$\in$ Reals&&x2 $\in$ Reals&&k1 $\in$ Reals&&k2 $\in$ Reals&&k1 $>$ 0&&
k1 $<$ k2], Assumptions $\to$ k1 $\in$ Reals&&k2 $\in$ Reals&&k1 $>$ 0&&
k1 $<$ k2]

Out[3]: $\frac{1}{2}\pi^2 \left(2k1^4 - 2k1^3 k2 - k1^2 k2^2 - 2k1k2^3 + 3k2^4 - 4k2^4 \text{ArcTanh}\left[\frac{k1}{k1 - 2k2}\right] + 4k1^2 k2^2 \text{Log}\left[1 - \frac{k1}{k2}\right] + 2k1^4 \text{Log}\left[\frac{k1}{-k1 + k2}\right]\right)$